UNIVERSITY OF COPENHAGEN
FACULTY OF SCIENCE

Characterisation of Silicon Crystals for use in Collimation System Upgrades at the SPS and LHC Particle Accelerators

Master's Thesis in Experimental Particle Physics

Daniel Abdulla Bobruk

Supervisor: Jørgen Beck Hansen

May 2022

Abstract

In this thesis the work that has been completed during a 12 month stay at CERN in the time period March 2021 - March 2022 will be described. Multiple aspects of the work performed will be covered with special emphasis on the collaborative effort of the UA9 collaboration focused on a crystal assisted collimation system based on studies performed in the Super Proton Synchrotron (SPS) accelerator.

Crystal collimation studies require several steps before implementation, so the thesis is a mixture of both accelerator physics, crystal physics, data analysis of Silicon crystal tests, and radiation studies. The Python scripts used for the analysis of data and production of results can be found in the GitHub repository[10].

The thesis describes the work performed at the H8 extraction line where a full characterisation of the Silicon crystals STF113 and ACP82 is obtained by bombarding the crystals in radiation campaigns of protons. The tests are done to extract key characteristics of the crystals such as the mean deflection angle, torsion, and channeling efficiency. The results found for the characterisation are coherent with earlier tests of the crystals[28].

The thesis also presents the work that has been made with the UA9 collaboration to examine the robustness of Silicon crystals based on earlier radiation tests[29][19] in the specific case of accidental full-on beam impact, and do a review of these results.

In this study the simulation results on the losses of particles in the accelerator for two different absorber materials are analysed, where a factor 50-57 improvement in cleaning efficiency of the beam halo is found when using Tungsten absorbers compared to Carbon absorbers in a single passage simulation.

Finally, this thesis concludes the work by presenting the results of the energy depositions in the beam loss monitors and corresponding reduction factor where a comparison to a 2018 experimental study with a similar setup has been made.

The work in this thesis serves as a bench mark study in the SPS for an implementation of a crystal assisted collimation system for the LHC. The work presented has contributed to bring the future installment of an upgraded collimation system in the LHC closer, and finds that further studies are needed to do a conclusive comparison on multi passage effects before implementation in the LHC.

Contents

1 Intro

When particle accelerators are brought up in conversation, they are typically thought of with regards to research regarding particle physics. But accelerators are used in many places, helping not only hardcore scientists but also in the medical field and in treating patients. It is also used for testing many materials used in your everyday. Particle accelerators serve many functions.

Acceleration of particles tell us about the very earliest times of the Universe. Ultra high energy particles allow us a peak into the times right after Big Bang and to find answers for some of the most fundamental questions. The closer we are to the Big Bang the more dense the Universe is, and hence the average energy of every particle is much higher. Thus, the conditions of the very early Universe is recreated when colliding particles at very high energies. It allows us to examine particle behaviour, decay and production to reveal possible new physics beyond the Standard Model.

But beyond answering the big questions particle acceleration is used in many appliances concerning testing materials used in every day appliances. Many of the materials used for construction or technical appliances need to be stress tested for quality checks at to assess the safety of their use in various environments.

At the same time particle accelerators are used for medical appliances. They are used at hospitals to generate radioactive isotopes for use in clinical trials in PET-scanners, and used directly for radiation therapy of patients.

At CERN all possible appliances of particle acceleration are being studied and tested intensely. They are the worlds biggest laboratory which allows for much creativity and a lot of resources to conduct research.

The novel technique that we focus on in this thesis is on the application of Silicon crystals for beam manipulation with emphasis on the implementation in a crystal assisted collimation system, serving as an upgrade to the current collimation system at the LHC. This is possible due to predictions many years ago resulting in tests in the 80's that discovered an effect of crystals referred to as channeling.

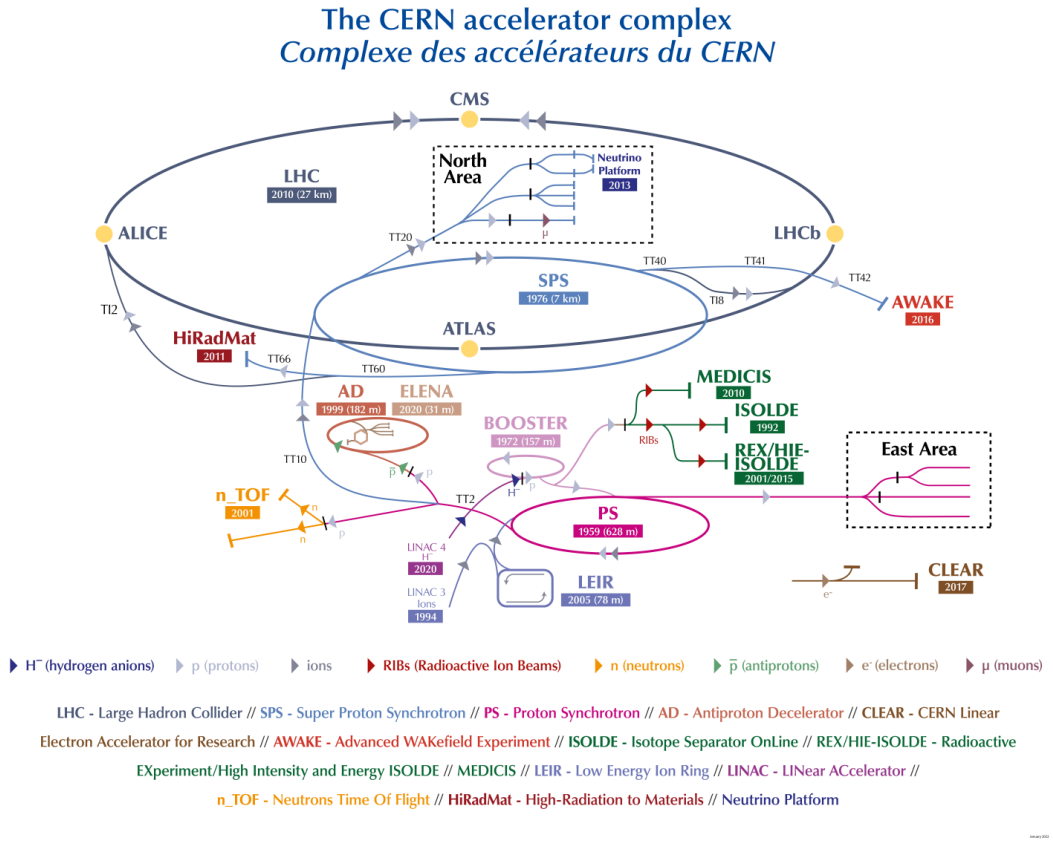

Figure 1: The accelerator complex showing the multiple steps of acceleration and injection points of particles [12]. This study was done with emphasis on research conducted in the Super Proton Synchrotron accelerator.

2 Accelerator physics

The work exhibited in this study was performed at the European Organisation for Nuclear Research (CERN), which is the largest particle accelerator complex in the world, which concerns itself with accelerator studies in many different areas such as fundamental particle physics, radiation studies, material studies, and medicinal applications.

The accelerator complex at CERN consists of multiple accelerators that bring particles to their maximum energy in multiple steps.

In the very beginning stage we have the particle source which provides the accelerator with the type of particles that are intended for the experiment. For example to inject an accelerator with protons, one would need a supply of hydrogen atoms, which are stripped of their electron by an electric field. Then the radio frequency (RF) cavities are used to accelerate the protons in the accelerator. The frequency is steered such that the particles are steered in bunches of particles, which can be thought of as pulses, instead of as a continuous stream of particles [1].

The produced protons from the source are accelerated in a linear accelerator providing DC current. The linear accelerator works as an injector into the first

circular accelerator, the Proton Synchrotron (PS) where they are injected at about 50 MeV. Here they are accelerated up to their maximum energy of 28 GeV, and then injected into the Super Proton Synchotron (SPS) where once again they are accelerated to their maximum energy of 450 GeV, and finally injected into the Large Hadron Collider (LHC) where they are accelerated one final time before finally colliding at a maximum energy of 7 TeV [14].

The maximum energy of a particle in the accelerator is dependent on the size of the accelerator. This means that the maximal energy of particles in the experiments are limited by the physical size of the accelerator complex [34]. This is a natural limit to the scale of particle physics that can be examined in a circular accelerator on Earth. For very high energy physics on the scales of PeV one would be required to look out into the Universe for natural occurring particle acceleration in core-collapse supernovas, where the dynamics of charged particles in the stellar matter cause very strong magnetic fields resulting in the production of cosmic rays due to Fermi acceleration at PeV energies[32].

We start by describing the machinery that makes out a circular particle accelerator. Simplified, a circular accelerator can be thought of as an arrangement of magnets manipulating the trajectory of a charged particle to make it undergo circular motion, and inducing changing electric fields to accelerate the particle [13].

The basic concept of a particle accelerator is having a charged particle undergo circular motion around the accelerator due to the magnetic force from the field induced by a dipole magnet. If we had to only consider a single charged particle in the ideal accelerator complex, we could manage it by using only dipole magnets in the bends of the accelerator, and RF cavities to accelerate them. In reality we need quadropoles to act as electromagnetic lenses when considering bunches of particles, as well as higher order multipoles for correcting errors in placement of quadropoles and for avoiding resonance effects and run-away losses. If we assume two particles in a dipole field with the same starting position and momentum but differing initial angle, we see that one particle starts oscillating around the other particle's trajectory. We call this behaviour Betatron motion and it is the basis of all transverse movement in the accelerator[35].

2.1 Beam motion & Twiss parameters

The particle movement in the accelerator is described by the Lorentz force. From the expression of force for a charged particle in a dipole field we can set up as a second order partial differential equation to obtain the equations of motion. From the equations of motion we obtain a pseudo-harmonic oscillator of the form[16][18][9]

$$x'' + K(s)x = 0 \tag{1}$$

where the factor $K(s)$ varies with the longitudinal coordinate s in the accelerator. Thus, by writing up the equations of motion we get that the restoring force in the

harmonic motion is dependent on s. Hence, the harmonic motion is not simple but changes throughout the machine.

The harmonic motion is shown for the transverse horisontal direction x, but there are also oscillations happening in the transverse vertical direction y. Thus, it must be kept in mind that the solutions shown in this chapter are only shown for the horisontal direction but another set of equations is present for the vertical direction. In fact, we get a set of coupled differential equations which are described by a transport matrix describing the particle's transverse position (x, y) and direction (x', y').

The transport matrix can be written so that the parameters α, β, and γ show up as the eigenvalue solutions to this matrix. These are the Courant-Snyder parameters referred to as the Twiss parameters which describe the optics of the machine. These parameters allow us to study the beam optics in greater detail and can be expressed on the form [16]

$$\alpha(s) = -\frac{1}{2}\beta'(s) \tag{2}$$

$$\gamma(s) = \frac{1 + \alpha(s)^2}{\beta(s)} \tag{3}$$

Again, since the transverse plane includes both x and y there are two sets of Twiss parameters, but we show the quantities only for the horisontal part.

We call the second order differential equation given in equation (1) (and its corresponding differential equation in the y-direction) the Hill's equation of linear transverse particle motion [24].

The Hill's equation has the solution

$$x(s) = \sqrt{\varepsilon\beta(s)}\cos(\phi(s) + \phi(s_0)) \tag{4}$$

where ε is the emittance of the beam, $\beta(s)$ is the beta function as a function of the longitudinal coordinate s in the accelerator, $\phi(s)$ is the particle angular coordinate in its harmonic motion also called the phase advance, and $\phi(s_0)$ is the initial angle. The solution equation (4) makes it clear to us that the transverse coordinates will swing periodically. This solution is important to remember when describing the emittance later.

The beta function $\beta(s)$ is a periodic function given by the optical properties that can be observed in the accelerator by measuring $\beta(s)$ around the beam line as a function of the longitudinal coordinate s. The function describes the optics of the accelerator complex due to its physical geometry which consists of arrangements of dipoles, focusing quadropoles, and defocusing quadropoles[17].

The phase advance $\phi(s)$ in a closed orbit is defined as the evolution of the reciprocal to the beta function $\beta(s)$ over a segment in the accelerator and describes the evolution of the phase of a particle as it travels through the accelerator along the

longitudinal coordinate s [6]

$$\phi(s) = \int_0^s \frac{ds}{\beta(s)} \tag{5}$$

An important property of the accelerator is the tune Q. The tune is the number of Betatron oscillations a particle will undergo before returning to its initial point around the accelerator. Hence, the tune is defined as the number of full oscillations that the phase of a particle will undergo during the phase evolution of one closed orbit around the accelerator

$$Q = \frac{1}{2\pi} \oint \frac{ds}{\beta(s)} \tag{6}$$

It is important that the tune Q is not an integer or half integer number, since the tune is responsible for creating resonance effects via constructive interference from the particle beam wave behaviour. Since we are dealing with harmonic oscillatory behaviour in the accelerator, we can get run-away effects if we are not cautious. The tune is dictated by the optics of the machine which means that it is directly dependent on the design of the accelerator.

There will always be a resonance for each accelerator but we wish to move the resonance so that it happens very infrequently as to avoid run-away resonances. Therefore, the tune is purposely made a non-integer number when designing an accelerator. If the resonances happen after many turns the resonance will not have time to grow coherently between each consecutive resonance. Since the tune Q is non-integer the (x, x') parameters of an particle will change each time it returns to the same position s in the accelerator, and it will take several turns for the particle to have the same parameters (x, x') at the same place.

We turn our attention back to the solution to the Hill's equation (4) which can be reformulated by taking the derivative $x'(s)$ corresponding to the particle direction, inserting the Twiss parameters equations (2), (3) and $\beta(s)$, and isolating the expression for the emittance ε

$$\varepsilon = \gamma(s)x^2(s) + 2\alpha(s)x(s)x'(s) + \beta(s)x'^2(s) \tag{7}$$

We get the expression for an ellipse in the phase space (x, x'). Thus, when a particle completes a whole revolution around the accelerator and returns multiple times to the same coordinate s in the accelerator it will do so with a different phase and span out the shape of a single closed ellipse shape in its phase space (x, x') as described by the equation (7).

The ellipse drawn out will be different for each particle but with a constant area as described by Liouville's Theorem when considering systems of conserving forces only, due to Newtonian mechanics and energy conservation of the system.

Now considering a full ensemble of particles, the emittance ε is a quantity that describes the ellipse in the phase space drawn out by a collection of particles, and specifically it is defined as the Root Mean Square (RMS) of the area of the ellipse containing 90% of the particles[11]. (There are multiple competing definitions for

the emittance whether it is 90%, 95%, or the full area of the ellipse. But we are making use of the 90% definition).

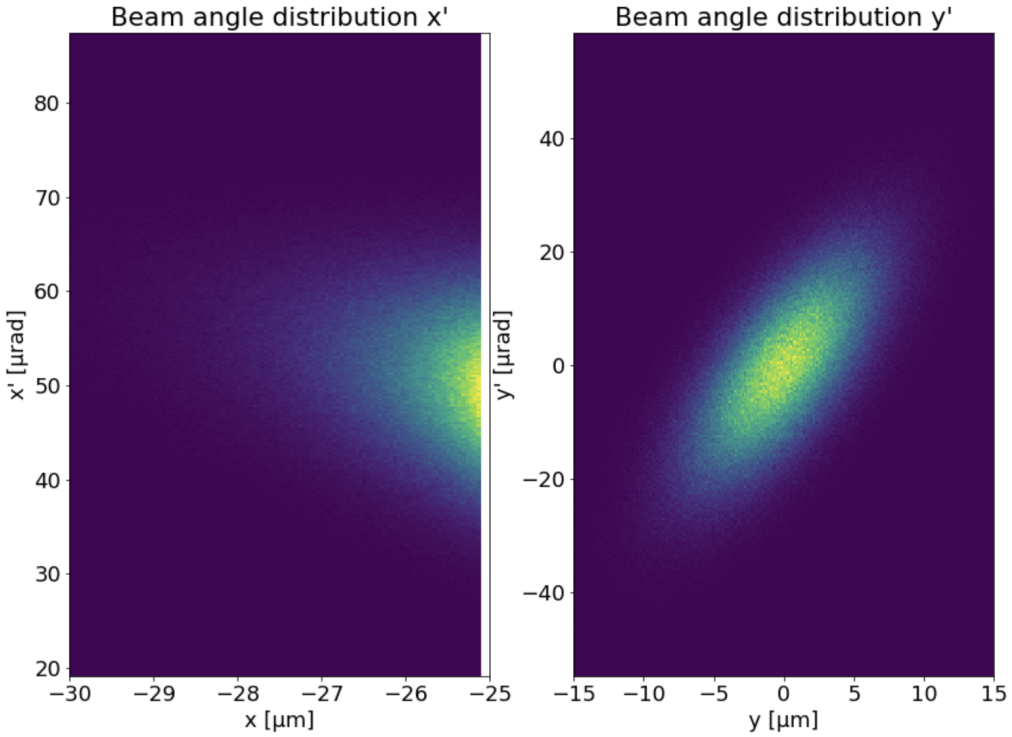

Figure 2: The phase space (x, x') (left) and (y, y') (right) showing the scatterplot of the angle versus the horisontal and vertical transverse position for an ensemble of particles. The emittance is defined as the area containing 90% of the particles. In the horisontal transverse direction we are only tracking particles in the lower half of the beam pipe, since this is where both the crystal and beam source is present. That is why we only see half of the ellipsoid.

The emittance is used for describing the beam particles, and the beta function for describing the optics. The amplitude of the particle oscillations, or the width of the beam is given by the beta function and the emittance $\sigma = \sqrt{\varepsilon\beta(s)}$. This width is describing the width of a Gaussian distribution since the distribution of particles in the transverse plane (x, y) is Gaussian.

Hence, we have a width in both transverse directions σ_x and σ_y, and we define the primary beam as that within 3σ and the beam outside is defined as the secondary halo.

Collectively these quantities constituting the Twiss parameters describe the optics of the machine and the properties of the beam width. They are also important for describing what is called the Betatron motion of the system which tells us of the behaviour of an ensemble of particles making out the beam.

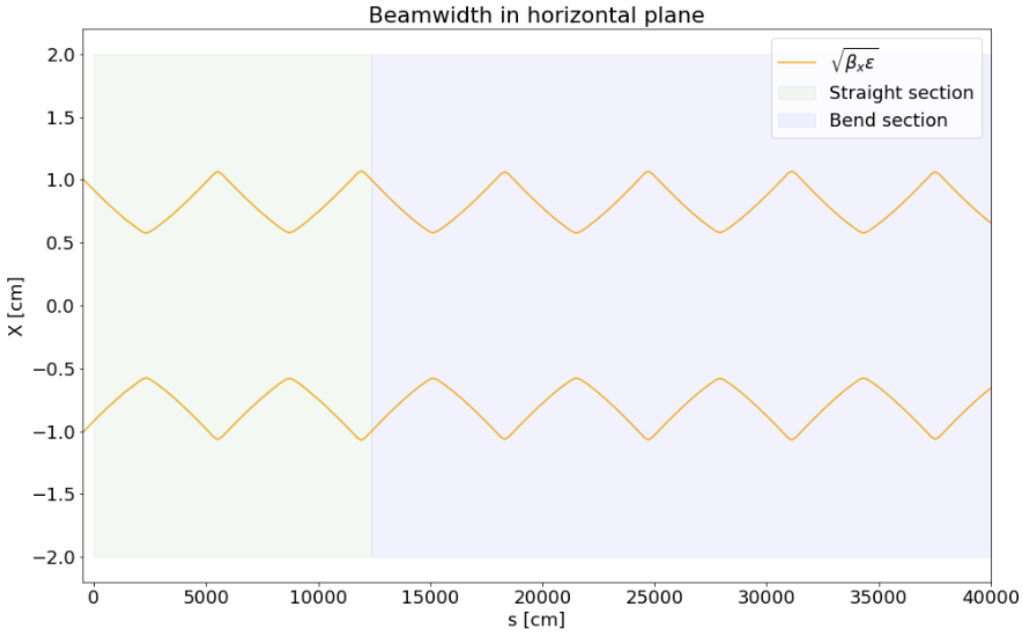

Figure 3: The beam envelope for a beam of protons centered around the transverse plane. We see the beam width x in meters as a function of the longitudinal coordinate s in centimeters in the accelerator complex. The point $s = 0$ is chosen arbitrarily inside the beam line within the SPS with a piece of machinery in the complex as a reference element. The straight section and bending section of the accelerator is indicated by the light green and blue shade respectively.

2.2 Betatron motion

When you have two particles with the same initial position but different initial angles moving in an accelerator with a dipole field you get Betatron motion[5]. One particle will oscillate around the other in the transverse plane with respect to the closed orbit that is going through the center of the quadropoles. This can be counteracted using quadropoles focusing the particles deviating from the optimal trajectory.

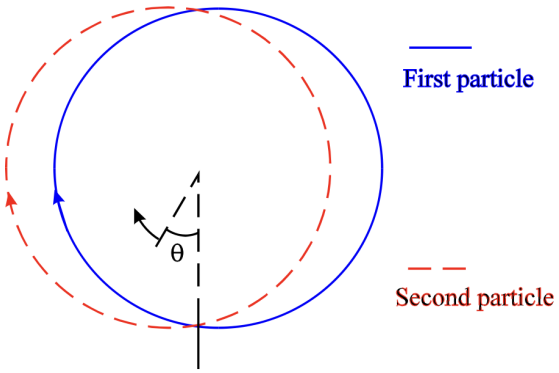

Figure 4: Two charged particles in a dipole field. From the point of view of the first particle, the second particle moves in an oscillatory pattern around it. This is due to the particles having differing initial angles[5].

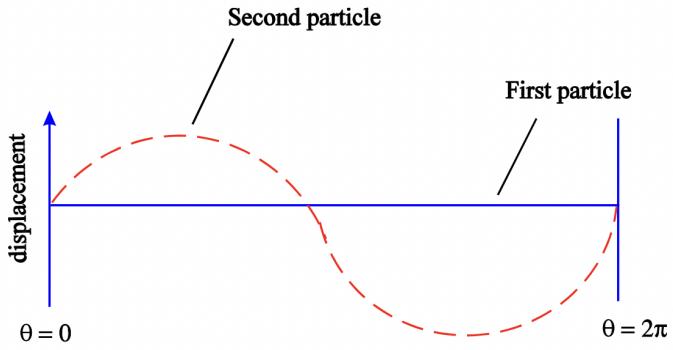

Figure 5: Two charged particles in a dipole field. From the point of view of the first particle, the second particle moves in an oscillatory pattern around it. This is due to the particles having differing initial angles[5].

Quadropoles change how much the beam is spread transversely in x and y. For example a focusing quadropole (QF) focuses the beam horisontally so that the particles that deviate from the central axis of the quadropole in the x-direction is centered back in, but then it increases the spread in the transverse y-direction. A defocusing quadropole (QD) does the opposite. As the particle traverses through the accelerator it will continuously encounter a series of QFs and QDs in the straight sections of the accelerator, called a Focusing-Defocusing (FODO) lattice where in between quadropoles we have non-focusing drift sections. The FODO lattices focus the beam particles deviating in the transverse plane.

We get an oscillatory behaviour of the beam width due to quadropoles focusing and defocusing as seen in the figure 3. The amplitude of the oscillatory behaviour in the horisontal plane is at its highest when at a focusing quadropole and lowest at the defocusing quadropoles.

2.2.1 Off-momentum

So far we have only considered on-momentum particles giving the beam dynamics as described above with the homogeneous Hill's equation (1) and its solution (4).

When we introduce off-momentum particles we get the inhomogeneous Hill's equation

$$x'' + K(s)x = \frac{1}{\rho}\frac{\delta p}{p} \tag{8}$$

where $\delta p/p$ is the off-momentum of a particle and ρ is the bending radius from a dipole magnetic field which shifts the horisontal closed orbit of the off-momentum particle.

The addition of off-momentum contribution to the Hill's equation also transforms the transport matrix into the revolution matrix which introduces another parameter into the phase space of the particles so that the particle state is now described by $(x, x', \delta p/p)$ [16]. The new element in the revolution matrix is referred to as the

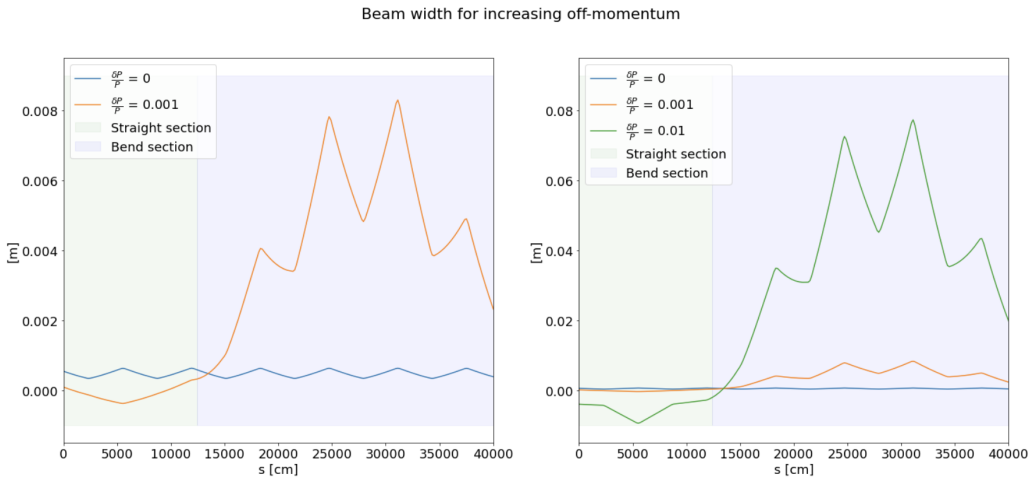

Figure 6: Beam width due to off-momentum giving rise to dispersion. The horisontal transverse coordinate x in units of cm is plotted as a function of the longitudinal coordinate s in cm. The light green shade corresponds to the straight drift section in the beam line, where FODO cells are present, and the light blue shade is the bending section with dipoles. Here the off-momentum particles are affected by the dipole fields resulting in the closed orbit trajectory deflecting; an effect called dispersion.

dispersion D and the eigenvectors to this matrix introduces the dispersion function $\eta(s)$

$$\eta(s) = \frac{dx(s)}{d\frac{\delta p}{p}} \tag{9}$$

The dispersion function states that there is a change in the transverse trajectory for a particle in a closed orbit as a result of increased off-momentum either due to energy loss of the particle, or for example after the particle undergoes an elastic interaction thus changing momentum direction, so that the transverse contribution increases. The increase in off-momentum results in the particle being deflected more by the dipole magnetic field.

The introduction of the off-momentum particles and thereby the dispersion D leads to an updated expression for the beam width with an added contribution from the dispersion

$$\sigma_x = \sqrt{\epsilon\beta(s)} + D\frac{\delta p}{p} \tag{10}$$

The beam width is now given by the optics of the accelerator given the emittance ϵ, beta function β(s), the dispersion D, and the off-momentum of the particles $\delta p/p$. As before, the beam width is given by the optics of the machine but now also the dispersion. The contribution from the optics becomes negligible to the beam width when we have off-momentum particles of about 1% and higher.

Now when plotting the beam width amplitude in the figure 6 the amplitude is at its highest not at the quadropoles but in the bending section of the accelerator where the dipoles are situated, and resulting in dispersive peaks.

This added dispersion term means that the beam envelope evolves differently and expands dramatically in the arc sections of the accelerator where the dipole field is strongest. This causes the envelope to expand the closed orbit to a size that is comparable with the beam pipe radius, thus leading to losses in the beam line in these regions and an increase in the energy deposition. The particles are then absorbed in unknown places for example in superconducting magnets in the LHC, thus heating them up and ruining their superconductivity - a process referred to as quenching of the magnets. It is the negative effects of dispersion that we want to minimize by use of crystal channeling. The dispersion is on the order of micro radians, so the angular spread of dispersed particles will still be within acceptance of the requirements for being intercepted by a crystal on the beam line.

2.2.2 Tune & Chromaticity

Having only dipoles and quadropoles we get another effect called chromaticity in the accelerator that we need to examine. Quadrupole focusing strength is dependent on the momentum of the particle. Thus, the ensemble of particles transforms the tune into a band spectrum since the beam is not monochromatic

$$\Delta Q = \frac{1}{4\pi} \oint \beta(s) K(s) ds \frac{\delta p}{p} = \xi \frac{\delta p}{p} \tag{11}$$

where ξ is the chromaticity. This band can include some of the unwanted tune resonances which is why there is also sextupoles present on the beam line to combat this. Dipoles and quadropoles combined with particles that have a momentum distribution lead to the spectrum band of tunes, while sextupoles correct for this.

As mentioned in a prior section the tune Q can result in runaway losses in the accelerator. That is why the accelerators are designed so that we avoid resonance effects destabilising the beam by making sure the tune is not an integer number. The tune Q changes by changing the magnetic field. The tune cannot be in integer or half integer steps or we will get resonance effects. For example after a couple of turns a magnet could give the wrong kick multiple times and thus create a resonance effect. Ideally you want a particle to not be able to end up in the same state after some turns.

These tune resonances resulted in major damages in the SPS in the year 2008 in the span of as little about 69 microseconds, where an unintended tune shift towards the $Q = 26$ resonance occurred during a magnet ramp down. This was in part due to the LHC type beam configuration that had a nominal tune of $Q = 26.13$, which is very close to the $Q = 26$ resonance. Therefore, only a slight change in tune was needed to hit a resonance. So, where the dispersion has its origin in the main bending fields from the dipoles in the accelerator, the closed orbit distortion is originating from field errors in the dipole fields which are predominantly induced by misalignments in the positions of quadropoles[4] .

Hence, losses in an accelerator are both due to effects of the different poles but also due to small errors in their placement. If a QF is placed slightly off, the particles that are on their ideal axis will not see a zero-sum field and will instead be displaced transversely away from their ideal trajectory which in turn means, that once they reach the dipole fields they will have their closed orbit changed.

This is a common quality of all accelerator's beam dynamics leading to losses of particles that potentially harm the accelerator detectors. To avoid this it is imperative to have a system in place which removes these off-orbit particles which make out what we refer to as the beam halo. This is the purpose of a collimation system.

2.3 Collimation system

A collimation system is necessary in a particle accelerator since as described in the previous section particles are lost due to effects such as dispersion. The particle beam is a Gaussian distribution of initial parameters and as such not all particles will be on the ideal trajectory and will be lost around the accelerator complex. Here they can be lost in regions with expensive equipment ruining electrical apparatus. Specifically in the LHC complex the losses lead to quenching of the superconducting magnets, thus directly intervening with the beam operation[20]. Therefore, these particles that are lost must be disposed off in a controlled manner. For this reason accelerators have a collimation system allowing for lost particles to be deposited at controlled beam dump sites.

The current collimation system in the LHC at CERN makes use of a multi step collimation system. In the beam halo you have absorbers which intercept the beam halo particles. Here, some particles are completely stopped whilst secondaries are also produced which then contaminate the beam halo. As the particles with now greater off-momentum revolve around the complex they are pushed further out in the secondary halo where they are again intercepted by absorbers. Here, yet again they are absorbed and some secondaries and higher order particles are produced until finally collimating onto Tungsten absorbers outside the beam halo where they are absorbed. This multi step collimation system is necessary because the Tungsten absorbers have a low nuclear interaction length, meaning that the energy deposition in the absorber inside the beam halo would correspond to temperature increases that would melt the absorber. Instead intermediary absorbers of Graphite are put in the halo stopping some of the primary protons but producing particle showers. Graphite has a higher nuclear interaction length, meaning that statistically speaking, the frequency of nuclear interactions in the material is lower than compared to Tungsten. This means that the Graphite absorber is not as efficient at stopping the halo particles, but it can withstand the energy deposition of the impacting particles without melting. This setup requires frequently placed big absorbers in the beam line reducing the overall impedance of the system in the LHC. If we

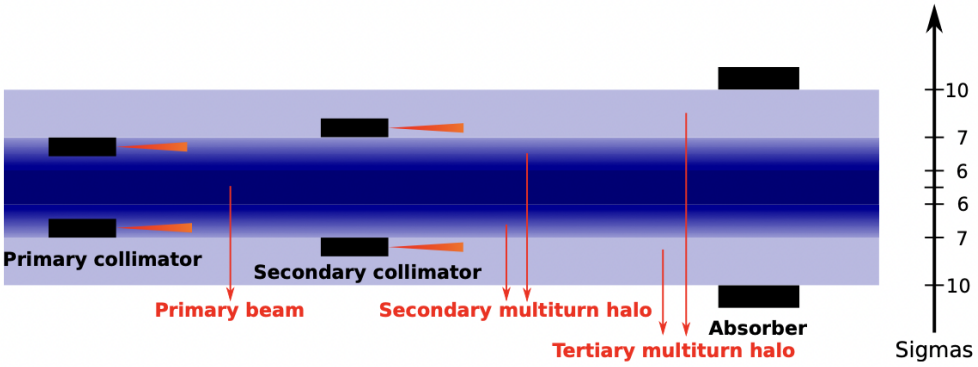

Figure 7: Current multi step collimation system in the LHC consisting of primary and secondary collimators of Graphite placed in the secondary and tertiary beam halo respectively. The Tungsten absorber is placed outside of the beam halo to avoid the absorber melting due to energy deposition inside the material from impacting particles[25].

instead introduced a method for diverting particles as the primary collimation step, we would be able to omit the intermediate collimation steps reducing the production of higher order particles in the beam halo resulting in a higher cleaning efficiency of the halo. The cleaning efficiency is a term for how many particles are lost in

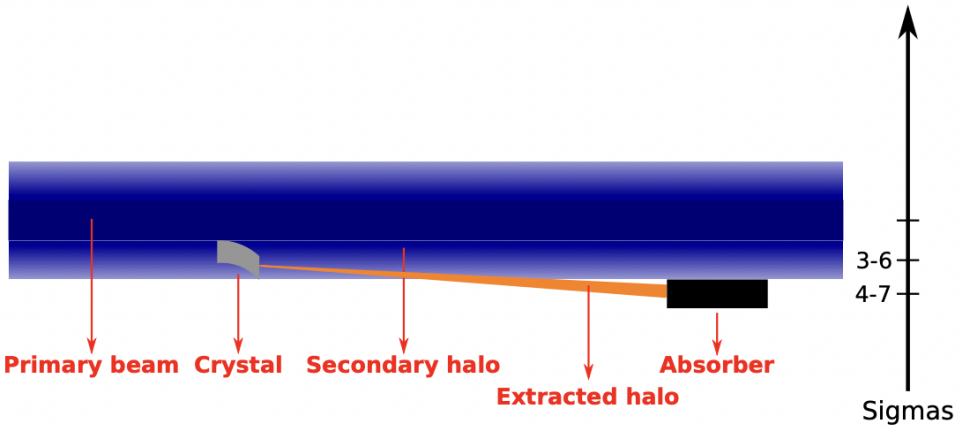

Figure 8: Crystal assisted collimation system. Here the primary collimation step has been switched out with a bent Silicon crystal, which steers beam halo particles directly towards an absorber. This way, less collimation steps are needed[26].

areas with sensitive equipment. A high cleaning efficiency corresponds to few lost particles. A collimation system with less intercept of the particles and more focus on deflecting them would result in a higher cleaning efficiency than the currently installed collimator system. Also the losses would be more localised in the accelerator complex so we would have designated hot regions.

A proposal for such an collimation system would be by applying a bent Silicon crystal in a crystal assisted collimation system. The Silicon crystal has a negligent amount of nuclear interactions with the intercepting particles and will thus operate

functionally within the beam halo simply deflecting the channeled particles to the last collimation step at an absorber[20]. This has been confirmed in experiment and is what we now wish to study and compare with earlier experiments by simulation.

3 Channeling theory and concepts

In this section the basic theory of channeling is reviewed and relevant concepts of importance to the thesis is introduced and described in detail. This study is focused on channeling of high energy ultra-relativistic particles. To describe the behaviour of these high energy relativistic particles a brief introduction is given on the description of particles in this energy regime.

3.1 High energy particles

A relativistic particle beam in an accelerator has its energy given by[7]

$$E^2 = p^2c^2 + m^2c^4 \simeq p^2 + m^2 \tag{12}$$

so, as particles are accelerated and move closer to the speed of light, the energy added to the particles contributes to increasing their mass. In a particle accelerator colliding particles can be thought of as a soup of energy that is the sum of the colliding particles' energy, and from this sum you have a ledger from which other particles can be produced. This is where the interesting physics reside, where based on branching ratios we can set up statistical models that theorise which particle pairs we will see produced and at what frequency.

This high-energy functional equivalency between energy and momentum allows particle energy to be calculated from tracker data. Once a particle's rest mass is determined from its identity (which follows, for example for muons, by them having been detected in the muon chamber coupled with other supporting data), the particle's velocity and thus its momentum can be calculated from the rate of change of its curvature in the magnetic field. Thus, in the Compact Muon Solenoid (CMS) detector, muon energy can be calculated from tracker data. In the case of muon tracker, both momentum and rest mass can be used in the energy calculation, since the rest mass of the muon, or any known particle, follows whenever the particle's type can be identified, and with muons this is relatively easy. (They are the only particles to be detected in the muon chamber.) But for high-energy muons, the principle holds: energy can be calculated directly from momentum when rest mass is negligible. (This principle is useful for the inner tracker as well: neutral particles leave no tracks there, but their energy values in the calorimeter, coupled with the location of those energy deposits, suffice to calculate momentum and transverse momentum particularly.)

The $E^2 - p^2 = m^2$ formulation reveals an easier way to calculate the rest mass of a parent particle. Another way to consider the parent particle at rest is just to remove the component of its energy due to its motion, a component which is related to its momentum, p. Subtracting p^2 from E^2 yields the particle's rest mass without the need of the mathematical formalism of the Lorenz transformation. As we will see below, it turns out that for muons, momentum data provides us with both terms

in this equation, p^2 and E^2.

What is known at the LHC is that in the primary collisions particles are carefully steered along the z axis (the beam line), and thus have very small components of transverse momentum p_t, meaning a momentum contribution that is radial, or orthogonal to the beam line. So initial transverse momentum for primary collisions is treated as zero. Transverse momentum for secondary collisions can be calculated from tracker, calorimeter, and timing data. Any difference between zero and the sum of all calculated transverse momentum is thus "missing" transverse momentum. But since at high energies E = p, that difference from zero of the sum of all transverse momenta is known in high energy physics as missing energy, or missing E_t.

When particles collide in the accelerator the ideal particles have all their momentum projected on the longitudinal axis. But in reality it will also have some momentum that is deviating radially in the transverse plane. Therefore a particle in the accelerator has a momentum that can be described by a longitudinal momentum p_z and a transverse momentum p_t.

This missing E_t, when coupled with other telltale signs of for example neutrino production such as the production of a single lepton, can provide indirect evidence for neutrinos, which are not directly detected at CMS. Once neutrino identification is added to the full set of identifications for particles directly detected at CMS, coherent event reconstruction under the Standard Model becomes possible, since now all collision products are accounted for (in the absence of new physics). So while all momentum is conserved in collisions at the LHC, it is transverse momentum whose initial value is known, and whose conservation is relied upon in calculations done with CMS data.

3.2 Crystal theory

A big part of the study conducted in this thesis consisted of the implementation of Silicon crystals as the novel technology for general beam manipulation. To understand how this works we need to consider the physics relating to crystals, their inner symmetry, and resulting electropotential properties[3].

A crystal is defined as a solid where the atoms are arranged in a periodic pattern. For example, table salt NaCl has cubic symmetry in the arrangement of atoms. A unit cell is the unit arrangement of atom(s) that is repeated. For example, one unit cube of a sodium ion and a chloride ion in a salt crystal. These unit cells stack together with no gaps. This limits the amount of configurations of unit cells to 219 (230 if including chirality) systems, called space groups of the crystal. The unit cells can be cubic, rectangular, hexagonal etc. The unit cell completely reflects the symmetry and structure of the entire crystal, so cubic crystal means cubic unit cells. The unit cells geometry is described by six parameters: the three principal axes and the three angles between these axes. Crystals are categorized into seven lattice systems: triclinic, monoclinic, orthorhombic, tetragonal, rhombohedral, hexagonal,

and cubic.

Crystals are described by three Miller indices (lmn) for example (101). The syntax denotes a plane that intercept at the point $a_1/l, a_2/m, a_3/n$. That is, the Miller indices are proportional to the inverses of the intercepts of the plane with the unit cell (in the basis of the lattice vectors). If one or more of the indices is zero it means that the planes do not intersect that axis.

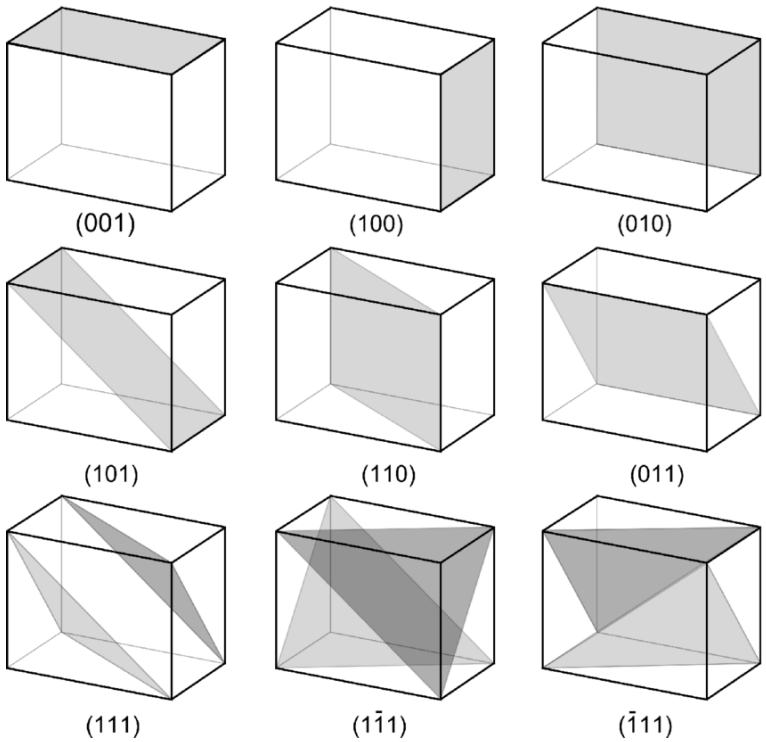

Figure 9: In this figure are shown some examples of Miller indices, showing how the indices (lmn) correspond to orientation of planes[31].

3.3 Channeling theory

Now we introduce a charged particle like a proton interacting with the Silicon crystal to study what kind of particle physics phenomena occur, and how this can be utilised for a general-purpose beam manipulation. A particle impacting on an atom in the Silicon crystal will feel a potential from the charge of the nucleus of the Silicon atom. This is described by the simple Coulomb potential that comes from Coulomb's law describing the force between two charged particles governed by the squared distance law

$$|\mathbf{F}| = k_e \frac{|q_1 q_2|}{r^2} \tag{13}$$

where k_e is the Coulomb constant $k_e = \frac{1}{4\pi\varepsilon_0}$, ε_0 is the vacuum permittivity constant, q_1 and q_2 is the charge of the two particles respectively, and r is the radial distance between the two charges.

The potential produced by a single atom in the lattice structure of the crystal is

simply implied by the Coulomb law

$$V(r) = k_e \frac{Q}{r} \tag{14}$$

where Q is the charge of the nucleus and r is the radial distance to the nucleus.

From solid state physics we can use a special case of the Lindhardt approximation called the Thomas-Fermi model which describes the damping of electric fields due to mobile charge carriers, which applies for the considerations of a lattice structure of Silicon atoms. Here an exponential damping term is added to the potential so we get

$$\phi(r) = k_e \frac{Q}{r} \cdot \exp(-k_0 r) \tag{15}$$

where k_0 is the Thomas-Fermi wave vector which acts as the damping factor. This is known as the screened Coulomb potential and is a result of putting the Thomas-Fermi approximation into the Poisson equation. Setting $k_0 = 0$ gives us the standard Coulomb potential back for a single atom. This leaves us with an expression for the potential that a single impacting particle will feel from a single atom in the lattice but corrected for the whole crystal solid

$$V(r) = \frac{Z_i Z e^2}{r} \phi\left(\frac{r}{a_{TF}}\right) \tag{16}$$

where $Z_i e$ is the charge of the impacting particle and $\phi\left(\frac{r}{a_{TF}}\right)$ is a Moliere screening function[2]. If now we imagine that the impacting particle is parallel to two adjacent crystal planes and is thus in a channel of the crystal, we can use the Lindhard approximation which states that the particle will feel the average potential of all the atoms in the planar lattice structure as a smooth potential. Thus, the ordered lattice structure of atoms in a Silicon crystal manifests itself in the shape of a smooth potential well given by the Coulomb potential of each atom in the lattice and can be approximated by the harmonic solution

$$U(x) \approx U_{max} \left(\frac{2x}{d_p}\right)^2 \tag{17}$$

where x is the impacting particle's horisontal coordinate and d_p is the interplanar distance. Two types of crystals are examined in this study: a strip-foil crystal bent through (110) and a quasi-mosaic crystal bent through (111). The difference between strip-foil crystals and quasi-mosaic crystals is in the interplanar potential created by the distance between the planes. The atoms in the crystal structure are oriented in planes in a lattice structure. Each of these planes are separated by a distance d_p, where the space between two adjacent planes are referred to as a channel of the crystal. Now the strip-foil crystals have equidistant crystalline planes, so the channels have all the same size, while quasi-mosaic crystals have a ratio 1:3 for subsequent planes. This means that the potential an impacting particle feels

will vary depending on which channel it enters when impacting on a quasi-mosaic crystal, while for a strip-foil crystal the potential will be the same regardless of channel.

On the figure 10 a) below is depicted both the exact solution as the solid line and the harmonic solution as the dashed line for a straight strip-foil crystal with planes (110). Figure 10 b) shows the exact solution for a quasi-mosaic crystal with the planes (111). The quasi-mosaic potential has multiple smaller wells going out from the center of the crystal due to the interplanar distance following a ratio 1:3.

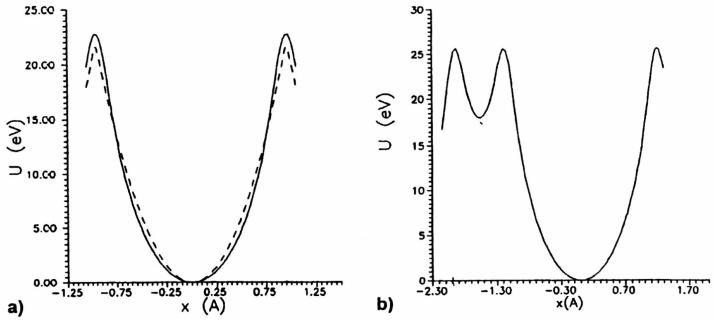

Figure 10: Potential for a straight crystal. The figure a) shows the exact solution to Moliere potential for a strip-foil crystal with planes (110) as the solid line, and the harmonic solution to the potential as the dashed line. Figure b) shows the exact solution for the potential for a quasi-mosaic crystal with planes (111)[21].

Now that the theory for the potential of a particle impacting on a crystal channel is in place we need to consider the case of a bent crystal. The symmetric potential well is only for the case of a straight crystal where two adjacent planes are similar. If we consider a Silicon crystal that is bent horisontally with some angle, the particle traversing through the channel will come closer to the bending plane while it travels in a straight line. The particle therefore encounters an asymmetric potential well when travelling through a bent crystal, and this change to the potential felt by the impacting particle is simply given by adding a centrifugal contribution[21]

$$U_{eff}(x) = U(x) + \frac{pv}{R}x \tag{18}$$

where R is the bending radius of the crystal. If the particle's transverse momentum is lower than the height of the potential well it will follow the bend of the crystal, else it will leave the channel by traversing through the planar wall.

3.4 Channeling phenomena

When a particle is impacting on the crystal face it will encounter a potential well as described in the section above. If the particle has a sufficiently small impact angle with the crystal face normal, meaning that its transverse momentum is sufficiently small, it will be captured in the potential well and undergo a phenomenon referred to

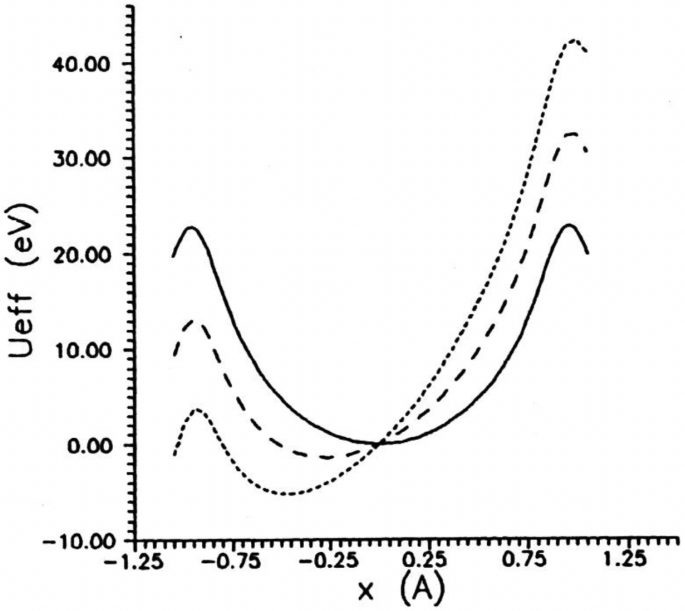

Figure 11: Potential for a bent strip-foil crystal with the added centrifugal contribution as a function of horisontal displacement with regards to the channel center. The solid line shows the potential for a contribution of 0, while the dashed and dotted line are from centrifugal contributions of $\frac{pv}{R} = 1$ [GeV/cm] and $\frac{pv}{R} = 2$ [GeV/cm] respectively.

as channeling. A particle undergoing channeling follows the channels of the crystal while traversing through it undergoing harmonic oscillations. The oscillations are given by the expression[27][21]

$$x(z) = \frac{d_p}{2}\sqrt{\frac{E_t}{U_{max}}}\sin(\frac{2\pi z}{\lambda} + \phi) \tag{19}$$

where E_t is the transverse energy which can be thought of as the transverse momentum of the particle, U_{max} is the height of the potential well, λ is the wavelength of the oscillation given by $\lambda = \pi d_p\sqrt{\frac{pv}{2U_{max}}}$ and ϕ is the phase advance. The expression is the solution to the equations of motion for a particle undergoing planar channeling. The expression is for a straight crystal where the particle is traversing right in the middle of the two planes. For a bent crystal the oscillatory term is the same except for the factor $\frac{d_p}{2}$ meaning that the particles oscillate in the same way as for a straight crystal but with a modified amplitude and with the minimum of the potential well shifted.

When particles are captured in the potential they will not interact nuclearly with the atoms in the plane, and if the crystal is also bent the channeled particle will follow this bend. The probability of an incoming particle undergoing channeling is a function of the particle's transverse momentum. This relation will be inverse since for higher transverse momentum the particle might exit the channel instead

of following it. Thus for known momentum it is a function of the incoming angle θ_{in}. This allows us to set up a criteria for when an incoming particle can undergo channeling given by its incoming angle. Because the forces acting on the particle only act in the transverse plane we can use conservation of energy for a channeled particle, and use the assumption of small impact angle $\theta_{in} \ll 1$ which gives us

$$\theta_{in} = \tan(\frac{p_t}{p_l}) \approx \frac{p_t}{p_l} \tag{20}$$

where p_t is the transverse momentum and p_l is the longitudinal momentum of the particle. Using this the total energy of the particle in a channel is given by

$$E = \sqrt{p_t^2 c^2 + p_l^2 c^2 + m^2 c^4} + U(x) \tag{21}$$

using that $p_l \simeq p$ and $E_l \simeq E$ we can rewrite the expression for a channeled particle travelling in the middle of a channel $x = 0$ to

$$\frac{pv}{2}\theta_{in}^2 \leq U_{max} \tag{22}$$

By isolating the expression for the incoming angle we now get the maximal incoming angle for which a particle can undergo channeling.

$$\theta_{crit} \approx \sin(\theta_{crit}) = \sqrt{\frac{2U_{max}}{pv}} \tag{23}$$

We define this as the critical angle θ_{crit}. The critical angle is the upper bound for the incoming angle of the particle for the transverse momentum to be low enough for channeling in the crystal. So the channeling criterion can be stated as $\theta_{in} \leq \theta_{crit}$ where θ_{crit} is usually tens of micro-radians for the energy considered in this study of LHC injection energy at about 450 GeV. From the expression we can see that the critical angle has an inverse relation to the particle momentum, which is the only variable that can change in our experiment design. For higher beam particle momentum the maximal incoming angle allowed to undergo channeling decreases, thus creating a more strict requirement on the incoming particles for them to undergo channeling.

3.5 Crystal interactions

Channeling is the main property we want to study since this is the application that allows us to manipulate a beam of charged particles most by deflecting them. Since a channeled particle follows the bend of the crystal, this can be used to steer the beam towards a specific region. But channeling is not the only interaction that a particle can undergo with the crystal. The channeling criterion is only an upper bound for channeling to be possible, but the interactions that happens inside the

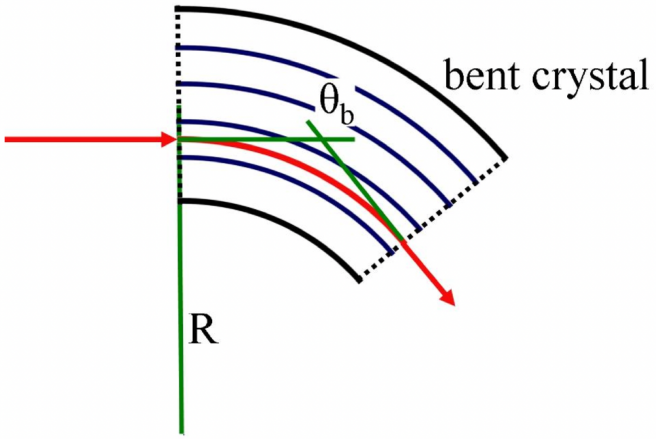

Figure 12: Channeling: When a particle impacts on the crystal alligned with the crystalline planes and with a sufficiently small incoming angle $\theta_{in} \leq \theta_{crit}$, it can be caught in the potential well created by the crystal planes. Here it will undergo oscillations throughout the crystal. In the case of a bent crystal like on the figure 12, the particle will follow the bend of the crystal thus gaining a horisontal angular deflection[21].

crystal are all probabilistic, so if the incoming angle is lower than the critical angle it does not mean that the particle will necessarily be undergoing channeling. More interactions are possible that will be described below.

If the crystal is slightly bent with a bending angle θ_b, the particles inside the channel can either follow the bending of the crystal and come out at a different angle than their incoming angle, or they leave the channel. This latter process is called dechanneling and is depicted on the figure 13. This happens when the impacting particle has a transverse momentum higher than the height of the potential well U_{max}. In this case the particle enters the channel and is initially caught but leaves the potential and continues out of the crystal. This can happen due to scattering on electrons or nuclei inside of the plane, which nudges the particle's transverse momentum to a level exceeding the height of the potential well, and as a result the particle leaves the channel. If the crystals were isotropic, only two interactions could happen, namely channeling and dechanneling as described above. The crystals we consider in this study are monocrystalline Silicon which is anisotropic, thus the physical processes that can occur inside the crystal, when a charged particle propagates through it are highly orientation dependent. Because the crystals are highly anisotropic they experience three additional types of interactions; volume capture, volume reflection, and amorphous scattering.

If a particle initially has too high transverse momentum it might be caught in a channel further inside the crystal due to the curvature of the crystal. These particles have angles $\theta_{crit} < \theta_{in} < \theta_b$ where θ_b is the bending angle of the crystal. This interaction is called volume capture.

Particles with an incoming angle higher than the bending angle $\theta_{in} > \theta_b$ do not

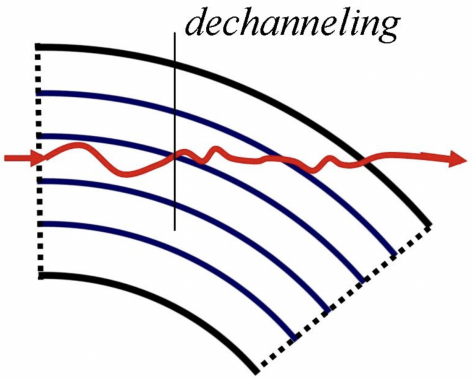

Figure 13: Dechanneling: A particle enters the channel and is initially caught in the potential well but leaves the potential and continues out of the crystal. This can happen due to scattering on electrons or nuclei inside of the plane which nudges the particle's transverse momentum to a level higher than the height of the potential well, and as a result the particle leaves the channel.

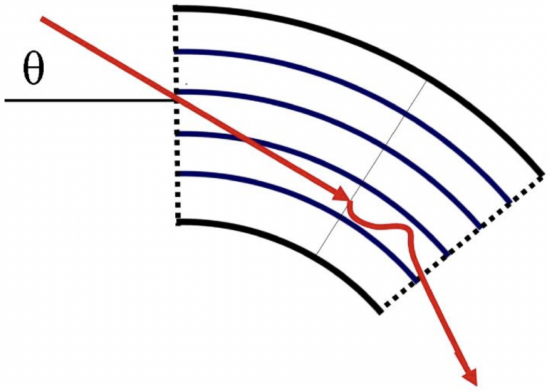

Figure 14: Volume capture: The incident where a particle that initially has too high transverse momentum to be caught in the potential traverses through some channels and then proceeds to be caught is referred to as a volume capture interaction.

get caught through the whole crystal but can undergo volume reflection where the particle might reflect on the crystal planes.

For angles of magnitude mrad and higher, the crystal interactions mentioned above have very small probabilities and the scattering of the particles is amorphous. Amorphous scattering is the most common elastic interaction happening for an impacting particle with a solid and if the crystal is not rotated to its channeling orientation, meaning that the beam is not parallel with the crystalline planes, the only interactions happening for an impacting particle would be amorphous scattering or nuclear interactions.

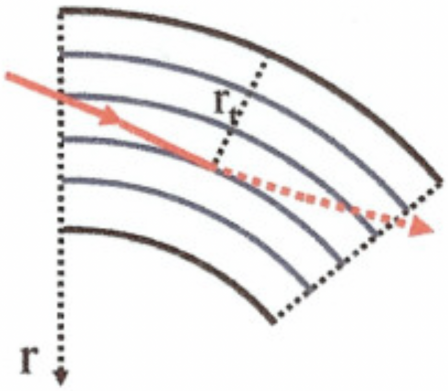

Figure 15: Volume reflection: For incoming angles higher than the bending angle of the crystal $\theta_{in}\theta_b$ the particle will have too high of an incoming angle to be channeled and instead reflects on the plane.

3.6 Crystal properties

The rate of amorphous scattering is used as a measure to define a property of the Silicon crystal called the crystal channeling efficiency. By comparing the amount of particles that are channeled to the amount of particles that scatter amorphously when the crystal is in its channeling orientation, we can quantify the efficiency of the crystal[26].

Highest efficiency corresponds to lowest transverse momentum. So the more parallel the incoming beam is with the surface normal of the crystal face, and thus how many of the particles undergo channeling, the higher the efficiency is.

Because of the small critical angle of the crystals (tens of micro radians), only particles with a trajectory almost parallel to the crystal planes are channelled. Therefore, the orientation of the crystal with respect to the beam axis is of large importance. But if the crystal is twisted vertically in its planes, then the highest efficiency is suddenly found as a function of the vertical impact position. This is more often the case since a real crystal does not consist of perfect crystal planes, the planes might be twisted slightly.

A quantity that expresses this twist is the torsion, defined as the rotation of the horisontal direction in the atomic planes of the crystal surface. The torsion is related to the change of the mean angular deflection of channelled particles as a function of vertical impact position, thus given in units of [μrad/mm].

Torsion is caused by the mechanical holders of the crystal on the beam line[20]. There is a holder present on the top and bottom of the crystal when it is installed either for test irradiation or for use on the beam line thus creating a vertical torsion. One can also add mechanical stress on the sides of the crystal creating a horisontal bend to deflect the particles as a kind of fine-tuning.

So while the primary bend of the crystal is given by a mechanical bend from the crystal holder, this holder can induce unwanted deformations like torsion in the crystal.

A final property of the crystal is with regards to the nuclear interactions happening in the crystal. The particles that hit the crystal can interact with the atoms in the crystal planes elastically or inelastically. We define the rate of inelastic nuclear interactions in the crystal as the INI-rate. The process of inelastic nuclear interactions produce new particles referred to as secondary particles during particle showers. More channeling also means a lower rate of inelastic nuclear interactions happening in the crystal and thus a lower INI-rate for the crystal.

3.7 Silicon crystal manufacture

Silicon crystals for use in the LHC and SPS collimation systems need to have a high degree of purity and quality and need to fulfil strict requirements before being installed for experimental use at CERN.

Initially Silicon wafers are cut from Silicon ingots where a miscut angle can be introduced. The miscut angle is caused by the imperfect polishing of the face. The angle is between the crystalline planes and the tangent to the lateral face. An "ideal" perfectly cut crystal would have crystalline planes parallel to the lateral face (tangential to the beam direction) of the crystal, but in reality they all have some angle. A miscut angle up to 100 μrad does not affect the collimation performance. Having too high of a miscut angle will result in some particles' probability of undergoing channeling being dependent on the impact parameter. Thus for regions of low impact parameter, particles will instead interact amorphously with the crystal and be lost in possibly sensitive areas of the accelerator. The wafers with an acceptable threshold of miscut are then studied to choose only those with the highest degree of crystalline perfection.

One of the most unwanted effects that can also be present in a crystal with regards to obtaining channeling, is dislocations in the atomic lattices of the crystal. A dislocation in the crystal induces a deformed electric field in which a charged particle undergoing channeling would interact with the deformed field and cause it to undergo dechanneling instead, thus reducing the channeling efficiency. Therefore, the process of selecting initial Silicon wafers with the intent of manufacturing Silicon crystals is requiring a high amount of resources. First the wafers are etched with chemicals that can highlight the amount of dislocations present. If the amount is under the very strict threshold of acceptance (even for standards used in microelectronics) of $1/\mathrm{dm}^2$ the wafers are then selected for x-ray topography before being finally accepted[20].

4 Experimental setup and data taking

In this thesis a combination of both experimental and simulated results are presented. The experimental data taking took place in the H8 extraction line, which is situated in the North Area of CERN at the SPS accelerator seen in figure 1.

The H8 is an extraction line situated in the SPS accelerator where the UA9 collaboration is performing radiation studies. The work at H8 is focused on the testing and characterisation of Silicon crystals for use in general-purpose beam manipulation. This is the experimental facility where the data to be used for the analysis and characterisation of Silicon crystals is taken which will be used in the next chapter, where we do a full characterisation of two crystals for a description of their mean deflection angle, torsion, and channeling efficiency.

4.1 UA9 setup

On the figure 16 we see that the H8 line is set up in a way such that a beam of protons/pions come from the left in the z-direction. The particle first crosses a detector plate which triggers data-acquisition. It then crosses two transverse detector planes that detect impact position, and thus an angle of impact can be calculated after the passage through the second detector plane. The particle then impinge (collide sharply) on the crystal where the location of impact can be extrapolated from the two previous detector planes via the found angle. The particle then has a probability of undergoing one of the five interactions in the crystal (channeling, dechanneling, volume capture, volume reflection, amorphous scattering).

The particles then deflect from the crystal and its trajectory is intercepted by three additional transverse detector planes downstream of the crystal. Some crystals can have greater deflection angles due to their length, and in some cases the deflected particle will be detected at the third detector plane and not the last (the fifth) detector plane. Thus by putting in another detector plane closely downstream off the third we are almost sure to get detection in at least two outgoing planes for angle and direction extrapolation.

Hence from a setup with two detector planes measuring impact position, followed by a crystal and then another three planes, we can extrapolate detailed information about the particle such as the incoming trajectory, the impact with the crystal face in the transverse plane, and the outgoing trajectory.

By varying the impact position we can measure the resultant angular deflection or the channeling efficiency of the crystal. Both of these methods can be used to characterise the torsion via a linear fit of the mean deflection angles. Having the torsion we can correct the data and then only include angles lower than the critical angle thus representing the population of incoming particles that can undergo channeling (the rest are assumed to have undergone volume capture, volume reflection, dechanneling, or amorphous scattering). Then by fitting the distribution of these particles we can extract the bending angle and determine the channeling efficiency,

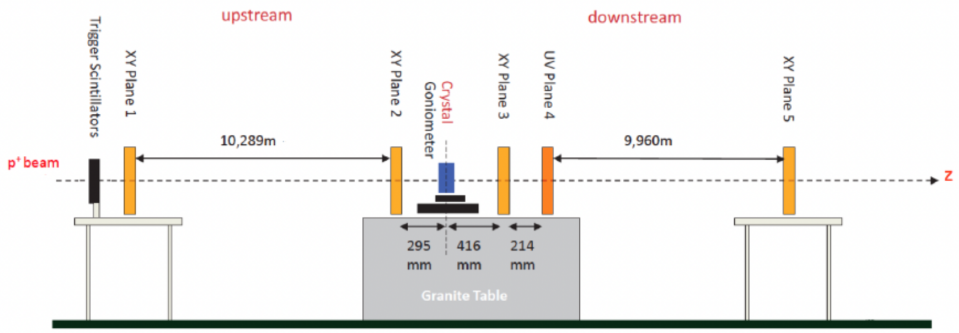

Figure 16: The UA9 experimental setup at the H8 extraction line. The setup consists of a detector plate which triggers data-acquisition and five downstream transverse detector planes measuring the impact position. Between the second and third detector plane the Silicon crystal is placed on a goniometer where it is bombarded by protons coming from the left. From the impact positions an incoming and outgoing angle can be computed. This is the process for characterising crystals.

thus resulting in a complete characterisation of the Silicon crystal.

4.2 H8 data taking

During the stay at CERN a visit to the H8 extraction line was arranged to see the control center as well as to see the experimental beam line where the crystal is mounted for radiation campaigns.

The crystal is mounted on a goniometer where it can be tilted and translated vertically and horisontally. The crystal is placed right at the exit of the beam pipe. Parallel to the beam pipe is an optic laser originating from the internal wall for initial placement of the crystal. The optic laser hits a pentaprism which has the optical property that even if the entry angle of the laser is not at 90 degrees to the entry face of the prism, the deflecting angle will always be exactly 90 degrees.

This deflected laser orthogonal to the beam line pipe then hits the crystal and continues to a mirror on the opposing side against the external wall. This mirror then reflects the laser back into the prism and back to the light source, where it should coincide close to the point source. This procedure makes it possible to see if the crystal is crudely aligned horisontally and vertically with the incoming beam of particles. The setup and the prism can be seen on the figures 17 and 18.

This crude positioning is followed by a proper alignment with small fine movements from the control center while bombarding the crystal with protons. The detector planes then produce a data set which when plotted shows a scatter plot of the deflection angle versus the horisontal impact position. This plot will look homogeneous if the crystal is not installed.

If instead the crystal intercepts the beam, then the deflection versus horisontal impact plot produces a rectangle that has the width of the crystal and a higher

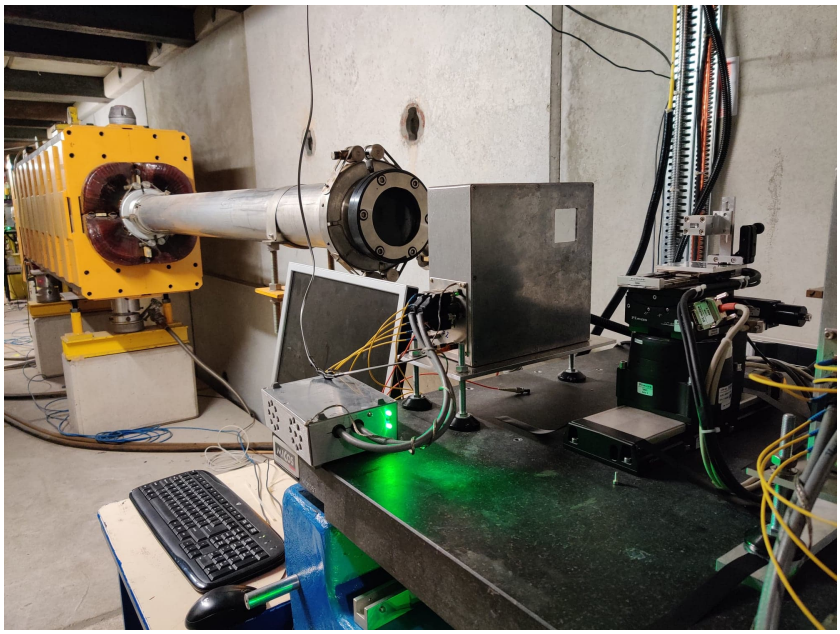

Figure 17: A photograph taken at the H8 extraction line. The exit of the beam pipe is seen corresponding to the left most part of the animated layout on the prior figure 15 at the exit of the beam pipe. The beam pipe exit is followed by a detector plate and then the crystal mounting on the goniometer. The extraction line was not in use so some of the detectors are not in place. Behind the goniometer is the external wall where the laser used for horisontal and vertical alignment is reflected.

Figure 18: A photograph of the H8 extraction line. Seen on the left is the internal wall where the aligning laser originates from the light source placed at the yellow sticker in the photograph. The laser then hits the pentaprism seen to the left, which deflects it 90 degrees towards the crystal on the goniometer to the right.

deflection in the vertical for that horisontal width. This is an indication that the crystal is in horisontal alignment.

The positioning is finalised with an angular alignment where the deflection is plotted against the impact angle of the particles. The angular orientation of the crystal is changed by an average of 1 mrad every 15 minutes until a channeling region appears on the scatter plot with a distinctly higher deflection for a small horisontal interval.

4.3 Detectors

All instruments (except beam loss monitors, scintillators, and other off-beam apparatus) are by default in a parking position, meaning that they are present on the beam line but displaced horisontally in the transverse plane away from the center of the beam line.

When an instrument is to be used, it is moved towards the beam center using its motors from an external control panel. The position is determined from the motors' three sensors that provide us with the controller, motor and Linear Variable Differential Transformer (LVDT), which together extrapolate the position of the instrument with respect to the beam center from the parking position. Some of the relevant instruments of the beam line are described here[25].

Beam loss monitors are used together with photomultiplier tubes to determine the loss of beam signal when performing measurements, for example when doing angular scans, or for indicating losses in the area right around the beam loss monitor.

The beam current transformer (BCT) measures the intensity of the beam circulating inside the machine. It is placed in order to measure the status of the beam during data taking for normalization in the offline analysis afterwards. Two types of BCTs are used, Fast BCT and BCTDC. They both measure the same quantity but in different time windows.

The beam position monitor (BPM) measures the beam position as well as monitors the stability of the orbit to avoid unwanted losses of beam. The beam position monitor is mounted on the collimator jaws.

A Timepix chip acquires data within a time frame referred to as the shutter time and works in three modes. Medipix mode counts the number of hits inside the shutter. Time of Arrival (TOA) where each pixel in the chip measures the time from the first hit until the end of the shutter signal. Time Over Threshold (TOT) is a mode where each pixel counts the number of clocks a signal is over the threshold inside the shutter. The Timepix is kept in a roman pot with a small pressure inside the SPS vacuum system but outside of the beam pipe.

During data taking when bombarding crystals in the H8 beam line, the machine runs in coast mode. This means that there are stationary conditions for beam orbit and a constant magnet current.

4.3.1 Alignment

All the experimental instruments need to be aligned between each beam injection because the parameters of the machine change each time. So, first off one needs to determine where the center line of the beam is with respect to the beam pipe center. This requires moving the jaws of the left and right collimator to intercept the beam, producing a loss of beam signal but an increase in energy deposition, thus indicating the location of the beam.

Once a collimator jaw intercepts the beam a peak in the nearby placed beam loss monitor is seen, since these detect the radioactive energy deposition happening from the nuclear interactions of the beam with the collimator jaw.

Two peaks are generated at specific transverse coordinates by moving both the left and right collimator jaw, which allows one to extrapolate where the beam is positioned between the two jaws with respect to the beam pipe center. The other instruments can then be aligned in a similar manner.

4.3.2 Angular Scan

An angular scan around the crystal is done by bombarding protons onto the crystal surface while rotating it to find when the amorphous scattering signal becomes replaced with an increase in the horisontal deflection angle. This would be an indication of when the crystal is in the channeling regime.

The angular resolution of the telescope responsible for tracking the angles is given as the difference between the incoming and outgoing angle when no crystal is installed. It is the angular deflection of the particle $\Delta\theta = \theta_{out} - \theta_{in}$ when there is no crystal.

On the figure 19 below is seen the result of an angular scan done in the year 2015 for the strip-foil crystal STF101, and shown for the region close to the channeling orientation. There are five distinct regions appearing for when doing an angular scan: Channeling, dechanneling, volume capture, volume reflection, and amorphous scattering.

The figure shows the angular horisontal deflection $\Delta\theta$ in micro radians as a function of the horisontal impact angle θ_{impact} in micro radians. The highest horisontal deflection is given by the channeling region indicated by the label number 3. The width of the channeling regime on the figure is given by $2\theta_{crit}$. This is as expected, it is where the deflection is highest and it is the region used to characterise the mean deflection angle of the crystal by fitting a Gaussian distribution to the particle population in this regime.

The dechanneled and volume captured particles are also deflected significantly since as seen in the previous section on crystal interactions in figures 13 and 14, we see that for the case of dechanneling the particle is initially channeled and follows the bend of the crystal for a while, thus increasing its outgoing angle before exiting the channel and leaving the whole crystal solid.

For the volume captured particle the opposite effects happens where initially the incoming angle is too high, the particle traverses through at least one channel before finally being caught and channeled for the remainder of the crystal thus also following the bend of the crystal but for the end of its geometry.

Since the incoming particles come in a distribution of incoming angles, the outgoing angles are also distributed uniformly which gives the filament-like structure for the dechanneling and volume capture regions. The volume reflection region is the only region that gives a negative value for the horisontal deflection angle, since during a reflection as indicated on the figure 15, the outgoing angle is opposed to the incoming angle. The amorphous region labeled by 4 gives a uniform scattering around $\Delta\theta = 0$ μrad horisontal deflection angle.

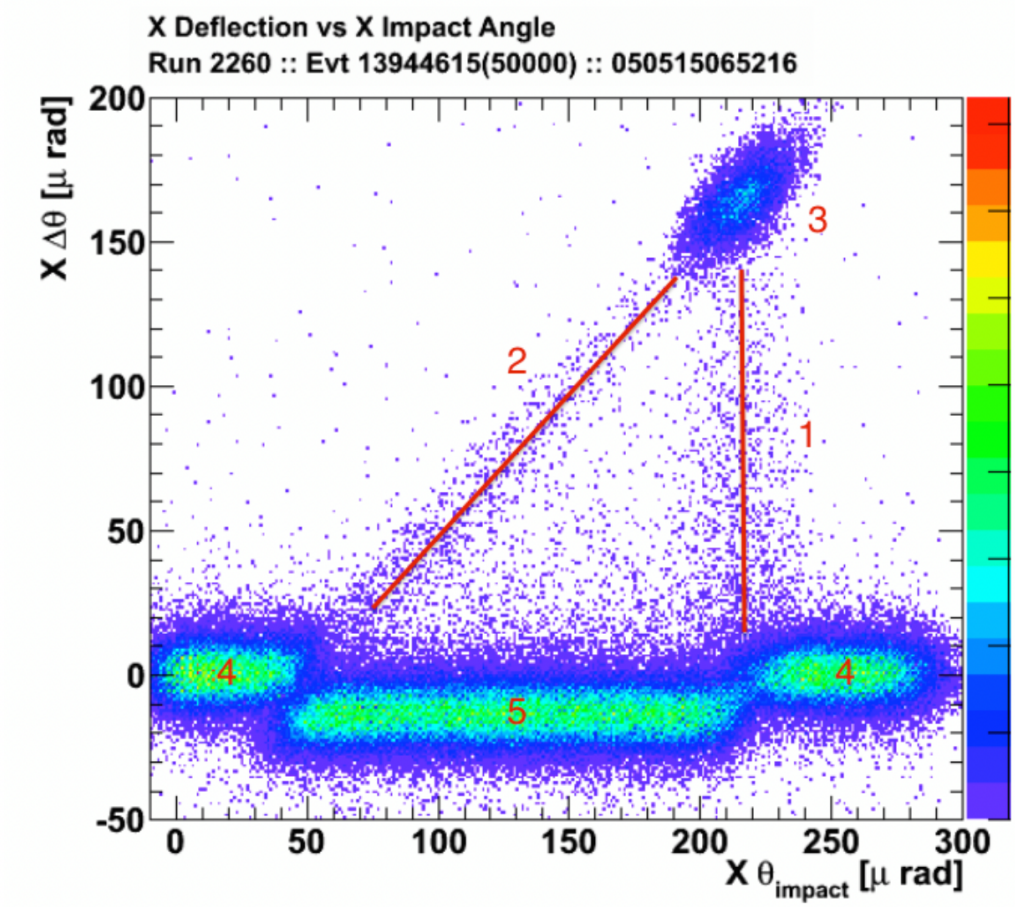

Figure 19: Angular scan for a strip-foil crystal STF101 analysed in the year 2015. The plot shows the angular horisontal deflection $\Delta\theta$ in micro radians as a function of the horisontal impact angle θ_{impact} in micro radians. The regions marked by numbers refer to the crystal interactions in the following way 1: Dechanneling, 2: Volume capture, 3: Channeling, 4: Amorphous scattering, 5: Volume reflection [30].

Now that we have found the channeling regime from the angular scan, we can perform measurements on the channeled beam using a linear scan.

4.3.3 Linear Scan

A linear scan is performed by intercepting both the secondary channeled beam and the primary beam with a collimator, thus examining the beam profile and kick angle from the crystal to the protons. The collimator jaws start from a retracted position and will move inwards so that it will intercept first the channeled particles, then the dechanneled and then coinciding with the volume captured and the volume reflected particles the primary beam will be intercepted. As you move the LHC collimator inwards and it intercepts more of the beam the beam loss increases, first slowly only reaching the channeled beam where it grows like a Gaussian, then it increases linearly in the dechanneled regime, and finally exponentially as the primary beam is intercepted. Integrating the beam profile over this whole inwards movement of the collimator jaw gives the total beam loss.

4.3.4 Normalization and data

Each run is going to be slightly different because between each run the parameters change slightly, like for example the beam intensity and position, so we have to normalize the data before we can compare runs of for example angular scans.

The BCT is used to score the beam intensity around the accelerator. The plot of the intensity profile is then fitted linearly to find the number of particles lost. This is then used as the normalization of the flux.

4.3.5 Slow Extraction

When beam is extracted to another accelerator it needs to be controlled. This can be done via a crystal deflecting the channeled beam, so that the beam takes multiple turns in the machine at other orbits (orbit bump). Then after two turns, the beam is in the external side of the machine and can be deflected towards an extraction line and injected into the LHC or into the H8 extraction line where the crystal characterisation is performed.

5 Crystal characterisation

In this chapter we will describe the results with the experimental data taken at the H8 extraction line, using the setup shown in the previous section and the analysis framework introduced here.

The goal is to get a full characterisation of the crystals by characterising the torsion, the mean deflection angle, and the channeling efficiency of the crystals. The crystals STF113 and ACP82 have been inspected during these radiation campaigns.

5.1 Deflection angle

We start off by showing the horisontal deflection angle plotted versus the horisontal and vertical impact position in mm for the two crystals.

For the analysis of the trajectories of the particles interacting with the crystal seven parameters are used: horisontal and vertical impact positions $d0_x, d0_y$, horisontal and vertical incoming and outgoing angles $\theta_{x,in}, \theta_{y,in}, \theta_{x,out}, \theta_{y,out}$ and the goniometer horisontal angle gpx. The deflection angle is found as $\Delta\theta_x = \theta_{x,out} - \theta_{x,in}$ and $\Delta\theta_y = \theta_{y,out} - \theta_{y,in}$

When comparing the two crystals the mean deflection angle is smaller for the STF113 crystal than for the ACP82 from a qualitative perspective. This can be seen when considering the figures 21 and 23 below where for the ACP82 crystal the region with higher deflection angle corresponding to the channeling region is clearly a distinct region for itself, while for the STF113 crystal the distribution of channeled particles overlap with the distribution of amorphously scattered particles.

When considering the plot showing the deflection angle as a function of horisontal impact position, the distribution of channeled particles has a center around a constant value for the deflection angle. Thus, we see a uniform mean deflection angle when varying the horisontal impact position of the particles on the plot below.

Instead, when considering the horisontal deflection angle as a function of the vertical impact position we see that there is a slight linear tilt in the mean of the distribution of channeled particles. This means that the mean horisontal deflection angle of the crystal varies with vertical impact position and this is a quality that we have to account for in the crystal when doing a full characterisation.

5.2 Torsion

The first quality of the crystal that is quantified is the torsion of the crystal due to the twist in the vertical planes, which creates the tilt seen in the channeling regime of the plot depicting horisontal deflection angle versus vertical impact position.

Two methods for determining the torsion are considered. The first involves the mean angular deflection of channelled particles as a function of the vertical impact position. In a crystal without torsion all heights are equivalent and the mean angular deflection is independent of the height of the crystal, just like we see no correlation

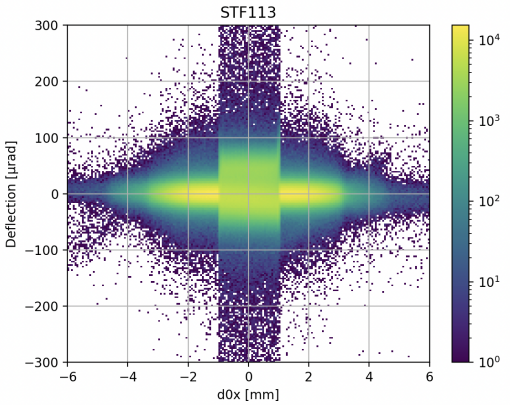

Figure 20: The horisontal deflection angle in μrad as a function of the horisontal impact position $d0_x$ in mm for the strip-foil crystal STF113. The width of the crystal can be extracted by looking at the horisontal width of the column-like structure centered around 0 with higher deflection angles. The colour bar corresponds to the particle density.

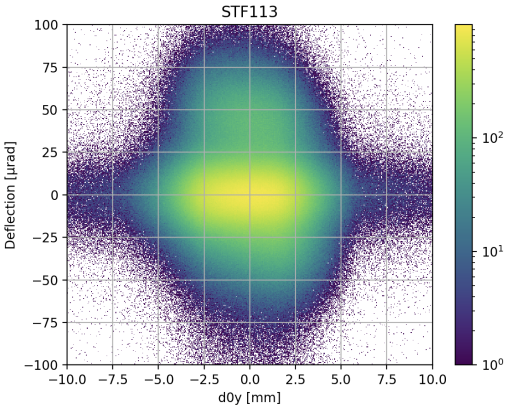

Figure 21: The horisontal deflection angle in μrad as a function of the vertical impact position $d0_y$ in mm for the crystal STF113. A slight tilt can be seen in the axis of symmetry in the region corresponding to the channeling regime. The colour bar corresponds to the particle density

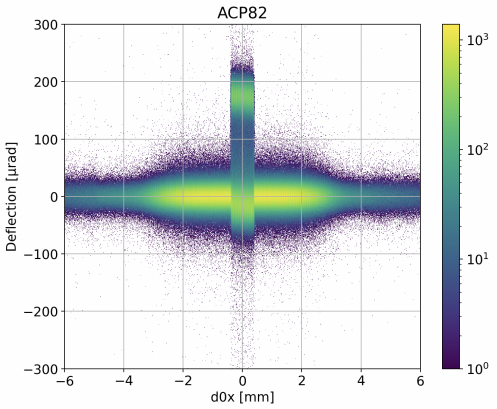

Figure 22: The horisontal deflection angle $\Delta\theta_x$ in μrad as a function of the horisontal impact position $d0_x$ in mm for the crystal ACP82. The width of the crystal can be extracted by looking at the horisontal width of the column-like structure centered around 0 with higher deflection angles. The colour bar corresponds to the particle density.

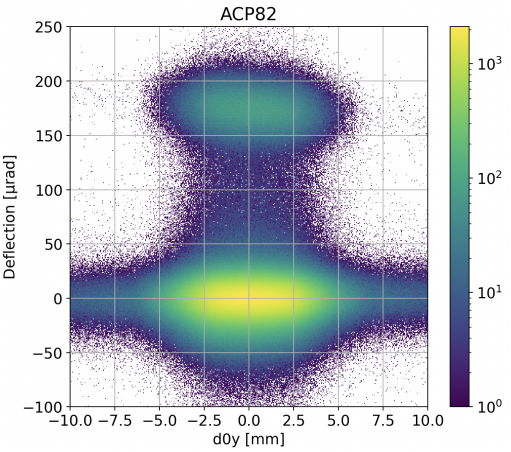

Figure 23: The horisontal deflection angle $\Delta\theta_x$ in μrad as a function of the vertical impact position $d0_y$ in mm for the crystal ACP82. A slight tilt can be seen in the axis of symmetry in the region corresponding to the channeling regime. The colour bar corresponds to the particle density.

between the horisontal deflection angle and the horisontal impact position in figures 24 and 25. However, if torsion is present the mean angular deflection will depend on the vertical position as seen in the figures 21 and 23, and thus we would need to

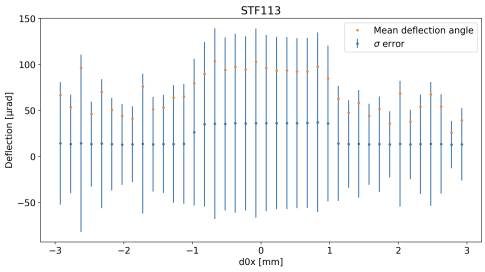

Figure 24: The figure shows the horisontal deflection angle $\Delta\theta_x$ in μrad as a function of the horisontal impact position $d0_x$ in mm for the crystal STF113 but this time plotting the mean of the deflection angle for each bin in orange, and the corresponding errors of the distribution in blue. From here it can be seen that there is no apparent relation between the horisontal deflection angle and the horisontal impact position when within the width of the crystal

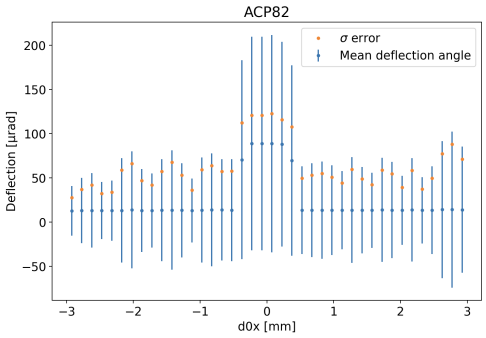

Figure 25: The figure again shows the horisontal deflection angle $\Delta\theta_x$ in μrad as a function of the horisontal impact position $d0_x$ in mm for the crystal ACP82 but this time plotting the mean of the deflection angle for each bin in orange, and the corresponding errors of the distribution in blue. From here it can be seen that there is no apparent relation between the horisontal deflection angle and the horisontal impact position when within the width of the crystal

find a torsion corrected average.

We want to create a plot similar to that of the figures 24 and 25 except plotting versus vertical impact position. We call this the mean angle method of finding the torsion.

If the beam is parallel with the normal vector of the crystal surface $\delta\theta = 0$ the beam profile of the incoming beam is approximately Gaussian with a spread σ_{in} for either the x or y direction.

The efficiency is a feature of the crystal and is also normally distributed with $\eta(\theta)$ and corresponding width σ_η. The amount of channeled particles is then given by

$$N_{ch}(\theta) = N_{in}(\theta_{in})\eta(\theta) \tag{24}$$

where $N_{in}(\theta_{in})$ is the number of incoming particles with incoming angle θ_{in} in either the horisontal or vertical direction and $\eta(\theta)$ is the distribution of channeling efficiency as a function of incoming angle of the particles. Thus, the number of channeled particles is simply given as the amount of incoming particles times the probability distribution of being channeled.

We said that there is a proportionality factor between the mean horisontal deflection angle of the channeled particles $< \Delta\theta_x >$ and the vertical impact position $d0_y$. In other words the mean horisontal deflection angle of the crystal is proportional to the vertical impact position $d0_y$ with a proportionality constant referred to as the

torsion t.

$$< \Delta\theta_x >= t \cdot d0_y \tag{25}$$

This provides us with a way of calculating the torsion in the crystal planes for infinitesimal steps in the vertical simply as

$$t = \frac{< \Delta\theta_x >}{dy} \tag{26}$$

where $\frac{<\Delta\theta_x>}{dy}$ is the rate of change of the mean horisontal angular deflection with the vertical position on the crystal.

The other method is referred to as the efficiency method, where the height is varied through a vertical scan of the crystal while keeping the incoming angle at 0 with respect to the crystal face normal. If there is no torsion the efficiency is the same for all heights. By varying the vertical height and making a histogram of efficiency for each height, it can be seen that if there is a variation there is torsion present as a function of vertical height.

But the mean angle method is the preferred method used for both crystals and the results are presented below.

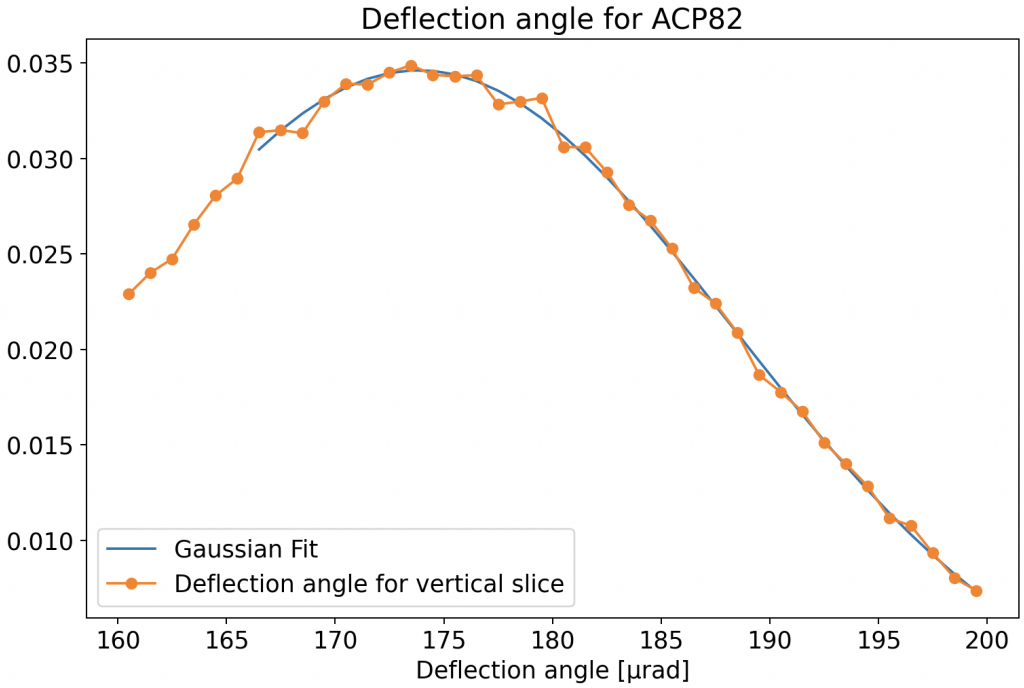

Figure 26: We fit a Gaussian to the distribution of horisontal deflection angles to determine the mean deflection angle as the mean of the distribution for the crystal ACP82.

We proceed by plotting the histogram of deflection angles for 41 bins for one vertical impact position and fit a Gaussian distribution to this histogram from which the mean from the fit corresponds to the mean horisontal deflection angle for that specific vertical impact position as seen on the figure 26. This mean horisontal

deflection angle is then stored in an array. This is repeated throughout the crystal in a vertical scan and appending the values to the array. A selection criteria is set so that the particles are in the range of [-0.5, 0.5] mm in the horisontal impact. The vertical scan is in the range [-4,4] mm in steps of the bin size of 30 bins. By

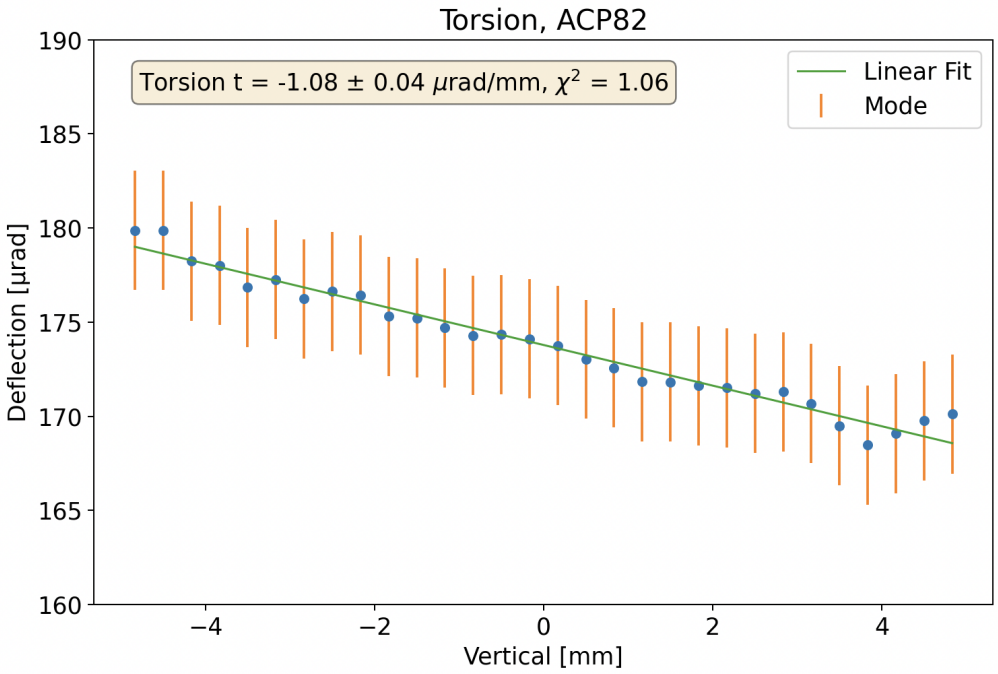

Figure 27: Each point on the line corresponds to the mean value of the Gaussian that has been fitted to the deflection angle distribution. We then did a linear fit through these point to get an estimate for the torsion with accompanying chi-square score.

completing the scan we get an array of 30 data points of mean deflection angles throughout the vertical which are seen plotted in the torsion figure 27. Here we see a linear relation in the mean deflection angle and vertical impact position. We fit a straight line through the data points and extract the value of the slope as a fit parameter which serves as the quantity for the torsion in the crystal. For the crystal ACP82 we get a value for the torsion of $t = (-1.08 \pm 0.04)\mu\text{rad/mm}$ with a χ^2 value of 1.06. The errors are estimated as the square root of the variance of the array values.

Usually you would take the mean of the distribution by using the Python package SciPy which has its own function for determining the mean of the distribution scipy.stats.mean(). The mean of the distribution then coincides with the peak in the histogram. This was used for the production of the figures 24 and 25, and initially also used for the crystal ACP82. We then switched to the manual mean estimation via the Gaussian fit of the binned histogram instead after having characterised the STF113 crystal

The STF113 crystal proves more difficult to analyse due to its smaller deflection angle. The Gaussian distribution of the amorphous peak overlaps with the Gaussian

distribution of the channeling regime. This results in a less ambiguous cut between the amorphous and channeling regime.

This also meant that for the determination of the torsion in the STF113 crystal another method had to be applied. We determine the torsion by looking at how the channeling peak shifts when scanning the vertical slices of the crystal like for the crystal ACP82.

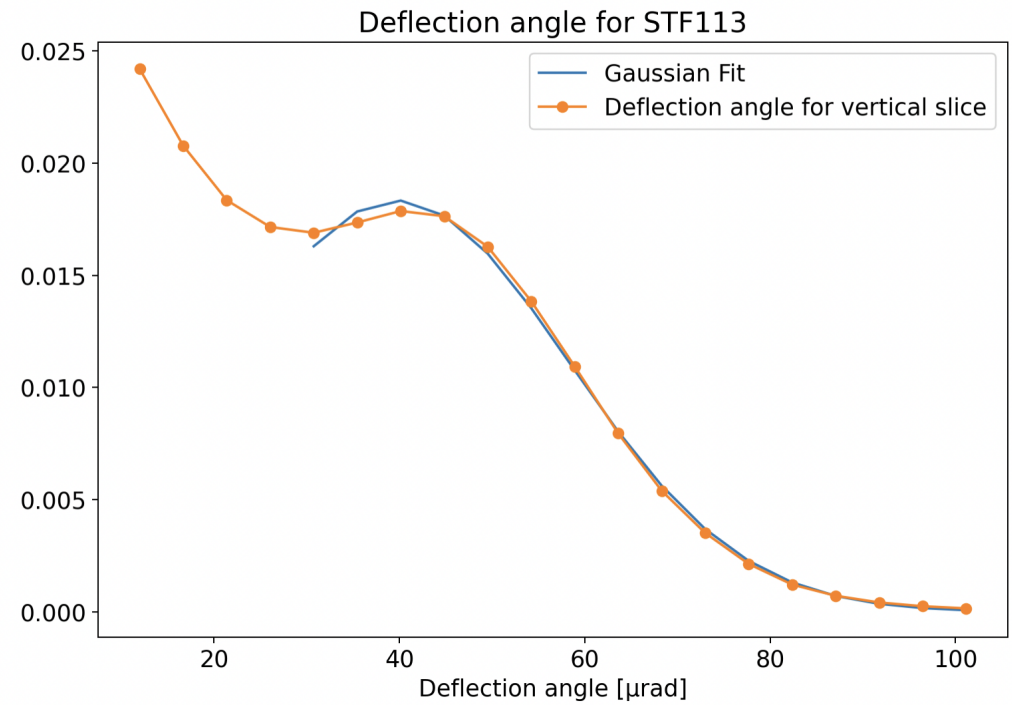

Figure 28: We fit a Gaussian to the distribution of deflection angles but use the value for the mode of the local peak of the two overlapping distributions. Taking just the mean of the distribution results in a skewed mean due to the overlap between the channeling and amorphous distribution.

But due to low deflection angle of the crystal STF113 the amorphous and channeling distributions overlap and thus the value for the mean of the channeling peak is shifted to the left towards the amorphous region. This is corrected for by instead using a Gaussian fit to the channeling peak, manually deciding where the channeling regime starts and finding the mode of the distribution instead of the taking the mean. An array is then created of the deflection angles corresponding to the mode for each vertical slice and a linear fit through these points gives us an estimate of the torsion for the crystal similar to when analysing the ACP82. For the strip-foil crystal STF113 we find a torsion of $t = (-1.82 \pm 0.17)\mu$rad/mm with a χ^2 value of 1.10. The errors are estimated as the square root of the variance of the array values.

The torsion for the STF113 was found to be (-0.56 $\pm$ 0.05) μrad/mm initially using scipy stats, which did not correlate with prior analysis. As explained above simply taking the mean makes us underestimate the mean deflection angle data points that are used in the torsion fit. This is why we had to adopt the other

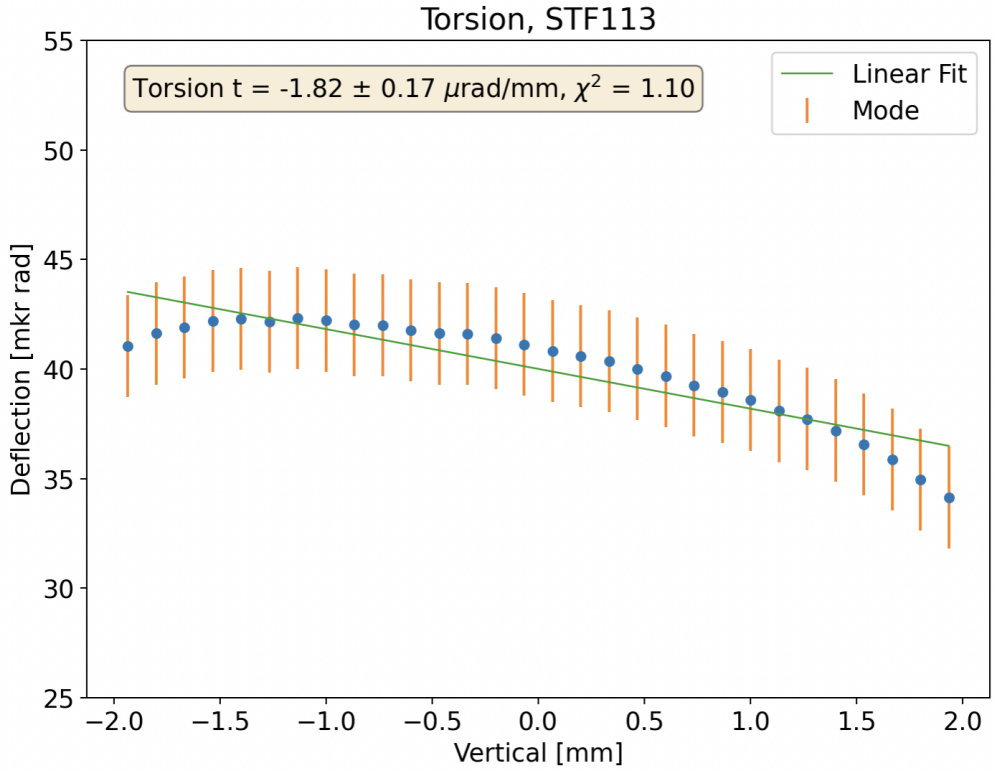

Figure 29: Each point on the line corresponds to the mean value of the Gaussian that has been fitted to the deflection angle distribution. We then did a linear fit through these point to get an estimate for the torsion with accompanying chi-square score.

method by calculating the mode. For ACP82 the torsion was found to be (-1.08 ± 0.04) μrad/mm regardless of the method used due to its larger deflection angle and thus less overlap between the distributions.

5.3 Full characterisation

Having characterised the torsion, the data is then corrected for this effect by correcting the incoming impact angles with a constant factor corresponding to the torsion times the center value of the vertical plane where the center of the beam is impacting.

A 2D plot is made of the horisontal deflection angle as a function of the torsion corrected horisontal impact angle, with the channeling region centered around an impact angle of 0. From this plot, four distinct regions can be seen: the channeling region, dechanneling region, volume reflection region and the amorphous scattering region.

On the figures 30 and 31 the two crystals have been plotted with their horisontal deflection angle in μrad as a function of the torsion corrected horisontal impact angle in μrad. The colour bar corresponds to the particle density. As for the strip-foil crystal STF101 studied in 2015 and seen on the figure , distinct regions of particles

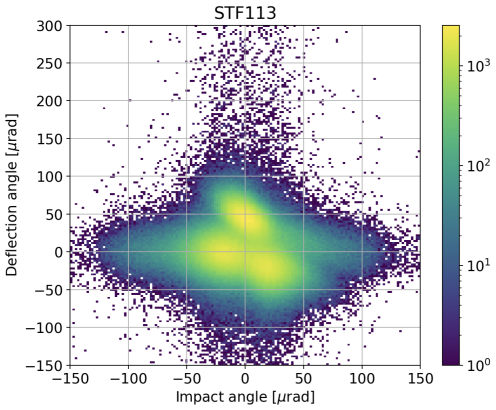

Figure 30: Scatter plot of the horisontal deflection angle in μrad versus the horisontal impact angle in μrad for the STF113 crystal. The Data has been corrected for torsion, so that the channeling distribution is centered around 0. The colour bar corresponds to the particle density.

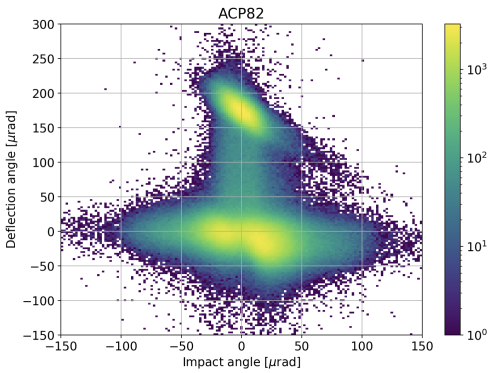

Figure 31: Scatter plot of the horisontal deflection angle in μrad versus the horisontal impact angle in μrad for the ACP82 crystal. The Data has been corrected for torsion, so that the channeling distribution is centered around 0. The colour bar corresponds to the particle density.

are formed, where the uppermost region corresponding to the largest horisontal deflection angle is the population of channeled particles. The column structure vertically connecting the channeling region with the lower population corresponds to the dechanneling region, the bottom left to the amorphous scattering, and the bottom right distribution is the volume reflected particles.

This corrected distribution is what we then use to finish the characterisation. A histogram of the torsion corrected deflection angle in μrad is performed and three fits are done as seen in the figures 32 and 33. One for the amorphous region, the dechanneling region, and the channeling region. The fit parameters from this action gives us the mean amorphous scattering angle, and the mean horisontal deflection angle.

The last quantity we need to characterise is the channeling efficiency which can also be computed from the corrected plot of the deflection angle. Channeling efficiency is defined as the ratio between the population of channeled particles versus the total number of particles with an incoming angle lower than the critical angle that hit the crystal face in each of the $60 \times 60 \mu m^2$ squares in which the total surface is divided into based on the bins.

For the crystal ACP82 we find a mean deflection angle of $\mu = (174.02 \pm 0.11)\mu$rad with a width of $\sigma = (12.50 \pm 0.11)\mu$rad a channeling efficiency of $\eta = (49.98 \pm 0.28)\%$, and a chi-square value of $\chi^2 = 1.81$ for the Gaussian fit. The parameters found for the characterisation of ACP82 is in accordance with prior analysis done on the crystal [15].

For the crystal STF113 we find a mean deflection angle of $\mu = (44.36 \pm 0.08)\mu$rad with a width of $\sigma = (14.47 \pm 0.09)\mu$rad a channeling efficiency of $\eta = (62.76 \pm 0.24)\%$,

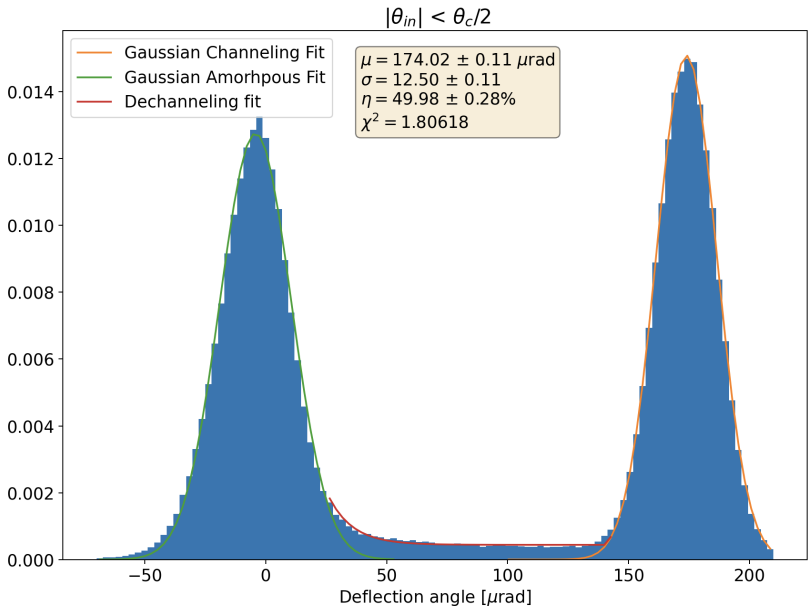

Figure 32: Normalised histogram of the torsion corrected deflection angle in μrad for the crystal ACP82 for half critical angle. Three fits are made, one for the channeling region indicated by the orange line, one for the amorphous peak indicated by the green line, and one for the dechanneling region indicated by the red line. The mean deflection angle found for the crystal is $\mu = (174.02 \pm 0.11)\mu$rad.

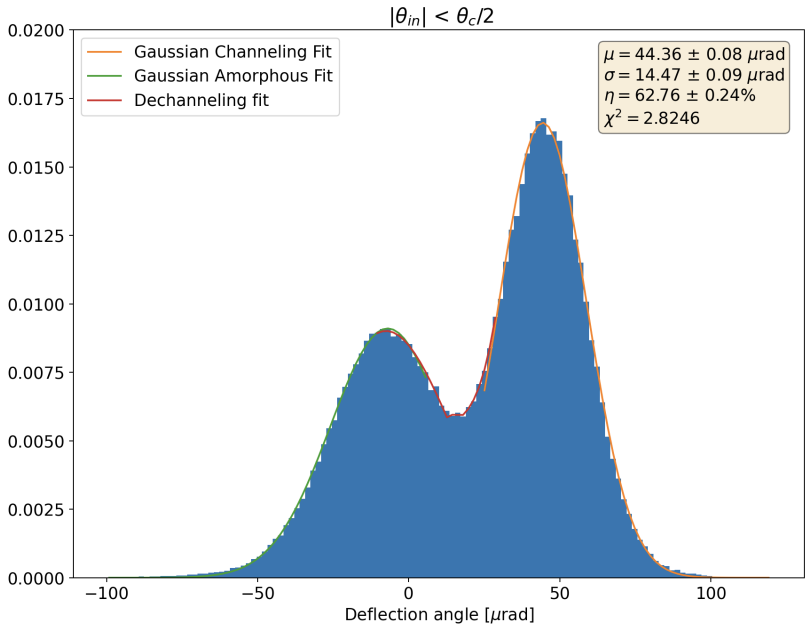

Figure 33: Normalised histogram of the torsion corrected deflection angle in μrad for the crystal STF113 for half critical angle. Three fits are made, one for the channeling region indicated by the orange line, one for the amorphous peak indicated by the green line, and one for the dechanneling region indicated by the red line. The mean deflection angle found for the crystal is $\mu = (44.36 \pm 0.08)\mu$rad.

and a chi-square value of $\chi^2 = 2.82$ for the Gaussian fit.

6 Simulation framework

Moving on from using experimental results we go on to introduce the simulation framework needed for the continuation of this study. We have a goal of simulating the beam line that was used in a 2018 experiment for studies of crystal assisted collimation in the Long Straight Section 5 (LSS5) beam line of the SPS accelerator, where we wish to simulate the particle losses.

We also use the simulation to review both a simulation and experimental study done for a Silicon crystal with regards to crystal robustness concerning energy deposition and atomic displacements affecting the channeling efficiency in the crystal, which was described in the prior chapter.

The two principal tools used for the simulations of particles in materials are Fluka and Flair which are used for producing the results for the particle loss map analysis and crystal robustness study respectively.

The simulations are run in the Fluka Monte Carlo simulation package written in the Fortran programming language, which is a fully integrated package for the interaction and transport of particles and nuclei in matter.

Fluka has scripts dating back to the 1980's being written and modified continuously by the users at CERN. The scripts describe all the physics that can take place in an accelerator as well as defines the geometrical bodies of all components. Using the scripts we tailor a simulation to our specific needs for the study. More precisely we use it for when simulating and producing the results of the particle losses in a later chapter.

We also introduce the visual user interface of Fluka called Flair for running the simulations from a convenient user interface and defining the geometry on the go while also being able to see the bodies and create data plots all in one place. This is used for producing the simulation results on crystal robustness used in the next chapter, but is also used for visualisation of the beam line as well as placement of absorbers for the particle losses analysis.

6.1 Simulation using Fluka

Simulations are built by using the resources available in the CERN remote cluster Clueet. The cluster contains directories with templates of all the aperture, meaning pipeline segments for drift sections and bending sections, crystal bodies, collimators, beam loss monitors and various other bodies found in the SPS and LHC. You can also define your own geometries of objects to test in simulation or perform radiation studies on, or experimental designs for accelerators you want to study.

6.1.1 Line Builder

Line Builder[33] is a tool to make simulation of complex geometries easier in Fluka so that instead of having to define the whole geometry from scratch and in one

collected script, we use the Line Builder as a "master-script". All the predefined objects and geometries of accelerator segments can be plugged in as building blocks to design your very own simulated experiment. It functions as a master script that assembles the whole geometry of the simulation based on external files that is fed into an input file. The Line Builder script has many elements which collectively builds a complex geometry, and allows for many customised builds. You can simulate single beam line segments, whole accelerator complexes such as the LHC, SPS, or PS. You can also build your own custom experimental design and test how it would function under various operations. The possibilities are many and as such they are being tested abundantly by the different collaborations at CERN. Uses are not limited to traditional particle physics but also include testing novel designs for small scale accelerators used for medicinal purposes. In this study we use the Line Builder to build the SPS accelerator, by including the aperture we find appropriate. Instead of building the whole SPS accelerator (very computationally heavy with a circumference of 6.9 km and a simulation with a micron scale resolution), we study the region of interest in the accelerator where we are looking at the LSS5 segment of the SPS, since this is where the UA9 collaboration is centered and the radiation testing of absorber materials is taking place.

6.1.2 Simulation cards

The cluster also contains directories that define all the physics we wish to include in the simulation. In the directory is found a card that defines what physics to include in the simulation such as the magnetic field strengths and the electric fields. Here it is also defined which interactions to include. For example if we include weak-force interactions in the collisions or strong-force interactions. The scripts that include the physics are very detailed and is able to include effects such as quark-quark interactions and neutrino production from lepton decays, such as a Michel decay, where during a particle collision a negatively charged muon is produced, which decays into an electron, an electron-antineutrino, and a muon-neutrino. These effects are necessary when studying hadron collisions in the LHC like proton-proton collisions, but would be overkill for when looking on beam dump physics at LHC injection energies of 440 Gev. Thus for the sake of the runtime of the simulation we put certain thresholds on the possible interactions. This is done via the transport card file, which is responsible for setting energy threshold limits. In the case of particle collision in an absorber we can limit the amount of cooling processes that are involved in the energy deposition. This is relevant for when we consider the proton impacting on the absorber, since this defines what kind of particle shower can be produced. If we are only interested in primary particles and the production of secondaries, we do not require the simulation to account for higher order decays, since the off-momentum of these produced particles would be so high, that they would be lost in the aperture at roughly the same spot. By not including the higher order particles produced in a shower the particles travel only a negligible amount

further. The transport card also puts on a boolean threshold whether to simply allow delta rays or not. These are responsible for dissipating away energy from the impact point in the absorber via friction through the electrons in the material.

Another card is responsible for the optics of the machine that is calculated from the geometry via the placement and dimensions of dipoles and quadropoles together with the magnetic field strengths from the physics card. This determines how the trajectories of the charged particles behave which for an ensemble of particles result in the beam envelope that was described in the earlier chapter on accelerator dynamics.

A lot of physics is taking place in the simulation so another important role is selecting the trackers and what data one wants to score for the particles. For this we use the mgdraw file which determines what kind of data files to produce, how to name them, and what quantity to score. This could be to score position, energy, and momentum for particles, incoming and outgoing angles, particle generation, transverse coordinates etc. Also specifically for the stopped particles we want their stopping coordinate and we wish to score the amount of inelastic nuclear interactions in the beam line. But to track all parameters for all particles would be an immense overkill and make it unfeasible to run the simulation for any large scale experiment, so in certain regions we might be interested in some additional parameters exclusively for those regions. For example we could have that for the whole accelerator we wish only to score the spatial coordinates and the momentum of the particles, but for specific regions like inside the crystal we wish to have more details to what kind of interactions the particles undergo and their trajectories. For example inside the crystal we also wish to score which of the five types of crystal interactions the particles have undergone and for the specific regions of the crystal face and its exit we additionally score the incoming and outgoing angles of the particles. In certain regions we also score the generation of the particle to distinct whether the tracked particle is a primary proton, a secondary proton meaning a proton that has some off-momentum due to an elastic scattering, or a secondary or higher order particle produced in a inelastic nuclear interaction. To account for these regions we need to have clearly defined boundaries. This is accomplished by defining trigger planes at the beginning of certain regions. This is accounted for in the usrmed and usrini files. usrmed registers when a particles leaves the vacuum for some other region for example vacuum to TCSM. The file then records the particle's properties and stops tracking the particle. It is also in these files we choose the coordinates from which we start to track particles. We define regions around boundaries such as the outer edge of the walls enclosing the room the beam pipes are confounded as black hole regions. This means that particles that reach this area are terminated and no tracking takes place. This is necessary so that the simulation does not run indefinitely. So mgdraw is responsible for creating the data files that track the number of losses in particular regions and the position of the particles. The usrini in combination with the usrmed file is where we define what regions to include and

omit for tracking and how they differentiate from each other. Like for the crystal which has both an entry and exit that we distinguish from the crystal as a whole. It is also in the mgdraw that we track the evolution of the particle and how many turns it has taken in the accelerator, as well as translation operators. This is also where we defined boundary actions such as the termination of a particle reaching the end of the defined geometry.

We use these files to generate data files that make sure we know what happens to every single proton that is produced. We simulate $N = 10^6$ protons and need to account for every single one of them to have control of the simulation results. This was a tedious process of rewriting and debugging the code accounting for some particles being terminated due to energy thresholds and not being accounted for in the produced files. So for that single condition it had to be coded into the script that it should store that interaction in a separate file.

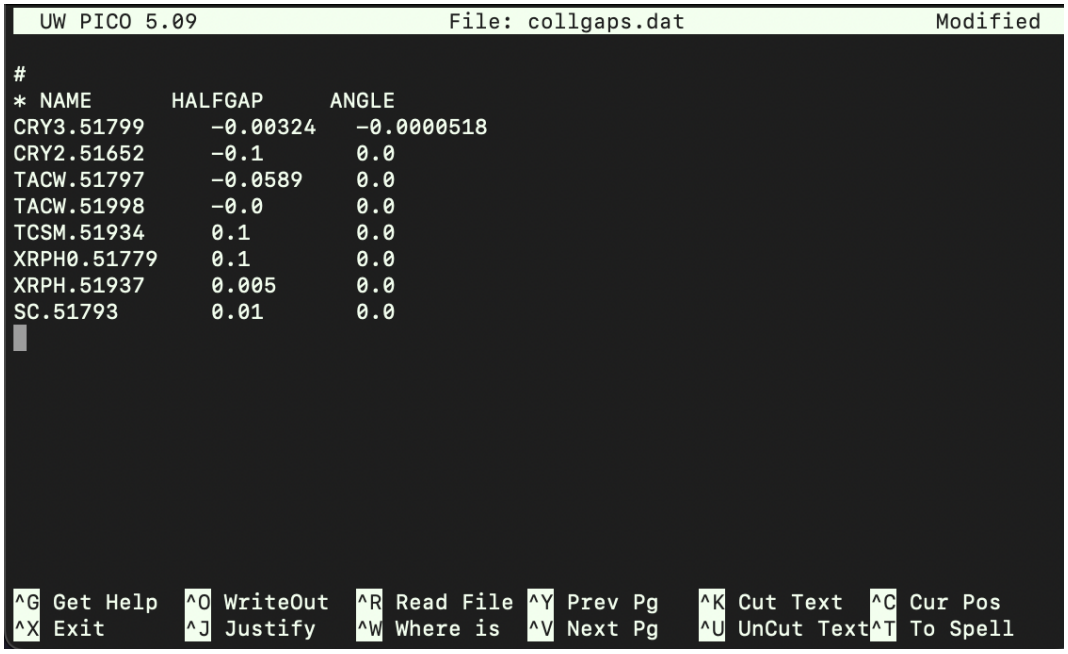

Figure 34: The collgaps file. In here the first column is the name of the object that is being called. The object's dimensions are specified in separate files for the bodies. The second column states how far the center of the object is placed from the beam line in units of meters. The third column is the angle in radians that the object should be rotated from its default orientation. The crystal in use CRY3 is rotated 51.8 μrad into channeling orientation. The other crystal CRY2 is outside the beam pipe, and is from a different experiment and so should not be considered in the context of this study.

The objects we include by defining them in the collgaps file are automatically placed in a specific region called the parking region in the simulation. This is an external region in the simulation geometry that is not affiliated with any physical space. From here the elements must be moved to their correct location and orientation. The ROT-DEFI cards are used to rotate elements and to move objects from the parking region to the proper place on the beam line.

A custom assignmat card is used to assign materials to the different regions, by importing a library of defined materials and their physical properties, such as mass density and electrochemical properties. One can also extend this library by adding their own materials as a combination of different elements such as a particular composite graphite.

The beam source card is used to define the coordinates of the source and its beam profile. We are simulating beam halo particles which are defined as the particles corresponding to 6σ or further from the beam core of the beam distribution and this is defined in this card.

Auxiliary files are also present for introducing off-beam objects. This is an arbitrary classification of objects not considered standard objects to be included in the beamline geometry. This is where the beam loss monitors are defined by their names and coordinates with respect to a reference element. These auxiliary files are also referenced in the inputfile. The auxiliary file in the figure 35 contains the eight beam loss monitors. The first column refers to the name of the beam loss monitor, which has its dimensions defined in a separate bodies file. The next column is the keyword that refers to which directory to look for the files describing the beam loss monitors. The next column is the longitudinal translation in meters either upstream or downstream of the reference object which is given in the last column. A negative value corresponds to upstream of the reference object and a positive value corresponds to downstream of the reference object. The reference objects are Roman pots, quadropoles and absorbers.

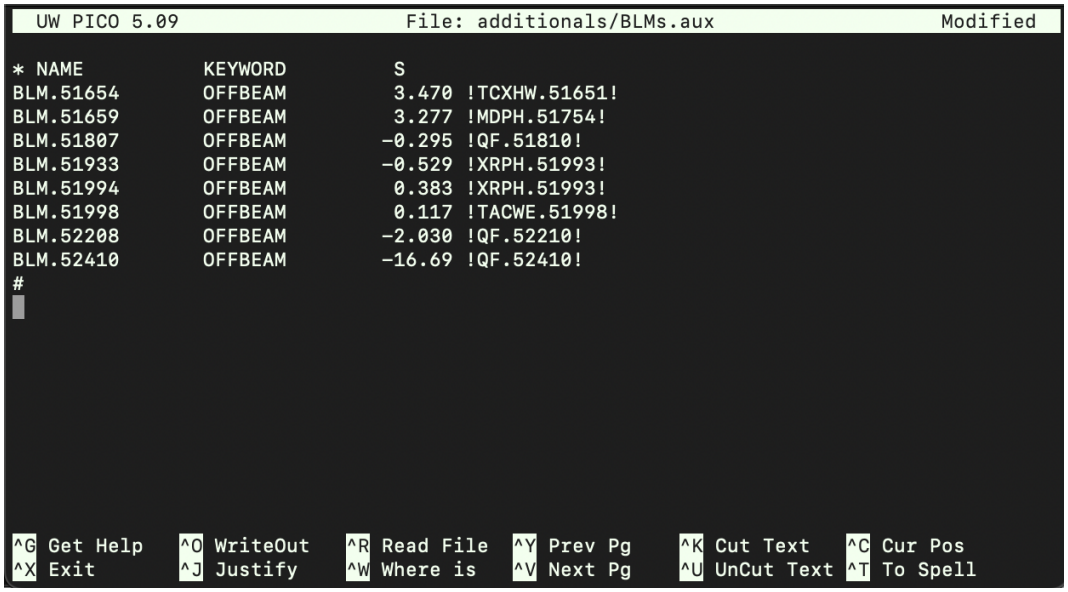

Figure 35: Eight beam loss monitors shown in the auxiliary file. They are being called via their referenced name in the bodies file. A longitudinal coordinate on the beam line is given either upstream or downstream of a reference element on the beam line.

Specifically for the ROT-DEFI card used for the beam loss monitors figure 36

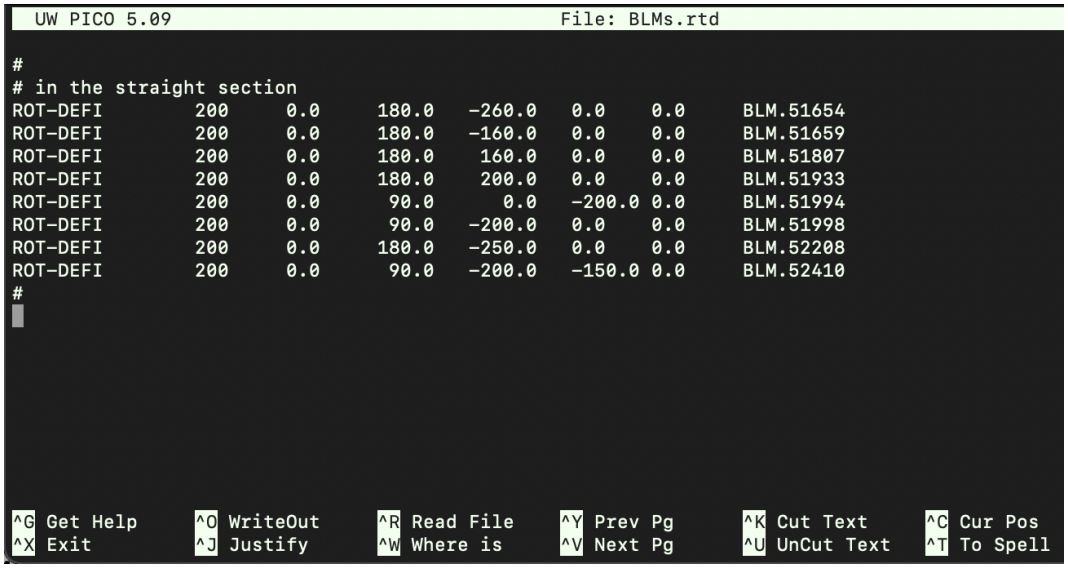

Figure 36: The ROT-DEFI card for the eight defined beam loss monitors. It holds the name of the specific beam loss monitor being called from the bodies file, the reference axis the rotation is centered about, the polar and azimuthal angle in degrees and translation in x, y, and z.

the card is taking care of the rotation of the eight defined beam loss monitors in their respective positions given by the auxiliary file. It allows for a rotation around the polar angle and the azimuthal angle. The first column calls the activation of the rotation operator. The second column is the tag for the rotation axis, where 200 corresponds to rotation around the y-axis as the reference vector. The next to columns are the polar and azimuthal angle respectively in units of degrees. The polar angle is 0 for all instances, meaning that all the beam loss monitors have their longitudinal axis in the x-z plane. Now for the beam loss monitors BLM.51994, BLM.51998, and BLM.52410, they have been rotated 90 degrees in the azimuthal direction meaning that their longitudinal axis is perpendicular to the beam line axis. For the other five beam loss monitors that are parallel with the beam line axis. The next three columns are the translations in the direction x, y and z respectively in units of mm. Naturally the beam loss monitors have to be moved in the transverse plane or else their centers would coincide with the beam line. Therefore they are placed either towards the inner wall or external wall of the beam line. Except for the beam loss monitor BLM.51994, which is perpendicular to the beam line and centered on the beam line's axis, and BLM.52410 which is also rotated perpendicularly but has its center placed 20 cm out from the beam line. Both beam loss monitors are shifted vertically down along the y-axis, so that they are beneath the beam pipe. BLM.51994 is shifted 20 cm down vertically and BLM.51994 is shifted 15 cm down vertically.

6.1.3 Building the line and running the simulation

Once you have all your settings defined in each external file you then go into the inputcard.txt file from where you choose which files to refer to the main script. The inputcard file serves as the mediator between the Fortran code and the Python scripts executing them together and linking together the appropriate external files. You combine the physics card, the defined objects, their translation and rotation cards and the scoring files. Furthermore in the input file you determine the basics of the simulation such as which particle to produce in the source and at what energy. You also choose from predefined keywords what kind of simulation you want to run. You can for example choose to do a simulation based on energy depositions in regions or one can choose to do a simulation with the focus of tracking particle trajectories. As a safety measure there is also Python parsing file in the directory named pythontest_assembly.py. This tests bodies and assemblies before building the geometry using Line Builder to check for overlapping regions. It is good measure to use this as a test of the geometry only, to spare yourself from compiling the whole simulation setup and find out there is an error.

Now the line can be built using the configure.sh script together with the inputcard txt file. Once the Line Builder Python script is executed it puts all the information from the external files that are fed into the inputfile txt file and produce an .inp file. An executable card is also compiled during the execution of the Line Builder script which carries the information of the physics settings. This .inp file together with the compiled executable contains all the geometry and the physics of the whole simulation, and is the canvas that can be used to start the simulation. The simulations can be run directly from the terminal window in the cluster by using the submit.sh script and defining the number of particles, the number of cycles the simulation should do, and on which of the servers the jobs should be submitted. This allows for running parallel jobs and combining them afterwards. When the script is run and the simulation has completed, Fortran data files are produced in new directories following the numbering of the specific run under a master directory which carries the name of the simulation that is given as an input in the inputfile. The Jupyter notebook file traj_test takes the produced Fortran data files and converts them to a h5 which can then easily be loaded directly into Python via the Pandas library to start analysis specific for the run in question.

6.2 Simulation using Flair

The .inp files described above can also be opened with the Flair interactive program which serves as a user interface that allows one to control most of the simulation parameters like the physics cards and allows one to define and visualize the geometry as it is built, as well as edit it from within the program. The simulation can be run from within Flair and plots can be produced from the resulting data files. Flair can be used as a user friendly way to edit the input files to be used in the Fluka

simulation. You edit the input in a .flair file which then generates the .inp file to be inputted to Fluka when submitting the simulation either to the CERN cluster or to your local machine.

6.2.1 Input and transport cards

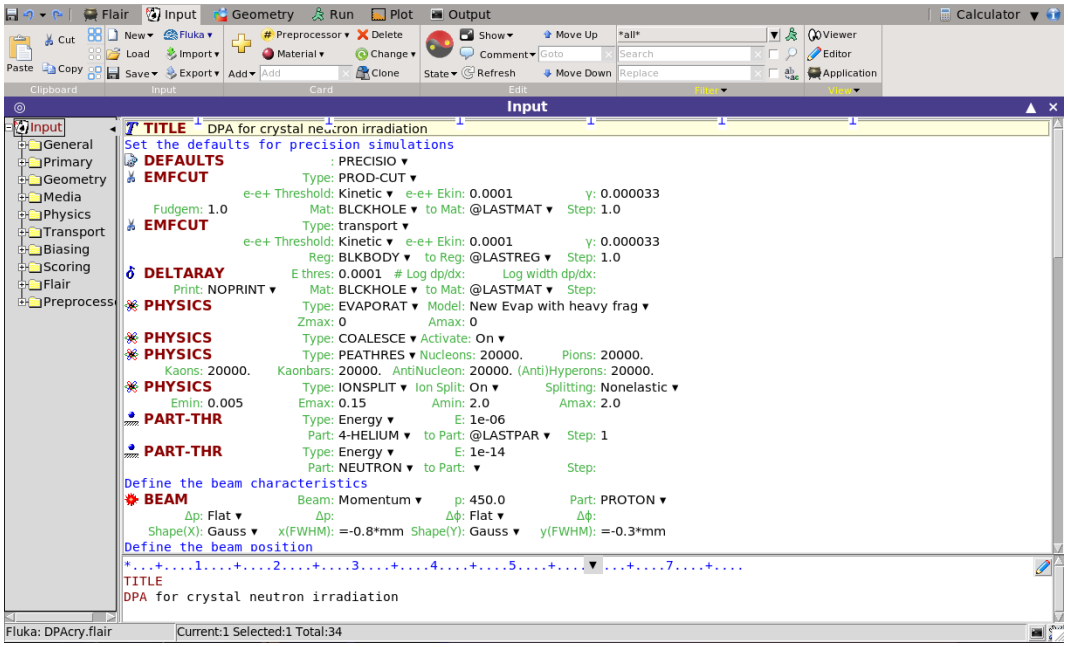

Figure 37: An example of a .inp file open in Flair. In the window we can see the different cards that can be defined for what physics to include in the simulation. The simulation can also be run directly from the Flair window in the Run tab.

In Monte Carlo simulations particles are tracked until they either leave the simulation geometry, or their energy drops below the transport energy threshold. Every DEFAULT has a transport and delta-ray threshold but this should be changed depending on the project simulation you wish to run by changing the EMFCUT and PART-THR cards. A rule of thumb is to set the transport threshold at an energy such that the range is smaller than the bin length. In the Input tab of Flair screen we can select the particle type, the particle energy, and beam width as well as the random seed. Some default settings for the physical parameters are present and used. We use the most detailed physics defaults by using the card PRECISIO. The EMF-cut is enabled by default and includes transport of e+/e- and photons. By enabling this the particle behaviour during collisions becomes more detailed as energy dissipation through the solid comes from multiple interactions. PHOTONUC actives photonucelar reactions. Because the mean free path between consecutive Coulomb scatterings (EMFP) and ionization losses (IMFP) is low it would be too computationally demanding to account for them individually in both high and low energy regimes. Therefore Fluka has an algorithm which only samples individually and includes generated delta rays when energy is large. Otherwise it will account for

the combined effect of the many small ionization losses under some energy threshold. This matters especially for electron-positron pair creation and for production of alpha particles. Delta rays are struck electrons which receive a lot of energy and can ionise other particles on their own, so they are significant when considering transport of energy away from the point of nuclear interactions happening in a solid like the absorber or crystal. Thus we set a delta-ray threshold depending on the specific scenario we are investigating, whether it is energy deposition or particle losses. So we enable two distinct energy levels: small energy below the energy threshold and large energy above the energy threshold, where the latter is being sampled explicitly, meaning that the tracking of energy transfer is more detailed for electrons being struck with a higher energy, dissipating this energy through the solid. There are numerous cards that can be added in the input tab to tailor the simulation to your experiment design. The electromagnetic cuts EMFCUT for electron, positron, and photon transport. The PART-THR and DELTARAY cards for transport of charged hadrons, muons, and ions. The EMFFIX card prints the stopping power for e-/e+ annihilation. If you want single scatterings the MULSOPT card can be enabled for a certain energy threshold, and for very small volumes μm^3 MULSOPT is necessary because the Moliere theory for the many low-energy scatterings does not apply.

6.2.2 Example of transport

An example of how to choose suitable energy thresholds for the transport of particles is to consider the case where we have to produce a continuous-slowing-down-approximation (CSDA) graph in water as seen in figure 38. This graph depicts the relation between the range of the particle in g/cm^2 as a function of its energy in MeV. When a charged particle moves through a material it will lose energy as it ionizes its surroundings until its energy is almost zero and it is stopped. The distance to this point is referred to as the range of the particle and is dependent on particle type, particle energy and the material. If you divide the range by the density of the material you get the distance travelled for the particle before it is stopped. In the case of water the density is approximately $\rho \sim 1$g/cm^3 and thus we would get a relation of cm travelled for a particle with an energy of specific MeV. From the National Institute of Standards and Technology we have a library PSTAR/ESTAR for the stopping power of protons and electrons in different materials from which one can produce CSDA graphs and Bragg curves[22][23]. We see from the figure for CSDA of a liquid water target that a 10 MeV electron would travel a distance of tens of centimeters before being stopped. A 1 MeV electron would travel distances corresponding to mm-scale, and for 10 KeV it is micro-meter scale. If we then have a bin-size of 50 μm in the simulation, the 1 MeV electrons could travel through several bins so stopping the tracking of them at the first bin due to an energy threshold of 1 MeV would be to kill them prematurely and we would get distorted energy deposition maps. But for scales of 10 KeV it would be a fine threshold because the electrons should not traverse more than 1 bin anyway due to the range profile of

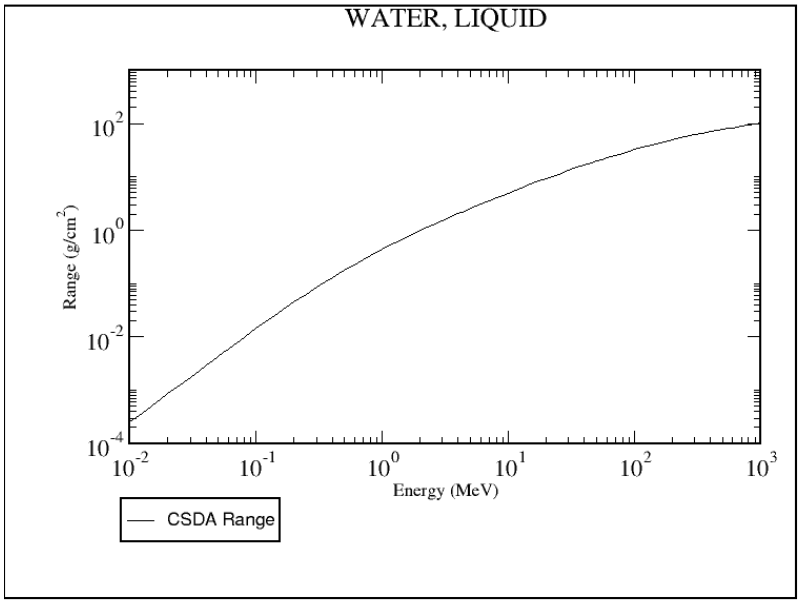

Figure 38: Continuous-slowing-down-approximation (CSDA) graph for water. The graph depicts the relation between the range of the particle in g/cm^2 as a function of its energy in MeV. [23].

water. So to sum up, the threshold depends on the grid size and geometry used in the simulation and the range tables of materials help set some sensible thresholds. Particles that travel farther should have a lower energy threshold and the threshold should be set as to catch the short-range particles in the first bins. The photon threshold should be lower, but for e-/e+ pairs the threshold should not be too low due to CPU usage of the simulation. The transport thresholds are outputted in the .out files in the produced simulation files after the run is executed. Related to the range of the particle is the stopping power of a material which is given as a 1D Bragg curve, showing the energy loss per length in a medium (MeV/cm). The Bragg curve also show a peak referred to as the Bragg peak, which is a pronounced peak on the Bragg curve which plots the energy loss of ionizing radiation during a particle's travel through matter. For protons, α-rays, and other ion rays, the peak occurs immediately before the particles come to rest. When a fast charged particle moves through matter, it ionizes atoms of the material and deposits a dose along its path. A peak occurs because the interaction cross section increases as the charged particle's energy decreases. Energy lost by charged particles is inversely proportional to the square of their velocity, which explains the peak occurring just before the particle comes to a complete stop. So the more the particle has already been slowed, the faster it will deposit its energy to its surroundings. Bragg peaks were produced as assignment exercises for getting to know the Fluka and Flair software, but are used much in radiation therapy or other radiation studies such as for examining the depth of the energy deposition of protons in the absorbers.

6.2.3 Geometry

The second tab in Flair is for visualization and editing of geometries interactively. You can open up prior simulations to visualise what the beam line of other experiments looked like and what physics settings it had defined. Every spatial dimension in the geometry is given in units of cm. The target objects that are predefined standard objects have three letter codes like for infinite planes we have XY-plane (XYP), XZ-plane (XZP), sphere (SPH), infinite cylindrical cylinder parallel to coordinate x/y/z (XCC), rectangular parallelopiped (RPP), ellipsoid (ELL) etc. In the geometry we differ between the definitions of a body, a zone, and a region. Bodies are geometrical structures placed somewhere in Euclidean space with spatial coordinates x, y, z. Zones are sub-regions described by subtraction or intersection of bodies. Regions are union of zones. So the area spanned by 1 or more zones, which themselves are defined by 1 or more bodies intersection. A lattice corresponds to a duplicate of the regions that combined make out a shape. These definitions can be seen on the figure below. Once you have defined your regions as a complete

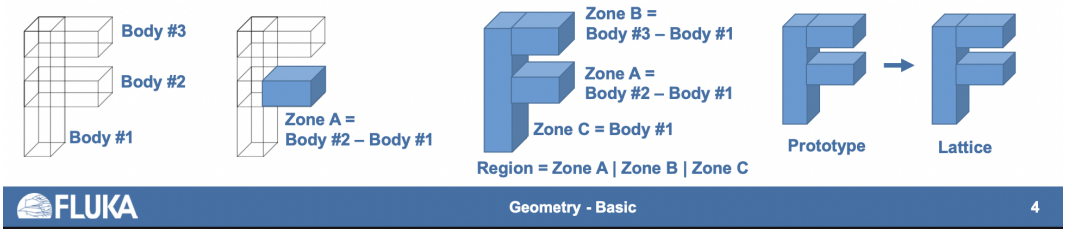

Figure 39: How geometry is defined in the Fluka and Flair syntax. We have definitions of bodies, which can be used to define zones, which finally act to define whole regions, which can be thought of as the prototype of an object.

prototype, some work is still needed before the simulation will run. All space must be defined for these prototypes placement to mean anything physically. Outside regions of prototypes must also be defined. Some operators that are used are "+" meaning inside the body, "-" meaning outside the body when defining zones. "|" is the divider between multiple region/zone definitions as to make union between zones to create a region. The most essential definitions are the BLACKHOLE regions and Air regions. The simulation is to be thought of as a grid where all points must have some definition. So if thought if like an onion structure the whole geometry needs to have an outer edge where the simulation is no longer valid. This is the BLACKHOLE region which is the edge of the simulation. Particles are killed and their tracking terminated when they reach this defined region or else the particles would be tracked indefinitely and as such the simulation would never reach a conclusion. Once inside the physical space where aperture is placed the whole geometry must also be filled by an "Air" region. This is like defining the field in which you can place objects. Else we will have undefined regions where a piece of machinery is filling a void. In this manner all points must be assigned to one and only one region with no overlap. You can also use the geometry tab to plot scored regions on top

like an electric field or magnetic force vectors for creation of physically informative plots of an accelerator complex.

6.2.4 Running the simulation

The third tab of the Flair interactive software is the Run tab, which is where the simulation can be managed and executed from. It can thought of as the "Command Center" of the simulation. Whatever parameters is fed into the run tab before starting the simulation will overwrite all prior defined parameters for the run that might have been put into the input tab. From this tab we choose how many cycles to run and with how many particles. We can stop currently running simulations, and we can clean the files from earlier simulations or merge together different runs.

The tab gives us an overview of the whole simulation, which inputfile is running as well as shows the progress bar of current cycles and parallel runs and the time remaining. The window lets you know whether the simulation was stopped prematurely or if it finished with errors and warnings etc. After running a simulation .inp and .out files are added to the ssh cluster's directory Clueet. Each cycle produces five files: .out .log .err, random seed file, scoring file. The amount of scoring files depend on how many scoring cards are defined in the Flair input tab. All generated files for each cycle must be merged once the simulation has finalised to create a composite data file to be analyzed. There is also an option to "Clean" the run files. This action will remove all files for a specific run while for the sub-tab "Data" within the tab Run, the "Clean" action will remove only the merged files, leaving the data from individual runs and cycles still there.

7 Crystal robustness

The simulation software Fluka and Flair was introduced in the prior chapter and these are the tools applied for creating the results of this chapter.

In this section we wish to apply the simulation software for testing the robustness of a Silicon crystal on the beam line during radiation. This is done by estimating the temperature increase in the crystal from the energy deposition of impacting particles. We do this by running a simulation with high statistics of a proton beam with a specified beam width. We plot the 1-dimensional maximal energy deposition as a projection on the longitudinal axis of the crystal, since we are not interested in the average deposition when testing robustness. The highest temperature is deposited very locally which is what causes melting or displacements of a local point in the crystal.

7.1 Prior studies of crystal robustness

In the 90's multiple studies on crystal collimation and crystal robustness had been performed. Many showed positive results that a crystal would not take significant damage during regular SPS operation. There was a firm basis that the halo beam particles intended for use in the SPS and LHC would not damage the crystals considered and temperature increases would be below 1 Kelvin.

The aim of this study is to develop a crystal assisted collimation system that can act as an upgrade to the current LHC collimation system installed described in the section 2.3. We can do this by testing the crystal in an SPS beam, as these results serve as a benchmark that can be generalized to an LHC beam.

The constraining factor for the use case of Silicon crystals in a collimation system is thermal damage resulting in melting of the crystal or phase transitions called brittle-to-ductile transitions.

Another factor is radiation damage that results in atomic displacements, but these only affect the efficiency of the crystal resulting in less channeling due to perturbations in the smooth potential between the atomic planes and thus on the capture of particles in the potential well.

So, for qualifying a crystal we need to also make sure it can withstand the energies in the accelerator. Specifically we want to see if the Silicon crystal can survive an accidental full-on impacting LHC beam.

The motivation for testing the crystal robustness is a case study performed as part of the stay at CERN relating a review of a simulation study performed in the year 2012. The study conducted by G. Smirnov et al [29][19] wanted to simulate the scenario of an accidental full-on impacting LHC beam on the crystal face of a Silicon crystal NA48 to see if the crystal would be damaged.

The study found that in the event of a full-on LHC beam impact, the maximum energy deposition in the crystal would result in a temperature increase above the melting point of Silicon at 1710 K, thus rendering the crystal unusable. As a result

of such damage during an accidental full-on impact event a new crystal would have to be installed.

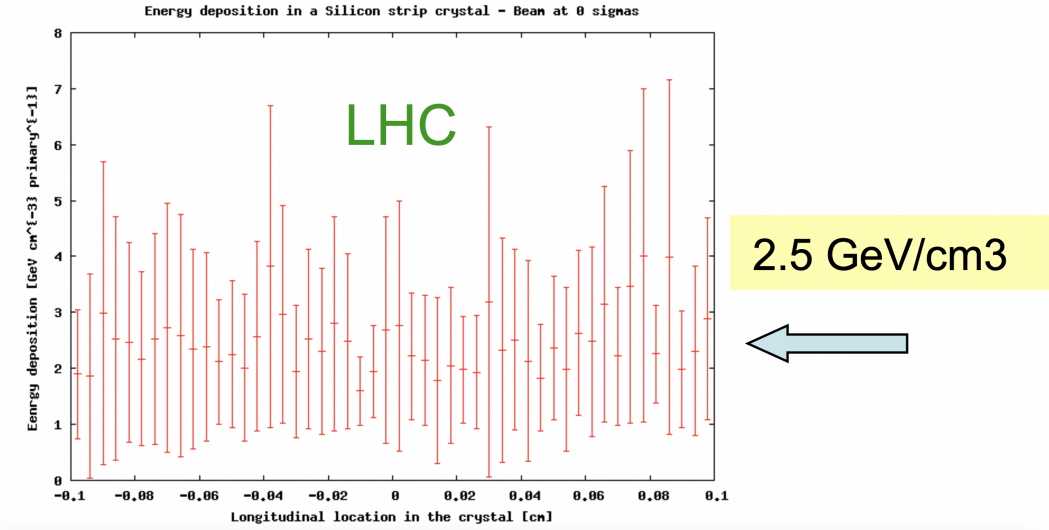

Figure 40: Plot from the 2012 study showing the energy deposition in GeV/cm^3 as a function of the z-coordinate in cm of the Silicon crystal. From here we can see that the error bars for the result have a magnitude of several GeV/cm^3. The maximum energy deposition cited from this result is 2.5 GeV/cm^3[29].

	Crystal size (mm3)	Beam size (mm)	Proton flux
LHC **7 TeV**	**1 x 50 x 2**	σ_X = 0.154 σ_Y = 0.412	3.63 •10^{18} (prot/s)
SPS **450 GeV**	**1 x 10 x 50**	FWHM$_X$ = 0.8 FWHM$_Y$ = 0.3	2.4 •10^{20} (prot/cm2)

Figure 41: The parameters used in the 2012 study to produce the result of the cited 2.5 GeV energy deposition.

The 2012 study simulated a crystal with the dimensions of 1 mm, 50 mm, and 2 mm for the x, y, and z dimension of the crystal respectively. They used a beam width of 0.154 mm and 0.412 mm for the horisontal and vertical beam width respectively and with a proton flux of 3.63×10^{18} protons/s.

They found an energy deposition of 2.5 GeV in the crystal resulting in a temperature increase of 1982 K, thus exceeding the melting point of Silicon.

7.2 Results of simulation

We use the parameters used in the 2012 simulation study and apply them to a beam with an energy of 7 TeV to produce the figure 40 showing the energy deposition in the Silicon crystal.

When translating energy deposition into a temperature we correct for the non-constant heat capacity of Silicon. The heat capacity varies as a function of temperature, and since we are dealing with temperatures on the scale of thousands of Kelvin we need to integrate over the varying heat capacity or we will overestimate the resulting temperature increase.

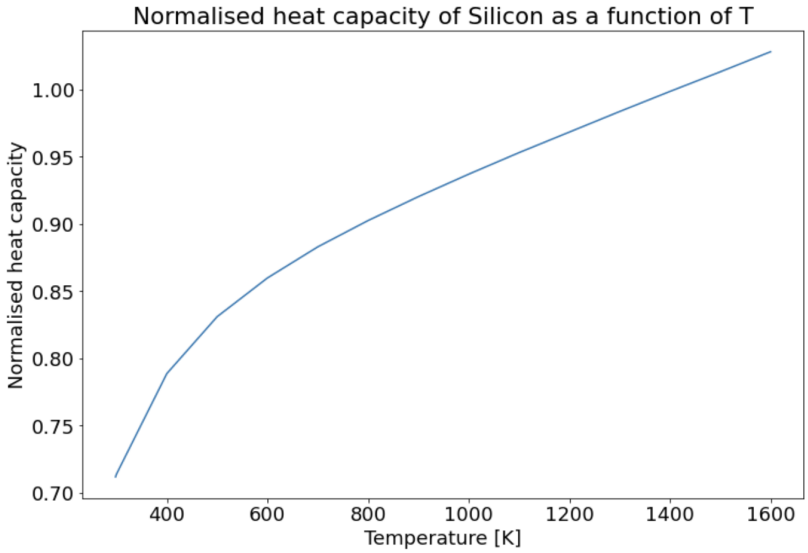

Figure 42: Data file provided by CERN with experimental measurements of heat capacity of Silicon as a function of the temperature in Kelvin. The plot has been normalised with respect to Silicons specific heat capacity.

In the year 2019 an experimental study was done with the use of a Silicon crystal in the HiRadMat department at the UA9 facility to test the claims of the 2012 simulation study[28].

The parameters provided by the HiRadMat group showed a beam with 216 bunches with a bunch intensity of 1.1×10^{11} particles per bunch.

In the study they irradiated both a strip-foil Silicon crystal and a quasi-mosaic crystal with a full on SPS beam of 440 GeV and saw no significant damage of the crystal or reduction in the channeling efficiency.

This is in contrast to what was predicted by the 2012 simulation study where the energies considered would result in temperature increases above the melting point of Silicon.

Thus there is a discrepancy between simulation results from 2012 and the experimental results from 2019. An investigation was set in to find out why. The input card from the 2012 simulation was found and copied to recreate the simulations.

We were able to replicate the results for a case of low statistics using the HiRad-

Mat parameters. We saw indications that the statistics had not converged. This resulted in an outlier of 2.5 GeV/cm^3/primary to lie within the center slice of the 2D projection of the energy deposition and can be seen on the figure 44. For the high statistics case we got a result of about 0.9 GeV/cm^3/primary which translated into a temperature increase resulted in a temperature increase below that of Silicon.

#shot	**1**	**2**	**3**	**4**
Date	23-05-2017			05-09-2017
Time	22:49	23:05	23:13	13:50
Optics	FP2_0.25mm	FP2_0.25mm	FP2_0.25mm	FP2_0.3mm
ppp	2.39e13	2.38e13	2.40e13	3.17e13
BTV.NEW Sigma_x,y [mm]	0.32, 0.35	0.4, 0.45	0.35, 0.45	0.43, 0.44
p/bunch (Velotti)	1.1e11	1.1e11	1.1e11	1.2e11
Number of bunches	216	216	216	288
emittance (Velotti)	2.9/2.8 mm.mrad			2.5/2.7 mm.mrad

Figure 43: Parameters used in 2019 experimental study. The most conservative parameters have been used in our simulation so that we slightly over estimate the energy deposition in the crystal

The study was performed at 440 GeV, and since the crystals used are 4 mm thick and the difference in energy deposition is only about 10% between 440 GeV protons and 7 TeV protons.

The experimental study conducted also checked the channeling efficiency post irradiation and saw a negligent decrease in efficiency. Thus the conclusion of the experimental study is conflicting with the results of the 2012 simulation study.

Now our goal is to find out why this discrepancy with experiment and simulation occurred and we set out to examine the data files from the 2012 study and try to recreate the results.

We use the experimental parameters from Smirnov et al shown in the figure 41 and try to reproduce the simulation result. We want to mimic an accident scenario where instead of the protons from the beam halo it is the beam core that hits the crystal. We simulate a 440 GeV proton beam core hitting the crystal oriented in the amorphous direction so no channeling is taking place, thus increasing the energy deposition by more than if the crystal had been channeling some of the incoming protons. The study on energy deposition is done under the assumption of adiabatic heat transfer since the duration of the beam pulses are on scales of micro seconds.

The Silicon crystal dimensions from the presentation is stated as 1x50x2 mm^3 while in the data files used, the dimensions are 1x10x2 mm^3. Using the same input parameters as from the input card of the Fluka data file used for the 2012 simulation,

we run the simulation and score the energy deposition. We run the simulation by varying only the amount of primary protons simulated.

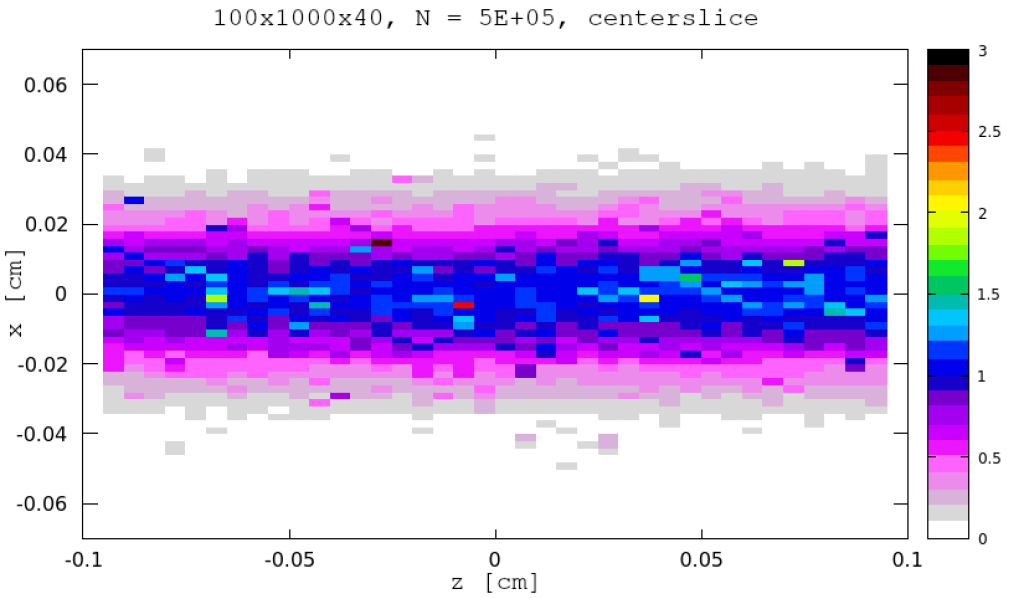

Figure 44: The 2-dimensional energy deposition in the x-z plane in the crystal produced from our replication of the 2012 simulation study by using the same parameters as for said study. Both axes are given in the units of cm. We simulated 5×10^5 protons just upstream of the crystal face. Here we can see an outlier marked in red corresponding to an energy deposition of about 2.5 GeV/cm^3.

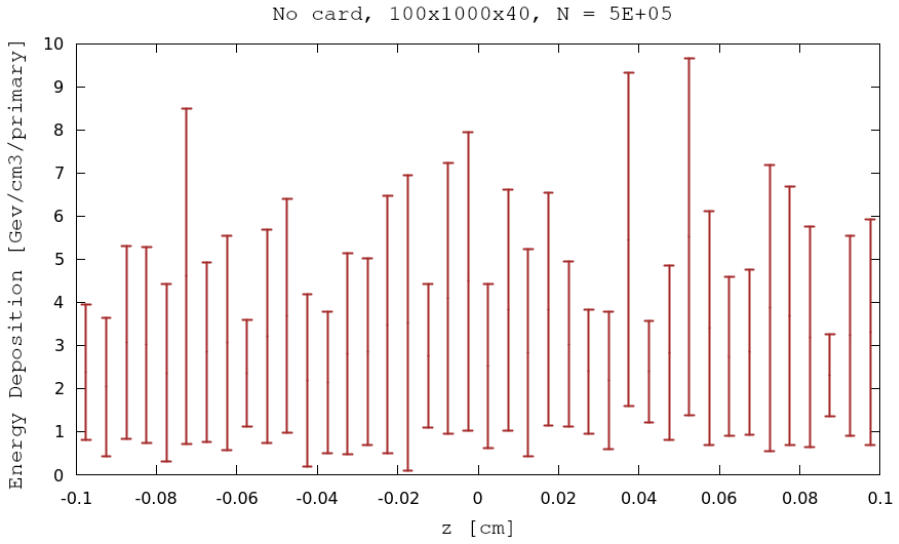

Figure 45: The 1-dimensional energy deposition in GeV/cm^3 as a function of the z-coordinate in cm in the Silicon crystal. By using the same parameters as in the 2012 study and simulating 5×10^5 protons, we manage to produce a result with error bars similar to that of the figure 40.

We managed to reproduce the 2.5 GeV energy deposition plot used in the 2012 study presentation by using the default values from the user score card in Flair and using the same number of bins as well as a low sample of $N = 5 \times 10^5$ protons simulated. The same result was obtained when using the same user card as for the study when considering the energy thresholds on the transportation cards.

Changing the transport card and EMF card described in the prior chapter, by increasing the threshold dramatically only has little gain in energy deposition. These cards determine how many low energy interactions we allow like electron-electron scattering and heat transfer through other interactions like delta ray production. But since many of these effects have a very small cross section at these energies their contribution is negligible and thus the default values for the transportation and EMF cards are sufficient.

We proceed to do the same simulation but increasing the amount of primaries simulated to $N = 10^7$.

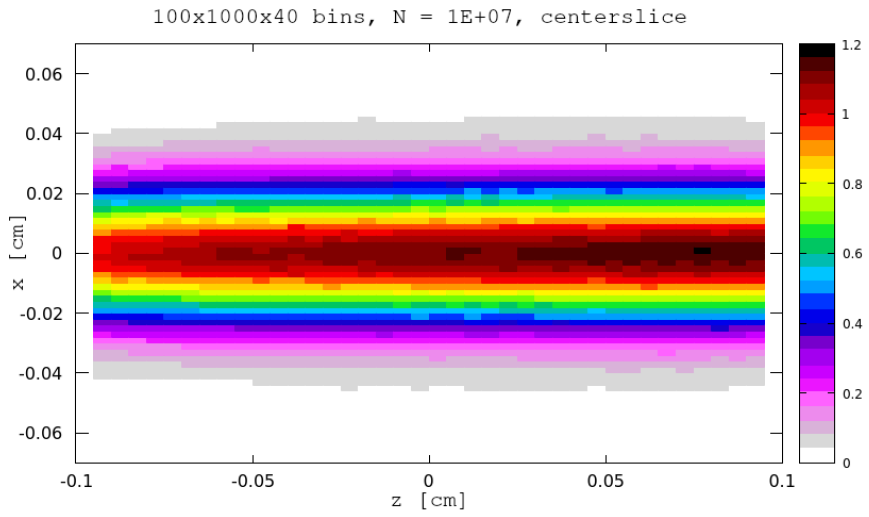

Figure 46: The 2-dimensional energy deposition in the x-z plane in the crystal produced from our replication of the 2012 simulation study by using the same parameters as for said study. Both axes are given in the units of cm. Here we simulated 10^7 protons just upstream of the crystal face. Unlike the other plot with fewer protons, here we see a smooth distribution in the energy deposition and see a maximum energy deposition of about 1.15 GeV/cm^3.

We have reproduced the low- and high statistics plots of the 1D energy deposition from the 2012 study by copying their user cards and by using default values for the transport cards as seen in figures 45 and 47.

We have also included a 2D projection of the x-z plane for both high and low statistics in figures 44 and 46. We do this by projecting the 2D energy deposition onto the y-axis and focusing on the center slice closest to the beam core, where we expect the energy deposition to be largest. So instead of projecting and averaging

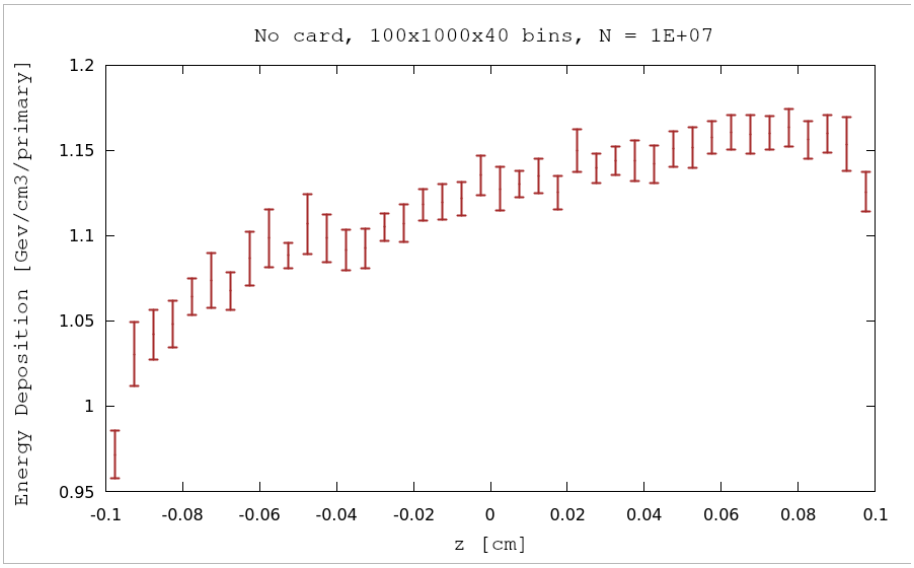

Figure 47: The one-dimensional energy deposition in GeV/cm^3 as a function of the z-coordinate in cm in the Silicon crystal. By using the same parameters as in the 2012 study and simulating 10^7 protons, we manage to produce a result where the statistics has converged and error bars are significantly smaller than for the simulation with fewer protons. From here we see a maximum energy deposition of about 1.15 GeV/cm^3.

over the whole y-range we only consider the slice right after y = 0.

We see that the 2.5 GeV reported is due to an outlier lying in the center slice. Most of the projection in the center is uniform except a few single pixels that have higher energy of about 2.5 GeV seen on figure 44. For the high statistics case the 2D projection looks completely uniform with a smooth gradient along x in figure 46.

We conclude that the result of 2.5 GeV reported in the Smirnov presentation is due to low statistics and is thus an effect of statistics that have not converged.

Finally, using high statistics we then do an energy deposition plot for the crystal used in the 2012 study, the strip-foil crystal and quasi-mosaic crystal used in the 2019 experimental study for a beam size varying between 0.3-0.5 mm in both transverse directions.

We use the beam parameters used during the experimental run in 2019 shown in figure 43 and present only the most strict limit of 0.3 mm for the beam width in both directions to see if we exceed the melting point.

On the figures 48, 49, and 50 we see the energy deposition scored for each direction in the crystal. The significant energy deposition happens in the longitudinal direction of the crystal where the energy deposition increases proportionally with the length of the crystal. There is a cutoff for the energy deposition in the z-direction for the LHC crystal used in the 2012 study and for the strip-foil crystal STF103 used in the 2019 experimental study. This is due to the crystal length being only 2 mm, while for the quasi-mosaic crystal QMP33 the crystal has a length of 4 mm which is why the cutoff for these crystals correspond to their length.

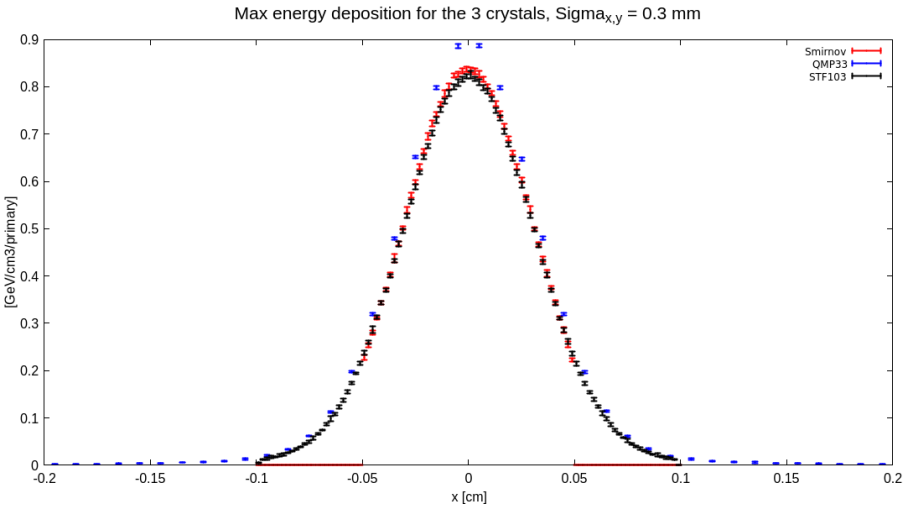

Figure 48: The one-dimensional energy deposition in GeV/cm^3 as a function of the x-coordinate in cm in three different Silicon crystals. The beam width is 0.3 mm for both x and y direction of the beam profile. Shown in red is the distribution for the strip-foil crystal used in the 2012 study, in blue the quasi-mosaic crystal used in the experimental 2019 study, and in black the strip-foil crystal also used in the experimental study. We see a smooth Gaussian distribution centered around 0 for the x-coordinate. We see a slightly higher max energy deposition for the quasi-mosaic crystal which has to do with its crystal being longer than the other two.

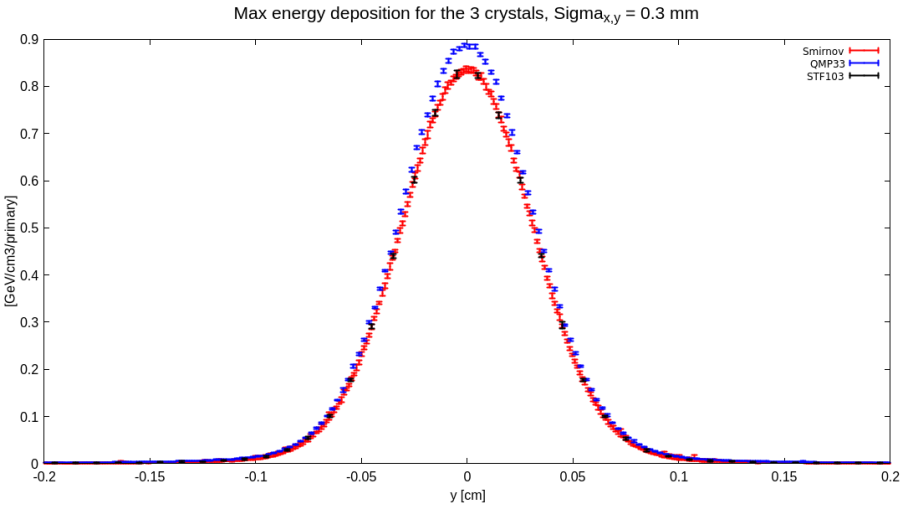

Figure 49: The one-dimensional energy deposition in GeV/cm^3 as a function of the y-coordinate in cm in three different Silicon crystals. The beam width is 0.3 mm for both x and y direction of the beam profile. Shown in red is the distribution for the strip-foil crystal used in the 2012 study, in blue the quasi-mosaic crystal used in the experimental 2019 study, and in black the strip-foil crystal also used in the experimental study. We see a smooth Gaussian distribution centered around 0 for the y-coordinate. We see a slightly higher max energy deposition for the quasi-mosaic crystal which has to do with its crystal being longer than the other two.

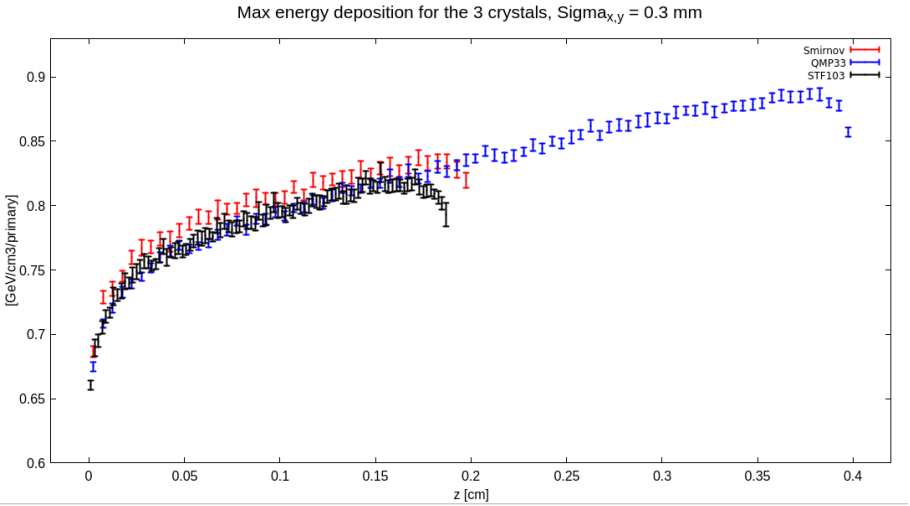

Figure 50: The one-dimensional energy deposition in GeV/cm^3 as a function of the z-coordinate in cm in three different Silicon crystals. The beam width is 0.3 mm for both x and y direction of the beam profile. Shown in red is the energy deposition for the stripfoil crystal used in the 2012 study, in blue the quasi-mosaic crystal used in the experimental 2019 study, and in black the strip-foil crystal also used in the experimental study. We see a cutoff for all three crystals corresponding to the length of the crystals. The maximal energy deposition is found for the quasi-mosaic crystal which is expected since it is the longest crystal.

For the 4 mm long crystal this results in a higher energy deposition since the total energy deposition is proportional to the length due to the expression for nuclear interaction length.

The nuclear interaction length is defined as the length a particle would have to travel in a material before undergoing an inelastic reaction with the solid. This means that you expect a higher energy deposition in a longer material, since more interactions take place, but due to the thin lengths of the crystals considered this is an negligible effect for our case.

Crystal	T [K]
QMP33	1563 K
STF103	1472 K
2012 study crystal	1487 K

Table 1: QMP33, STF103, and the crystal from the 2012 Smirnov et al study. The energy depositions have been translated into temperature increases and has been accounted for varying heat capacity by integration of C_p.

In conclusion we see that for all three crystals with the most strict constraint on the beam width of $\sigma_{x,y} = 0.3$mm we find energy depositions that when translated into a temperature increase under the assumption of adiabatic heat transfer, are all below the melting point of Silicon and thus the crystals used in the LHC should see no damage due to an accidental full-on LHC beam neither during an SPS injection into the LHC at 440 GeV or during operation in the LHC at maximum energy at

7 TeV. The simulated temperature increases due to energy deposition from beam impact is listed in the table 1

Furthermore the presented result of 2.5 GeV energy deposition into the LHC crystal used in the 2012 simulation study by Smirnov et al was due to low statistics that did not converge which resulted in a statistical outlier which was presented as the maximal energy deposition.

7.3 Radiation damage

What remains now is to consider the displacements per atom (dpa) induced in the crystal and also simulated in the 2012 study.

When the crystal is exposed to the LHC beam during regular operation, the beam halo at 6σ is constantly under the melting and brittle-to-dust threshold and the temperature increase makes out less than 1K.

Displacements per atom is considered as radiation damage, where we have a binary outcome. Either we have a displacement in the atomic lattice or we do not. This is in contrast to the thermal damage coming from energy depositions from scattering and friction with electrons in the material, which can produce delta rays which further spreads the heat generated as described above.

In general as proton energy increases the nuclear interaction cross section also increases. But for a thin crystal of thickness $z \sim 2$ mm the total probability for nuclear interaction does not increase much even when struck by the beam core. This is why the thermal properties of the beam on the Silicon crystal are the most significant for investigation of crystal damage. That being said we still need to consider the displacements which can be induced by neutrons, electrons, ions and gamma rays all produced doing nuclear interactions in the crystal. Prior studies have already shown that the dpa is already low in Silicon crystals, and if the crystal is in channeling orientation it becomes even lower.

The 2012 study refers to an article[8] where the NA48 crystal (1x10x50 mm^3) was irradiated in the SPS T6 with 450 GeV protons for a full year with a total beam fluence of 2.4×10^{20} p/cm^2 and beam area of 0.24 mm^2 FWHM (0.8 mm $\times$ 0.3 mm). They find a dpa of 0.4 dpa/cm^3. The 2012 study also did a Fluka simulation of dpa using the dimension of the NA48 crystal and found that for a 7 TeV LHC beam, the reduction in deflection efficiency per year was only on the level of 0.4% per year.

Finally the 2019 experimental study also did post irradiation tests of the crystals used were they saw a negligent amount of deterioration in the channeling efficiency of the irradiated crystal.

The studies all conclude that the limiting factor for the tests of crystal robustness is not the dislocations of atoms but rather the thermal damage.

8 Loss map analysis

Now that we have covered the process of characterising a Silicon crystal for use in a crystal assisted collimation system as well as studied its robustness, we can now look into applying it for studying the efficiency of a collimation system.

We wish to have an idea of where particles are lost in the accelerator aperture due to interactions with the crystal or due to inelastic collisions or a loss of energy. As described in chapter 2.1 magnetic fields and off-momentum particles leads to dispersion where the closed orbit of particles deviates and becomes comparable with the beam pipe radius resulting in the particles being lost and depositing their energy.

As the primary protons from the source impact on the crystal some undergo nuclear interactions with the crystal and are stopped, and some undergo scattering interactions with the crystals such as channeling, dechanneling, volume capture, volume reflection, or amorphous scattering. After interacting with the crystal those particles not stopped continue their trajectory through the accelerator, where some reach the end of the geometry defined in the simulation, some impact on the absorbers as intended, and some are lost elsewhere in the aperture such as at the magnets or the beam pipe walls due to effects like dispersion.

8.1 Loss map setup

We can track these losses by doing a simulation on particle losses and producing a loss map. A loss map is a histogram of where primary, secondary, and higher order particles are hitting the pipeline walls or other aperture. It is a way of visualizing where primary particles and produced secondary particles will deposit energy their energy thus creating hot regions in the accelerator. We do the simulation for the LSS5 layout of the SPS, where the absorbers are placed.

The simulation we did was done with a setup of a Silicon crystal in the beginning of the aperture at $s = 97.1$ cm, and just upstream of it a beam source with an angular distribution centered about an angle matching with the crystal plane orientation. Downstream of the crystal on the beam line the absorbers are installed. The first absorber is the Tungsten absorber TACW at $s = 4940$ cm, and downstream of it is the Carbon absorber TCSM at $s = 9150$ cm. The setup can be seen in the Flair geometry and with corresponding coordinates for the crystal and absorber in the figure 51.

A loss map is shown on the figure 52 where the histogram is the s coordinate in the accelerator with $s = 0$ corresponding to the start of the defined geometry with respect to the reference element in the simulation files. On top is plotted the dispersion function, which shows where losses should be more pronounced for off-momentum particles. For this simulation run the Carbon absorber is on the beam line thus intercepting the particles earlier on the beam line.

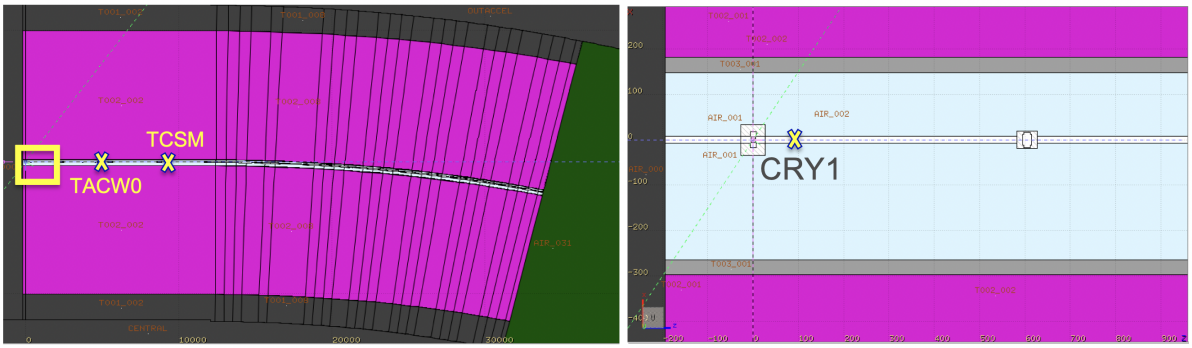

	CRY1	TACW0	TCSM
Position [cm]	97.1	4940	9150

Figure 51: The simulated LSS5 layout of the SPS accelerator in the Flair geometry window. To the left is seen a zoomed out picture of the whole LSS5 simulated with the BLACKHOLE regions marked in dark grey. To the right is a zoomed in picture of the start of the LSS5 to better see the Silicon crystal position. Here the Air region is seen in light blue, the internal and external wall of the complex in light grey, and the beam pipe and other aperture in white. The bottom table shows the longitudinal coordinate s in cm for the crystal, Tungsten absorber and Carbon absorber.

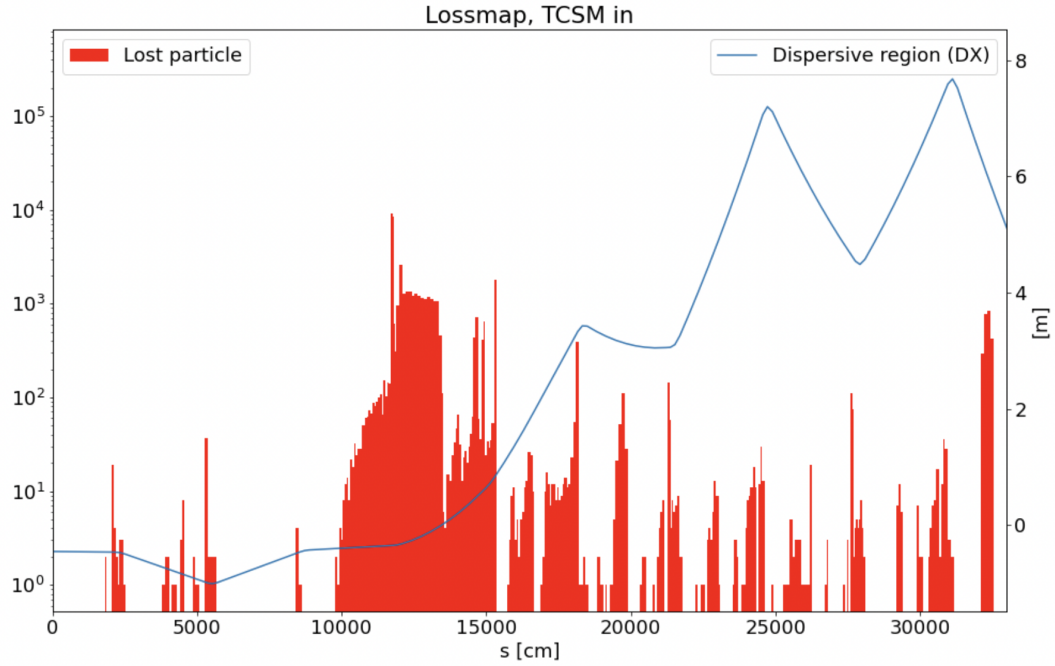

Figure 52: The location s in cm of all the lost particles in the beam line. Plotted on top is the dispersive regions, indicating the dispersive peaks. The plot does not include the region corresponding to the end of the defined geometry, otherwise there would be a large spike indicating a false particle loss which would correspond to the terminated particles.

8.2 Comparison

By running the simulation twice, once with the Tungsten absorber in place and another with the Carbon absorber, we can compare the amount of leakage from production of secondary particles due to interactions with the absorbers for each absorber material, compare the location of the losses, as well as compare the dynamics of the particles. The leakage is simply the rate of higher order particles produced that are lost in the beam line. They are produced as a result of nuclear interactions from the beam particles with accelerator material such as the absorbers.

For this study of particle losses we simulated $N = 10^6$ protons in the beam line. The loss maps in the figures 53 and 54 below show us where in the beam line each particle is lost, what species the particle is, and the relative frequency.

8.2.1 Loss maps

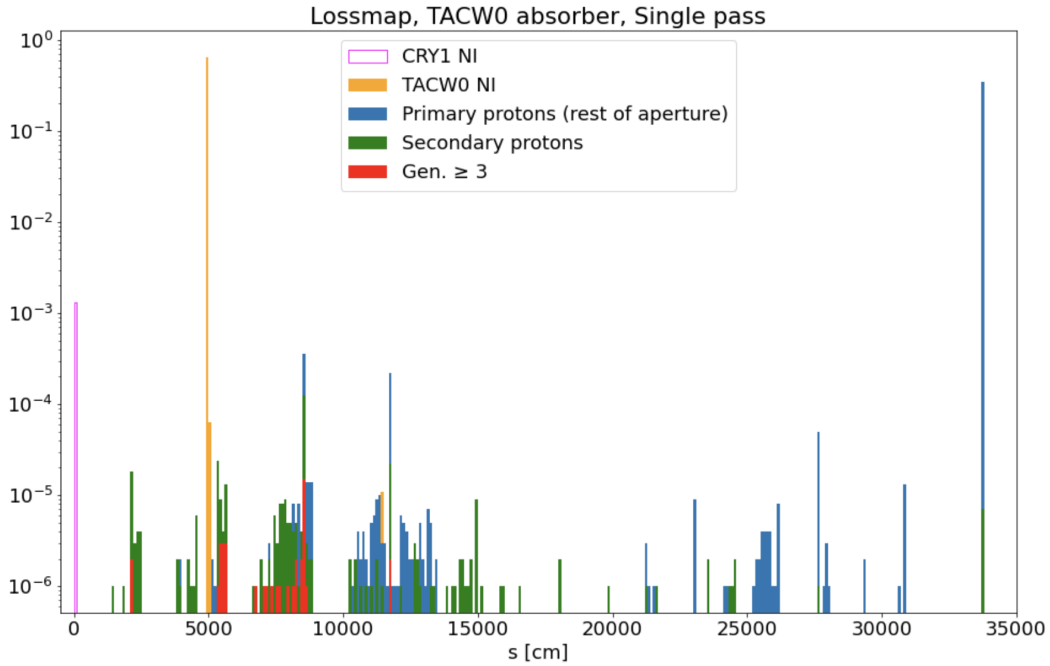

Figure 53: The normalised histogram making out the loss map showing the location s in cm of all the lost particles in the beam line with the Tungsten absorber in place. The loss map shows the population of nuclear interactions in the Silicon crystal in pink, the nuclear interactions in the Tungsten absorber in yellow, the primary protons lost in the aperture in blue, the lost secondary protons in green, and the higher order particles in red. The right-most data spike is the particles terminated due to reaching the end of the geometry.

The loss map is a histogram that shows the occurrence of particles at longitudinal coordinate s in the LSS5 layout labeled by colours. The primary protons are shown as the blue distribution. Secondary protons, defined as protons that have interacted elastically giving them an off-momentum, are shown in green. Higher

Region	Number of particles
Crystal	1300
TACW	650580
Aperture	942
Generation $\geq$ 2 particles	419
Reaching end of geometry	347176

Table 2: Table quantifying the losses of the $N = 10^6$ protons and additionally the amount of higher order particles for when the Tungsten absorber is on the beam line.

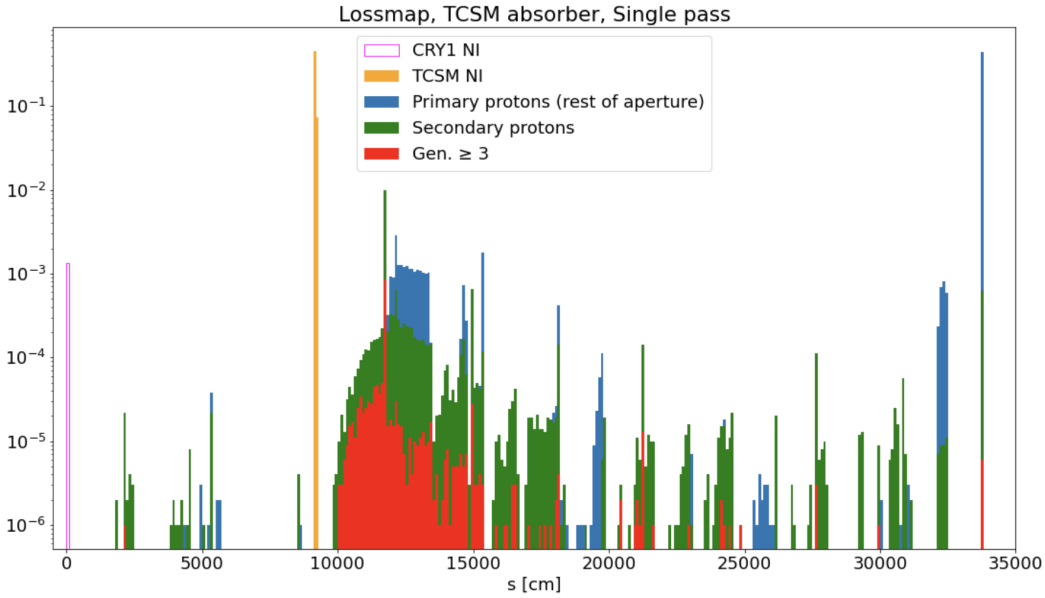

Figure 54: The normalised histogram making out the loss map showing the location s in cm of all the lost particles in the beam line with the Carbon absorber in place. The loss map shows the population of nuclear interactions in the Silicon crystal in pink, the nuclear interactions in the Carbon absorber in yellow, the primary protons lost in the aperture in blue, the lost secondary protons in green, and the higher order particles in red. The right-most data spike is the particles terminated due to reaching the end of the geometry.

Region	Number of particles
Crystal	1317
TCSM	525820
Aperture	34274
Generation $\geq$ 2 particles	20678
Reaching end of geometry	438589

Table 3: Table quantifying the losses of the $N = 10^6$ protons and additionally the amount of higher order particles for when the Carbon absorber is on the beam line.

order particles produced during nuclear interactions during the primary proton colliding with the absorber material producing particle showers are shown in red. The pink distribution is showing the nuclear interactions happening inside of the Silicon

crystal that collimates the protons and makes out about 0.13% of the simulated particles as shown in the tables 2 and 3. Finally the nuclear interactions happening inside the absorbers is given by the yellow distribution, and are given at different longitudinal coordinates for the case with a Tungsten absorber in place figure 53, and the case with a Carbon absorber in figure 54.

For both cases the histogram is logarithmic and normalised to show the relative frequency. The very last column on both plots shows the end of the geometry where the particles are being terminated and thus are not to be considered as actual losses.

From this we can see that the highest frequency of particle collision happens at the absorbers. Here we see from the table that 34.7% of the particles reach the end of the defined geometry when the Tungsten absorber is in place, and 43.9% reach the end of geometry when the Carbon absorber is in place.

If we do not include the particles reaching the end of the geometry then the nuclear interactions in the absorbers make out 99.7% and 93.7% of the losses for the Tungsten absorber and the Carbon absorber respectively.

From the figures 53 and 54 the most significant difference is seen in the abundance of higher order particles, meaning second order particles or higher. For the case of the Tungsten absorber on the beam line the higher order particles make out about 0.042% of the particles, and 0.064% when not including particles at the end of the geometry. Meanwhile for the Carbon absorber on the beam line the higher order particles make out about 2.1% of the particles, and 3.7% when not including particles at the end of the geometry.

Thus, there is a factor 50-57 reduction in secondaries produced when using the Tungsten absorber with lower nuclear interaction length compared to when using Carbon absorbers. Hence, it seems that the Tungsten absorber leads to a higher cleaning efficiency of the collimation system when considering this result.

8.2.2 Impact on absorbers

We can see from the tables 4 and 5 that for both absorbers more than 99.9% of the particles impacting on the absorber are either channeled or dechanneled particles. From this it can be extrapolated that only particles that have interacted with the crystal have enough deflection to be able to reach the absorbers.

Specifically looking at the impacting primary particles with the Carbon absorber in figure 55 we can see distinct regions for the particles based on their interaction with the crystal. We analyse the normalised logarithmic histogram of the transverse plane of the absorbers in the horisontal direction.

We notice that for the TCSM the distributions of particles are on both sides of the center transverse plane indicating that the absorber has two collimator jaws that are being struck. The collimator jaw is the region of the absorber that consist of the absorbing material meant for interception of high energy particles, and they function as a beam dump. For the TACW the distribution is only seen to the left of the center, since it is a single jaw absorber.

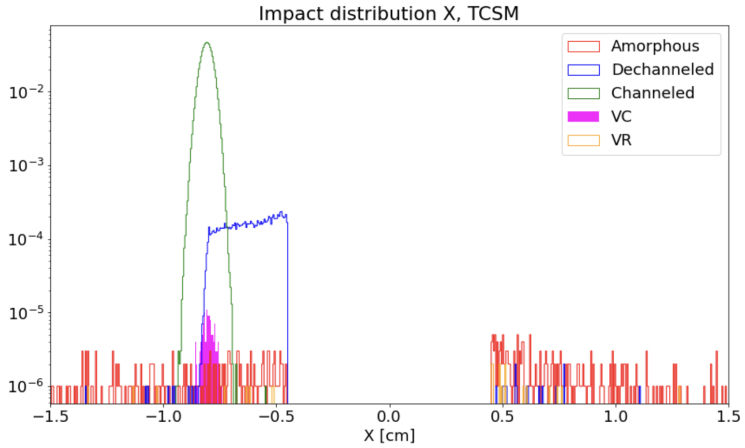

Figure 55: Histogram of the population of particles that impact on the Carbon absorber in the transverse plane. Seen on the plot is the distribution of particles and their horisontal impact on the absorber as well as their interaction with the crystal given by the legend.

Interaction	Occurrence in %
Channeled	98.1%
Dechanneled	1.8%
Amorphous/Volume Capture/Volume Reflection	<0.1%

Table 4: Table showing for the particles that hit the Carbon absorber what interaction they have undergone with the collimating crystal. Channeled and dechanneled particles make out over 99.9% of the particle population impacting on the absorber.

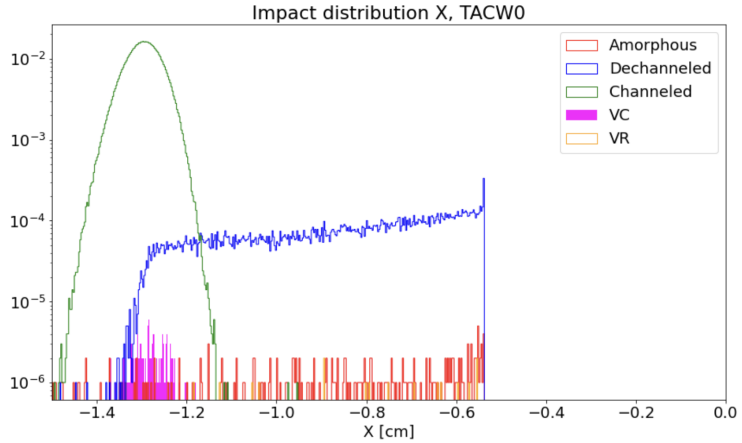

Figure 56: Histogram of the population of particles that impact on the Carbon absorber in the transverse plane. Seen on the plot is the distribution of particles and their horisontal impact on the absorber as well as their interaction with the crystal given by the legend.

The Gaussian shape in green shows the distribution of channeled particles impacting on the absorber. The square distribution in blue shows the population of dechanneled particles. The cutoff corresponds to the edge of the collimator jaw, thus indicating the rest of the distribution continuing its trajectory through the beam-

line. The volume captured particles are also seen making out a Gaussian structure indicated by the magenta distribution in the histogram. The red distribution is given by the amorphous interactions seen by their homogeneous distribution, and finally the yellow distribution is the volume reflected particles.

Interaction	Occurrence in %
Channeled	96.4%
Dechanneled	3.5%
Amorphous/Volume Capture/Volume Reflection	<0.1%

Table 5: Table showing for the particles that hit the Tungsten absorber what interaction they have undergone with the collimating crystal. Channeled and dechanneled particles make out over 99.9% of the particle population impacting on the absorber.

8.2.3 Momentum distributions

Looking at the figures 57 and 58 we see a scatter plot of the off-momentum $\delta p/p$ in GeV belonging to the lost particles versus the longitudinal coordinate s in cm in the accelerator where the particles were lost at.

On the plot is shown the primary protons lost in blue, secondary protons in orange, and higher order particles in green. All the particles plotted have been lost in the aperture, meaning that particles that have undergone nuclear interactions with the crystal or absorber are not included. Furthermore, on the plot is shown the locations of quadropoles and absorbers in colour bars. The straight section of the accelerator is shown by the light green shade, and the bending section of the accelerator is shown in a light blue shade. The quadropoles are placed in the straight section and the dipoles in the bending section.

We see a clear pattern, that the more off-momentum particles are lost early on in the beam line, and that many of the losses happen at or nearby the quadropoles. There is a decaying tail structure of the particles towards the end of the geometry. This makes sense since the higher the off-momentum of the particle is, the more deflected its closed orbit becomes from the dipole fields, thus increasing the likelihood that the particle will be lost. So, the particles reaching the end should have a low off-momentum.

For the Carbon absorber figure 58 we see that most of the losses are concentrated around the focusing quadropole downstream of the Carbon absorber. We saw before that the majority of losses in the loss maps are nuclear interactions in the absorber, but the losses shown here are only for particles lost in the aperture, meaning excluding the crystal and absorbers. The high abundance of higher order particles is caused by the nuclear interactions with the absorber material producing many higher order particles just downstream of it. These particles are lost early on due to their high off-momentum, meaning that their closed orbit gets deflected strongly.

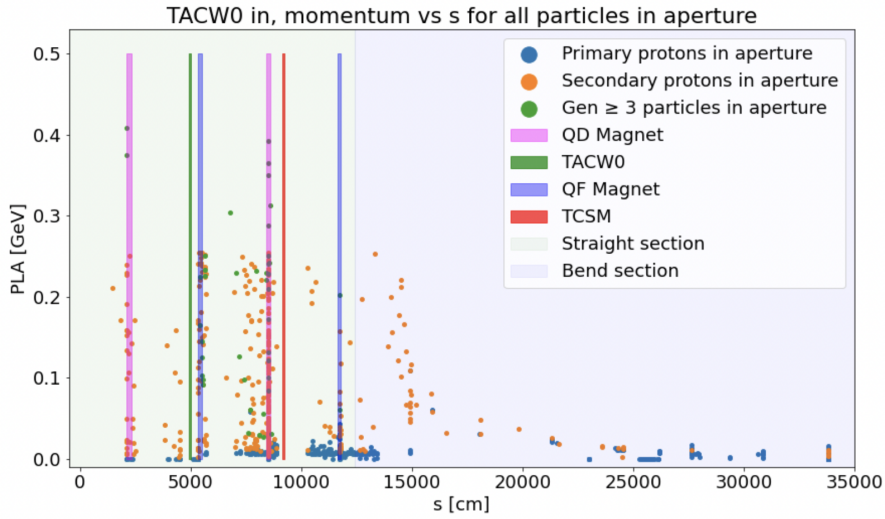

Figure 57: Scatter plot of the off-momentum $\delta p/p$ in GeV belonging to the lost particles versus the longitudinal coordinate s in cm they were lost at in the accelerator when the Tungsten absorber is on the line. Seen are the primary protons lost in blue, secondary protons in orange, and higher order particles in green. The locations of quadropoles and absorbers are indicated by colour bars. Additionally, the straight section and bending section of the accelerator are shown in a light green and blue shade respectively.

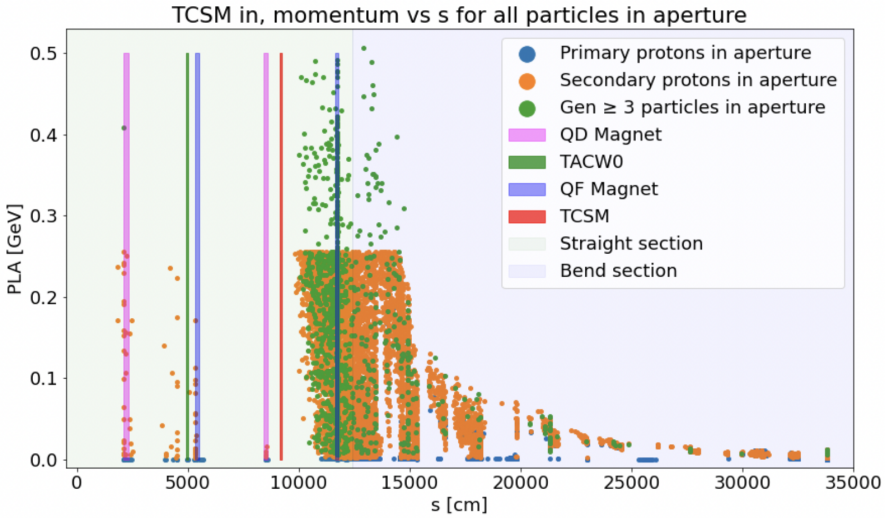

Figure 58: Scatter plot of the off-momentum $\delta p/p$ in GeV belonging to the lost particles versus the longitudinal coordinate s in cm they were lost at in the accelerator when the Carbon absorber is on the line. Seen are the primary protons lost in blue, secondary protons in orange, and higher order particles in green. The locations of quadropoles and absorbers are indicated by colour bars. Additionally, the straight section and bending section of the accelerator are shown in a light green and blue shade respectively.

8.3 Thoughts on single pass simulation

In principle, had the simulation been an experimental run, the particles that are terminated at the end of the defined geometry in the simulation would have taken multiple turns in the accelerator complex until they were lost somewhere in the aperture or intercepted by the absorber.

We wanted to include this in the simulation and did so by changing the Fortran code, so that a translation would happen as the particle crossed the boundary region defined at the end of geometry. It would take all the parameters of the particle like the angle and momentum, and extrapolate the particles evolution for the span of the accelerator complex until the particle is at the beginning of the LSS5 layout of the SPS again, as if it had traversed through the whole accelerator. This would neglect the possibility of a particle being lost in the aperture from the end of LSS5 and back to the beginning of it making out about 6.5 km of runway.

The change in code seemed to work for the case where the Carbon absorber was in place and successfully collimated the multi turn particles on the absorber. But with the Tungsten absorber in place there was a systematic error, where the translated particles were lost right next to the Tungsten absorber but hitting the aperture, and there was a relation between number of turns the particle had taken and how far from the absorber it was lost.

We tried to debug the code but could not identify the reason for this anomaly and thus these results were discarded and not included. Therefore the study conducted only considers the single pass of protons in the collimation setup, which is why the relative abundance of particles hitting the absorber is low when including the particles being terminated at the end of the geometry. When including all $N = 10^6$ protons only 65% and 53% are hitting the Tungsten and Carbon absorber respectively as seen in the tables 2 and 3 respectively.

This means that our simulation is limited when it comes to say anything conclusive about the comparison of the absorber materials in a crystal assisted collimation system. The collimation efficiency is underestimated when including the particles reaching the end of the geometry in the estimation of the efficiency.

9 Beam Loss Monitors

Beam loss monitors (BLM) are used to monitor the beam losses while the beam is operational and serves to automatically send a signal to stop the beam in case a major change in the losses happens due to an accident or unforeseen changes in the beam. They also score the energy deposition from nuclear interactions in the accelerator close to it. They provide a way of tracking the hot regions around the accelerator and thus serves as a fitting tool for when doing radiation studies and testing the setup of a collimation system. They can be included in the simulation as an off-beam element as mentioned back in chapter 6.

Back in the year 2018 an experimental study on crystal channeling was performed in the SPS by the UA9 collaboration. The goal was to compare the leakage using two different absorber materials. A Tungsten TACW absorber and a Carbon TCSM absorber. Using a Silicon crystal and a source providing a beam halo going through the crystal, the crystal then deflects these particles onto an absorber via the channeling interactions described in chapter 3. The experimental run was concluded by presenting the results of the study in a bar graph showing the reduction factor, which is a way of quantifying the energy deposition as a ratio when applying a crystal in channeling orientation and in its amorphous orientation. This is the result we wish to recreate and compare, so that the simulation study serves as a comparable to the experimental results.

To do so, we need to place eight LHC-type beam loss monitors around the accelerator complex in the LSS5 layout of the SPS to measure the energy deposition in the same areas as for the experimental run. Thus, the first step to would be to find the eight locations of the BLMs used in the experimental run.

9.1 Method for finding BLMs

We want to reuse the configuration used in the 2018 setup. The end goal is to reproduce the results of the 2018 experimental run that show the reduction factor for the energy deposition in the BLMs for eight positions, when having the crystal in channeling orientation and in amorphous.

Before starting the simulation we have to simulate the conditions that the experiment was performed under in 2018. This means that we have to find the exact locations of the eight BLMs in the LSS5 layout and insert into our simulation.

Therefore, our task is to locate these BLMs, measure their distance to adjacent aperture, and enter this information into the auxiliary files of the simulation. We start out by getting a crude overview of what apparatus is close to the BLM via the documentations of the experimental run, and from there we look at the schematic drawings to pinpoint the location more accurately using a ruler that is included on the drawings. When we have a rough idea of where to look for the BLM we need to confirm that it was installed during the 2018 operation period. For this purpose CERN provides a Google Street View inside of its accelerator complex and here we

went looking for the beam loss monitors positions in the SPS in the year 2018. An example can be seen on the figure 59 below where we locate the beam loss monitor number four out of eight when ordering them downstream of the crystal location.

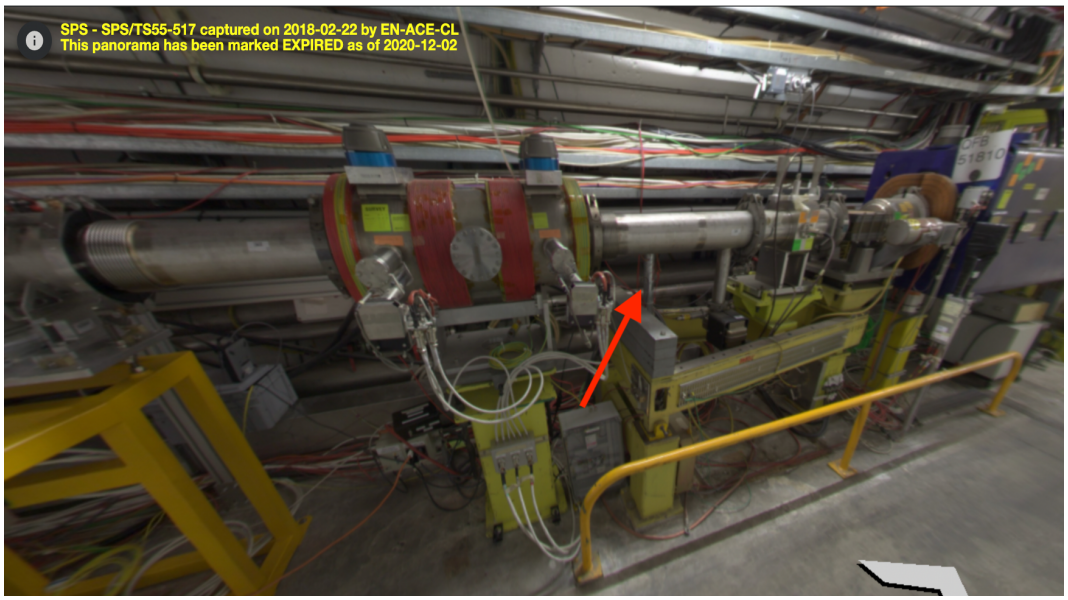

Figure 59: The Google Street View referred to as the panoramic view of the SPS accelerator. Here we see the foot of a BLM placed towards the internal wall of the complex. The body of the BLM is covered by the beam pipe, and therefore we use the foot indicated by the red arrow as confirmation of its presence on the beam line. The panoramic view allows on to change the year the photograph was taken, so you can see how the beam line equipment is switched between experimental runs.

Some BLMs are parallel with the beam line and others perpendicular to it, and some are placed closest to the external wall and others to the inner wall. Now to find out which way they should be oriented and where they should be placed we make use of schematic drawings of the SPS layout in combination with this panoramic view to manually estimate the position before finally implementing the BLM into the Fluka simulation.

On the figure 59 for the fourth consecutive BLM we do not directly see the body of the BLM since it is placed towards the internal wall of the complex and thus its body is hidden by the beam pipe. We notice that the foot of the BLM is showing to confirm its presence which is indicated by the red arrow on the photograph.

We have to manually estimate the exact location horisontally and vertically on the beam line by using the ruler in units of mm on the top line of the schematic drawing as shown in the figure 60. This is done by inserting a straight line directly into the image editor of the PDF file of the schematic drawing and matching it with the ruler over the box. This line is then duplicated and cut into smaller segments and placed adjacently from a known starting point in the geometry.

For example for the BLM shown in the schematic drawing figure 60, where we use the end coordinate of the TACW location and add line segments until reaching the center position of the beam loss monitor on the drawing. For this case with the

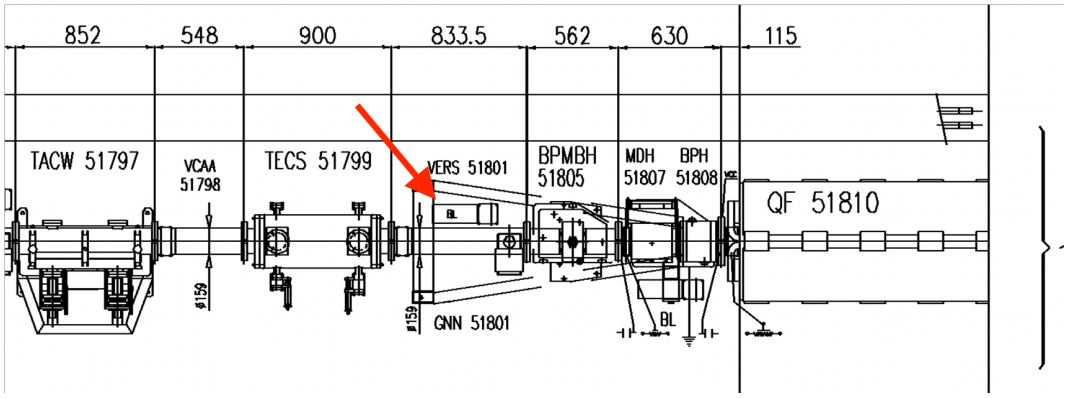

Figure 60: Schematic drawing showing the BLM indicated by the red arrow. We use the horisontal and vertical rulers on the drawing to estimate the position. The position is put into the ROT-DEFI file and the BLM is implemented onto the simulated beam line.

fourth consecutive BLM we find that the center of the BLM is placed a horisontal distance of $d_h = (1865 \pm 23.68)$ mm downstream of the edge of TACW.51797, found by adding the two documented full line segments from the schematic (548 mm+ 900 mm) and then adding the final part from the method of dividing up the ruler as mentioned above (417 mm). We then find a vertical distance of $d_v = (160 \pm 6.45)$mm upwards of the beam line center also documented by the schematic drawing's vertical ruler.

Since this measurement is done manually in the image editor of the PDF file and the scale is only a question of how far we are zoomed in on the image, the uncertainty on the measurement has been estimated to follow the pixel resolution. We count the 833.5 mm horisontally on 176 pixels and vertically the 160 mm is counted on 124 pixels. By then considering a qualitative accuracy of estimating the center within 5 pixels the uncertainty becomes $\sigma_h = \frac{833.5mm}{176} \times 5 = 23.68$ mm, and vertically $\sigma_v = \frac{160mm}{124} \times 5 = 6.45$ mm. The 5 pixels correspond to the image resolution of the lines in the image, meaning how many pixels wide the lines are in the image.

When the exact distance has been calculated to a reference object on the beam line, we add the BLM into the Fluka geometry by defining a cylinder corresponding to the physical dimension of an LHC-type BLM from the bodies files. These are added to an external auxiliary file, where all eight BLMs are defined. Here the found distance is added to the reference element's Fluka coordinate and in the ROT-DEFI file the translation and rotation of the BLM takes places like described in chapter 6 and shown on the figures 35 and 36.

Then the Fluka code implements these structures in on the simulated beam line when the BLMs are activated in the main simulation code which calls the auxiliary and ROT-DEFI files containing the BLM parameters. The BLM is then added onto the simulation beam line as shown in the Flair graphic on the figure 61 showing the Flair interactive geometry window of the fourth BLM.

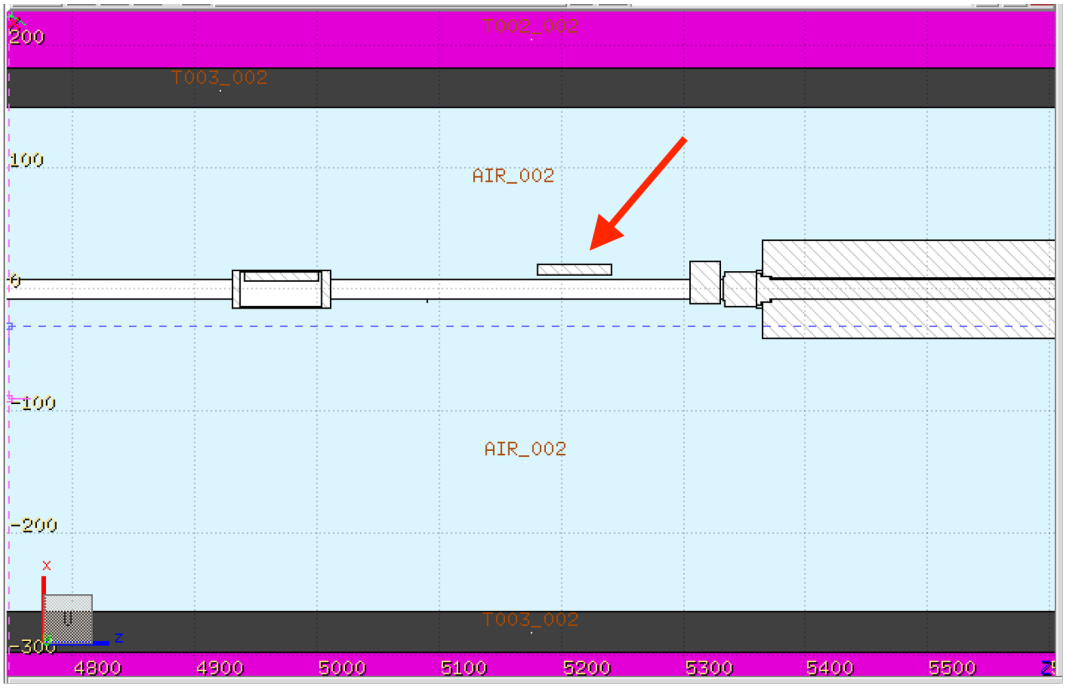

Figure 61: The Flair interactive geometry served as a great help for the placement of the BLMs. The geometry window allowed to inspect the placement of the object from all direction. This was very helpful when placing the BLMs that were rotated 90 degrees and translated under the beam pipe.

It is worth noting that when comparing the Flair geometry of the LSS5 with the panoramic view of the complex and the schematic drawing we see that the simulated beam line is much simpler, meaning that we neglect including much of the aperture that is not relevant for the simulation, such as the roman pots. Our simulation includes the crystal, absorbers, dipole magnets, and quadropole magnets. This means, that when considering the fourth BLM in our example, we see that there is nothing shielding the BLM in the distance between it and the Tungsten absorber where the particles are interacting, opposed to what can be seen from the panoramic and the schematic drawing.

This is generalised for all eight BLMs present in the simulated beam line. Therefore we would systematically expect to get a higher absolute energy deposition in the multi turn simulation than for the experiment where some natural shielding is occurring from intercepting machinery. But as mentioned in the prior chapter our simulation is of a single pass of the particle.

9.1.1 Missing material on localising beam loss monitors

Above an example was shown of localising the fourth consecutive of eight beam loss monitors downstream of the crystal where all information was congruent for all three sources, the photography of the beam line, the schematic drawing, and the layout overview shown in the appendix I. Multiple BLMs had conflicting sources on their location.

Shown on the figures 62 and 63 is the example of BLM.51654 which is seen on the photograph of the beam line for the year 2017 confirming its presence (a photo of this exact region was not available for the year 2018). But on the schematic drawing it is not present. Instead where it is supposed to be located, the drawing states "*To be checked*". In this case the placement of the BLM had to be done without any other reference than the photograph, which was also done at an impractical angle. Additionally the photo has been marked as expired as of February 2018, but the BLM was used in the experiment.

Multiple BLMs were missing either in the schematic drawing, or were showing a conflict between panoramic view and schematic drawing. Another example is where the panoramic showed a BLM with its longitudinal axis parallel with the beam pipe but the schematic drawing stated it was oriented perpendicularly to the beam pipe. Other cases showed the BLMs on the opposite side of the beam pipe than the panoramic showed, and in other instances like for the BLM.51654 above, the BLM is simply not included in the schematic drawing. This is the case at multiple locations and is documented in the appendix I.

Figure 62: Panoramic view showing the presence of the BLM.51654 downstream of the TECS.51651. The photo is marked as expired as of February 2018.

Additionally, the naming of the BLMs is based on which segment of the schematic drawing they belong to, but also here the naming does not fit the schematic drawing's numeration, since multiple layout changes has been made throughout the years, but the naming had to stay the same to avoid confusion with earlier experiments. This is also why the numeration frequently skips multiple concurrent segments of the beam line. Cross checks were done for the BLM placements. Multiple excel sheets stating the locations and names had inconsistencies, where we would have located a BLM to within ± 1 m horisontally but the naming would be conflicting. Also here there would be confusion due to name changes induced by a change in the layout of the beam line. In the end the found locations were cross checked with the group executing the 2018 experimental run to confirm the BLMs that were included in this study.

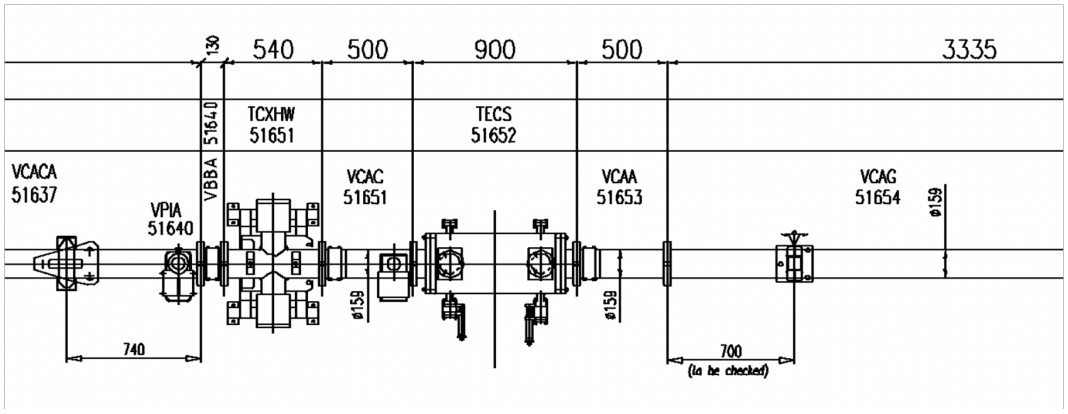

Figure 63: Schematic drawing showing the area where the BLM.51654 was situated during the 2018 experimental run. It is not present on the schematic drawings and instead replaced by a text stating: "*To be checked*".

9.2 BLM placement

As mentioned above the layout was used in an experimental setup. Now we need to incorporate it into our simulation of the LSS5 layout by implementation into the Fluka code with the found BLM positions.

First we need to activate the BLMs in the Fluka routines. This is done by going into the prototypes file and uncommenting the section that actives LHC-type BLMs. To score energy deposition we need to change the scoring setting within the inputcard.txt from : abd : to : ed :. This corresponds to changing tracker settings from advance beam dynamics simulation to energy deposition simulation. We then go into the file governing the physics settings and add the scoring of the energy deposition in the BLMs.

This is followed by going into the inputcard.txt file and uncommenting two lines that activate the usage of the BLM auxiliary file to set the position and name of the BLMs, as well as activating the ROT-DEFI file to configure the position away from the center of the beam and rotation of the BLMs. This is necessary since BLMs are considered to be off-beam objects and thus do not appear in the twiss files and must be placed manually. The twiss files are a directory of standard equipment used in simulations which are automatically added when for example changing the key word for what kind of simulation is performed in the inputcard.txt file, but the BLMs are not considered standard equipment and so must be inserted manually by filling out auxiliary files.

Eight regions were chosen as regions of interest as per our analysis of the loss map in the prior chapter. These regions include at the crystal placement, the absorber locations, and dispersive regions but are dictated by the locations used in the experimental 2018 setup. The regions can be seen on the figure 64 where we see the BLM locations shown on the axis corresponding to longitudinal coordinate in the accelerator s by black dashed lines, and the aperture in the beam line shown by colour bars indicating the locations of the crystal, absorbers, and the quadropoles.

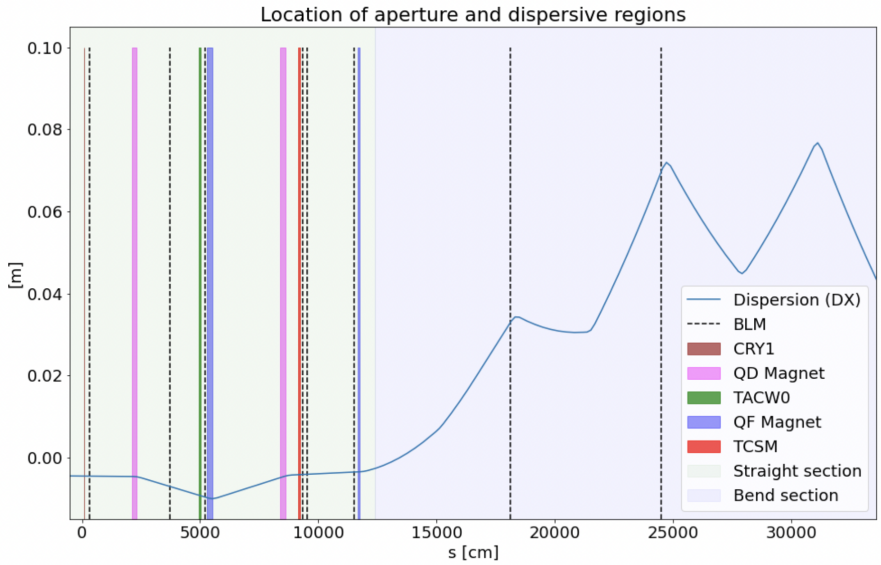

Figure 64: Beam loss monitor locations around the LSS5 layout. The beam loss monitors are shown as black dashed lines, the quadropoles are shown in magenta and blue colour bars, the crystal in brown, the Tungsten absorber in green, and the Carbon absorber in red. The straight section and bending section is shown by the light green and light blue shades respectively.

The straight section and bending section of the accelerator is shown by the light green and light blue shade respectively. The straight section is where the quadropoles are placed, and the bending section is where the dipole fields bending the trajectory of charged particles. This is also the region where the dispersion leads to greater deflection of the closed orbit as described in chapter 2 and indicated by the dispersive peaks on the figure.

9.3 BLM Reduction factor

The quantity used in the 2018 experiment to quantify the amount of radiation in specific regions of the SPS is the reduction factor.

Shown in the figure 65 the reduction factors for the 2018 experimental run are shown. These are the data we wish to compare with out simulation study.

For each BLM the energy deposition is scored for when the crystal is in its channeling orientation and when it is not. The reduction factor is then the ratio of the energy deposition for the given BLM when there is amorphous scattering on the crystal crystal relative to when the crystal is channeling particles. Thus, a reduction factor below 1 corresponds to regions where there is a higher energy deposition for when the crystal is channeling particles compared to when it is not. Vice versa, where we have high values of the reduction factor means that there is a much higher energy deposition in the area when the crystal is not channeling compared to when there is channeling. Thus a high reduction factor corresponds to high reduction in energy deposition in that area when a crystal is in use and channeling the particles.

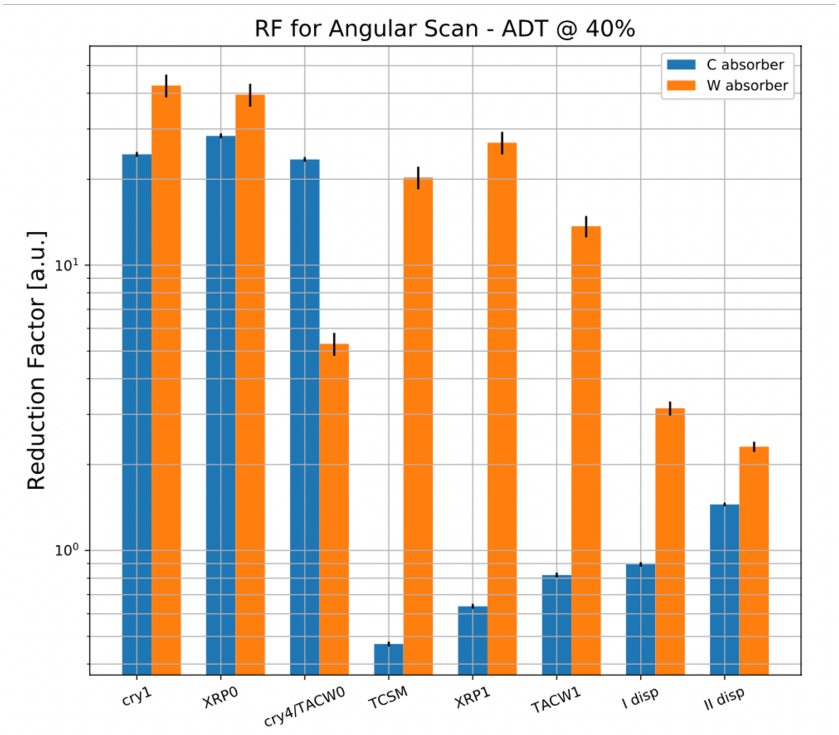

Figure 65: The results for the 2018 experimental study done in the UA9 collaboration for the energy deposition in 8 placed beam loss monitors around the LSS5 layout of the SPS. The bar graph shows the reduction factor at the 8 locations for when having the Carbon absorber on the beam line shown by the blue bars, and for when the Tungsten absorber is in shown by the orange bars. The results are produced for multi turn passage of the particles

The results of the reduction factor of the simulation is shown in the figure 66.

As expected we see a low reduction factor for the locations corresponding to the absorber that is in use for the run, since the channeled particle is intentionally steered towards the absorbers to localise the hot regions. A high reduction factor is expected when considering the BLM placed at the crystal, since here in its amorphous orientation more nuclear interactions are happening and particles scatter in its local vicinity. When the crystal instead is channeling particles it is reducing the number of interactions and steering the particles away from the crystal.

We ended the prior chapter by commenting on the fact that the experiment was done for multi turn passage of the particles while our simulation only shows single passage effects. This affects both the loss map analysis but also the reduction factors produced.

Therefore, we are limited to compare the results of the experimental run and the simulation qualitatively. The absolute value of the reduction factor is naturally higher for the multi turn case than for single passage, as the particles that pass through the beam line in the simulation do not get the chance of being collimated again, so the experimental results have a 1-2 orders of magnitude higher reduction factor.

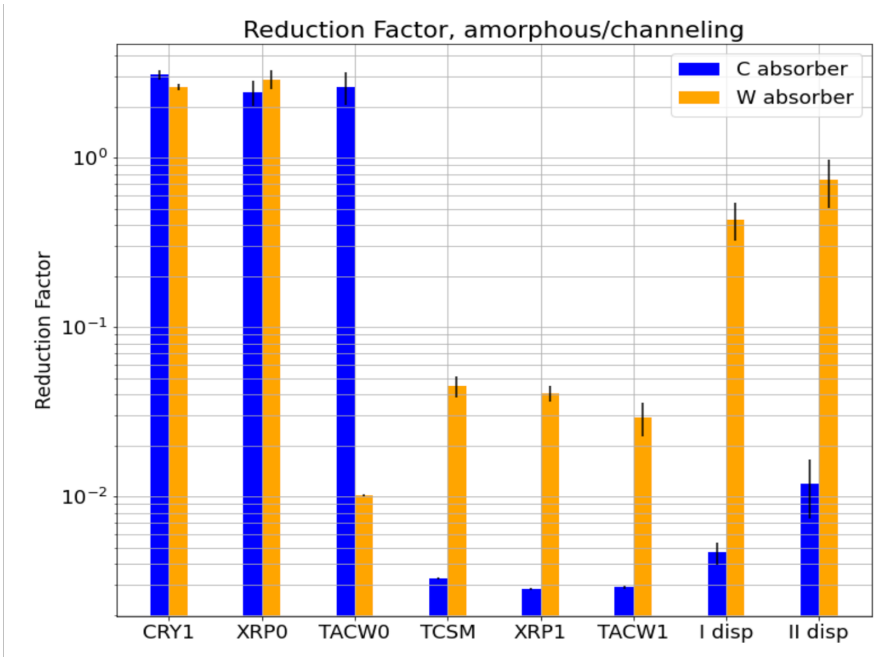

Figure 66: The results for the simulation study that we have done in the UA9 collaboration for the energy deposition in 8 placed beam loss monitors around the LSS5 layout of the SPS. These simulation results are made by replicating the 2018 experimental setup. The bar graph shows the reduction factor at the eight locations for when having the Carbon absorber on the beam line shown by the blue bars, and for when the Tungsten absorber is in shown by the orange bars. The results are produced for single turn passage of the particles.

But if we ignore the absolute values and inspect the results qualitatively we first notice that the general shape of the reduction factors look similar. Especially for the Carbon absorber shown by the blue bar in the figures 65 and 66. For the Tungsten absorber the reduction factor is shown by the orange bars. Also here the general shape seems similar, but we see a discrepancy for the two dispersive regions.

For the last two BLMs coinciding with the dispersive peaks, the resulting reduction factor is higher relative to the other regions when examining the case with the Tungsten absorber on the beam line for the simulation, when comparing it to the results from the experiment.

This discrepancy is difficult to evaluate when the simulation has been performed for single passage, since this might be a statistical fluctuation, that would even itself out if multiple passages were permitted. At the same time, we can speculate whether a multi turn simulation would be comparable at the level of absolute values of the reduction factor. As mentioned we have a systematic effect of neglecting the natural shielding of other adjacent aperture in the beam line during the simulation due to the simple geometry, which would result in a slight overestimation of the energy deposition. Additionally, the multi turn simulation would guarantee that the particles passing through the LSS5 without being lost would be transported back to the beginning of the section. Thus, we neglect the chance of particles being

lost in other sections of the accelerator like for the experimental run. This again would be a systematic effect that would contribute to overestimating the energy depositions. Since the reduction factor is a ratio of the energy deposition when the crystal is channeling over the energy deposition when the crystal is not channeling, the systematic effects of forcing the particles to be lost in the LSS5 might cancel each other out.

From the results stated and from the comparison we can not conclude whether the discrepancy in the regions of the dispersive peaks are in fact an anomaly or it would disappear once a multi turn simulation is performed. Thus, we conclude that further studies are needed to perform a final and conclusive comparison of the 2018 experimental run and the simulation results of the same setup.

10 Conclusion

This thesis has served as a multi aspect study, where we examined the theoretical and practical aspects of applying bent Silicon crystals for a crystal assisted collimation system.

We fully characterised two crystals, the STF113 and the ACP82 by documenting their mean deflection angle, torsion and channeling efficiency. We found for the crystal STF113 a mean deflection angle of $\mu = (44.36 \pm 0.08)\mu$rad, a torsion of $t = (-1.82 \pm 0.17)\mu$rad/mm, and a channeling efficiency of $\eta = (62.76 \pm 0.24)\%$. For the crystal ACP82 we found a mean deflection angle of $\mu = (174.02 \pm 0.11)\mu$rad, a torsion of $t = (-1.08 \pm 0.04)\mu$rad/mm, and a channeling efficiency of $\eta = (49.98 \pm 0.28)\%$ in agreement with prior analysis done on the crystals.

We used the simulation tools Fluka and Flair to first simulate the crystal robustness tests as a review of a 2012 simulation study and 2019 experimental study. Here we found that for the two crystals STF103 and QMP33 from the experimental run, and for the LHC-type crystal used in the 2012 study, that all three crystals would suffer no damage due to temperature increase from a full-on LHC beam on the crystal face when using the same parameters, thus challenging the findings of the 2012 study.

The experimental setup from 2018 was replicated in simulation and the final result was compared between experiment and simulation. Two different absorber materials were compared for a crystal assisted collimation system, where we found that the cleaning efficiency is higher for that of Tungsten compared to Carbon by a factor of 50-57. We addressed that our simulation study has been performed for a single pass scenario, while the experimental study in 2018 was done for multi turn passage of the particles. Therefore, this study concludes that further studies are needed to finalise the comparison of reduction factors in the collimation system. The next step would be to improve the Fluka simulation code, so that the multi turn simulation collimation setup is working satisfactory

This study contributed by performing tests in the SPS serving as a bench mark study for applying the crystal assisted collimation system in the LHC. The next step would be to setup further simulations to review the 2018 experimental setup and thus advance the development of a future full upgrade of the LHC collimation system.

References

[1] Erik Adli. *An Introduction to Particle Accelerators*. 2009. URL: http://www.phys.ufl.edu/~avery/course/4390/reference/Aldi_An%20Introduction%20to%20Particle%20Accelerators.pdf.

[2] Jens Ulrik Andersen. *Notes on channeling*. Dec. 2014.

[3] Neil W. Ashcroft and N. David Mermin. *Solid state physics*. New York: Holt, Rinehart and Winston, 1976. ISBN: 978-0-03-083993-1.

[4] T Baer et al. "TUNE RESONANCE PHENOMENA IN THE SPS AND RELATED MACHINE PROTECTION". In: *CERN* (2010). URL: https://accelconf.web.cern.ch/HB2010/papers/tho1c01.pdf.

[5] Simon Baird. *ACCELERATORS FOR PEDESTRIANS*. Feb. 2007.

[6] W. Barletta. *Introduction to Accelerator Optics*. 2010. URL: https://uspas.fnal.gov/materials/11ODU/Into.pdf.

[7] W. Barletta. *Introduction to Accelerators Lecture 4 Basic Properties of Particle Beams*. 2009. URL: https://uspas.fnal.gov/materials/09UNM/Unit_2_Lecture_4_Beam_Properties.pdf.

[8] A. Baurichter et al. "Channeling of high-energy particles in bent crystals – Experiments at the CERN SPS". en. In: *Nuclear Instruments and Methods in Physics Research Section B: Beam Interactions with Materials and Atoms* 164-165 (Apr. 2000), pp. 27–43. ISSN: 0168583X. DOI: 10.1016/S0168-583X(99)01062-9. URL: https://linkinghub.elsevier.com/retrieve/pii/S0168583X99010629 (visited on 05/17/2022).

[9] C. Biscari. *Transverse Beam Dynamics*. 2014. URL: https://indico.cern.ch/event/528094/contributions/2213316/attachments/1322590/1984069/L3-4-5_-_Transverse_Beam_Dynamics.pdf.

[10] Daniel Abdulla Bobruk. *Python scripts used for production of results for the Master's thesis*. Mar. 2021. URL: https://github.com/qkg982/Thesis_scripts.

[11] Hans Braun. *Emittance Diagnostics*. June 2008.

[12] CERN. *CERN's accelerator complex*. URL: https://home.cern/science/accelerators/accelerator-complex.

[13] CERN. *How an accelerator works*. URL: https://home.cern/science/accelerators/how-accelerator-works.

[14] CERN. "Proton Synchrotron". In: *CERN Annual Report 1959* (). URL: https://cds.cern.ch/record/1479637/files/1959_E_p29.pdf?version=1.

[15] Luigi Salvatore Esposito et al. "Crystal for Slow Extraction Loss-Reduction of the SPS Electrostatic Septum". en. In: *Proceedings of the 10th Int. Particle Accelerator Conf.* IPAC2019 (2019). Artwork Size: 4 pages, 4.713 MB ISBN: 9783954502080 Medium: PDF Publisher: JACoW Publishing, Geneva, Switzerland, 4 pages, 4.713 MB. DOI: 10.18429/JACOW-IPAC2019-WEPMP028. URL: http://jacow.org/ipac2019/doi/JACoW-IPAC2019-WEPMP028.html (visited on 05/14/2022).

[16] Peter Hansen. *Particle detectors and accelerators Lecture notes.* Oct. 2016.

[17] Bernhard Holzer. *Introduction to Transverse Beam Optics. III.) Twiss Parameters & Lattice Design.* 2014. URL: https://www.cockcroft.ac.uk/wp-content/uploads/2014/12/Neil_3.pdf.

[18] T.H. Kokkeler et al. *Python data analysis at the UA9 experiment.* Aug. 2019.

[19] A Lechner et al. *Potential thermal and radiation damage to crystals in the LHC beams.* Sept. 2012.

[20] A. Mazzolari et al. "Silicon crystals for steering of high-intensity particle beams at ultra-high energy accelerators". In: (2020). Publisher: arXiv Version Number: 1. DOI: 10.48550/ARXIV.2006.15582. URL: https://arxiv.org/abs/2006.15582 (visited on 05/11/2022).

[21] Daniele Mirarchi. "Crystal collimation for LHC". In: *High Energy Physics Department Imperial College London* (Mar. 2015).

[22] NIST. *Stopping power and range tables for protons in various materials.* URL: https://physics.nist.gov/PhysRefData/Star/Text/PSTAR.html.

[23] NIST. *Stopping power, density effect parameters, range, and radiation yield tables for electrons in various materials.* URL: https://physics.nist.gov/cgi-bin/Star/e_table.pl.

[24] Y. Papaphilippou and N. C. Lasheras. *Hill's equations and transport matrices.* June 2005. URL: https://yannis.web.cern.ch/teaching/matrices.pdf.

[25] Stefano Petrucci. "Advanced Crystal collimation studies at the SPS". In: *SAPIENZA UNIVERSITÀ DI ROMA* (2017).

[26] Roberto Rossi et al. "Measurements of coherent interactions of 400GeV protons in silicon bent crystals". en. In: *Nuclear Instruments and Methods in Physics Research Section B: Beam Interactions with Materials and Atoms* 355 (July 2015), pp. 369–373. ISSN: 0168583X. DOI: 10.1016/j.nimb.2015.03.001. URL: https://linkinghub.elsevier.com/retrieve/pii/S0168583X15002013 (visited on 05/11/2022).

[27] Hasan Said. "BENT SILICON CRYSTALS FOR THE LHC COLLIMATION: STUDIES WITH AN ULTRARELATIVISTIC PROTON BEAM". In: *UNIVERSITA' DEGLI STUDI DELL'INSUBRIA* (Oct. 2007).

[28] W. Scandale et al. “Beam steering performance of bent silicon crystals irradiated with high-intensity and high-energy protons”. en. In: *The European Physical Journal C* 79.11 (Nov. 2019), p. 933. ISSN: 1434-6044, 1434-6052. DOI: 10.1140/epjc/s10052-019-7448-2. URL: http://link.springer.com/10.1140/epjc/s10052-019-7448-2 (visited on 05/11/2022).

[29] G. Smirnov et al. “On thermal and radiation damage to silicon crystals in the LHC proton beam”. en. In: *Nuclear Instruments and Methods in Physics Research Section B: Beam Interactions with Materials and Atoms* 309 (Aug. 2013), pp. 141–145. ISSN: 0168583X. DOI: 10.1016/j.nimb.2013.01.066. URL: https://linkinghub.elsevier.com/retrieve/pii/S0168583X13002991 (visited on 05/11/2022).

[30] Daniil Sukhonos. *Experimental studies of coherent processes in bent silicon crystals*. June 2017.

[31] Gennady Sushko. “Atomistic molecular dynamics approach for channeling of charged particles in oriented crystals”. In: (Oct. 2015).

[32] Irene Tamborra. *Astrophysical Shocks and Particle Acceleration*. 2020.

[33] *The Fluka Line Builder Wiki (Twiki)*. URL: https://twiki.cern.ch/twiki/bin/view/FlukaTeam/FlukaLineBuilder.

[34] Ezio Todesco. *Unit 2 Magnets for circular accelerators: the interaction regions*. May 2020. URL: https://indico.cern.ch/event/913156/attachments/2034720/3406300/2.pdf.

[35] Elena Wildner. *Accelerator Physics Transverse motion*. 2008. URL: http://benasque.org/2008nufact/talks_contr/101Elena_day2.pdf.

11 Appendix I

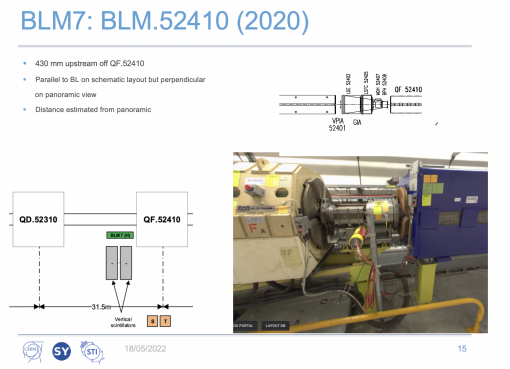

Figure 67: BLM7 2020 - perpendicular to beam line on panoramic both year 2020 and 2017. Layout shows it should be perpendicular to the beam line. Is not included on the schematic drawing

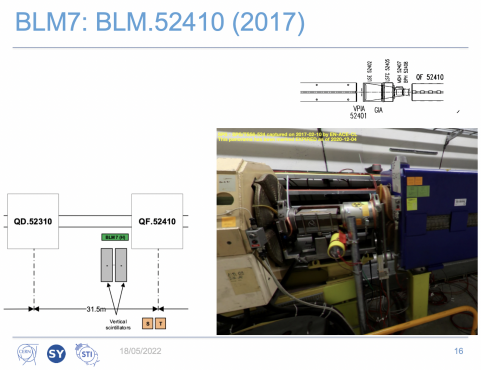

Figure 68: BLM7 2017 - perpendicular to beam line on panoramic both year 2020 and 2017. Layout shows it should be perpendicular to the beam line. Is not included on the schematic drawing

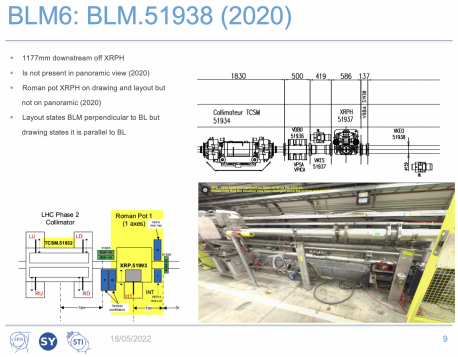

Figure 69: BLM6 2020 - not present on year 2020 panoramic

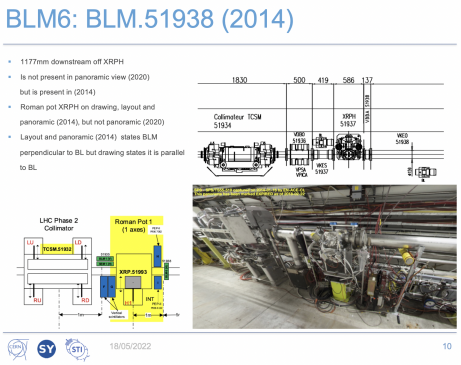

Figure 70: BLM6 2014 - Layout drawing and panoramic photo states the BLM is perpendicular. But schematic drawing says its parallel

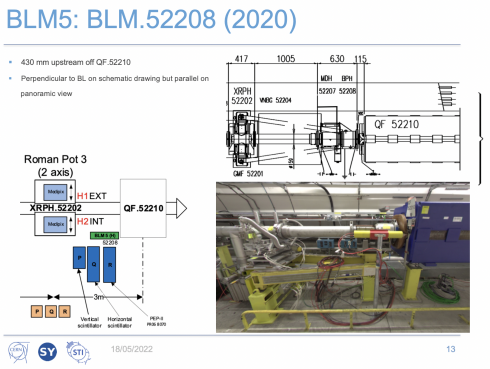

Figure 71: BLM5 2020 - BLM present on both panoramic views, but schematic drawing states it is perpendicular to the beam line.

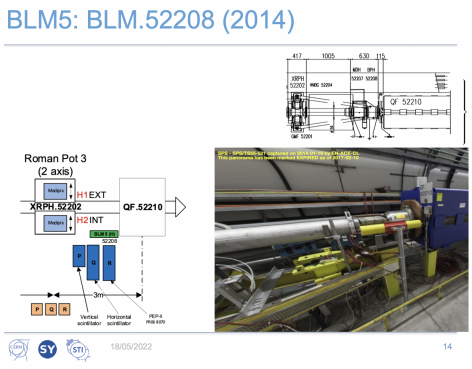

Figure 72: BLM5 2014 - BLM present on both panoramic views, but schematic drawing states it is perpendicular to the beam line.

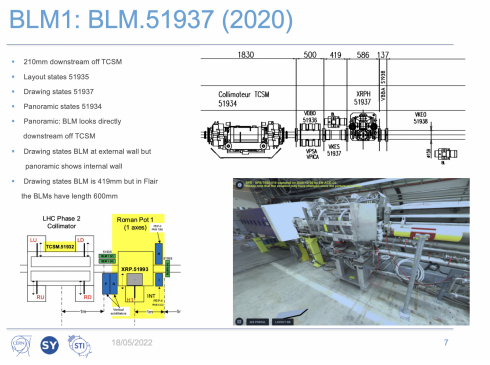

Figure 73: BLM1 2020 - shown on the 2020 panoramic. Both layout and schematic drawing states the BLM should be placed towards the external wall, but the panoramic shows it is installed towards the internal wall.

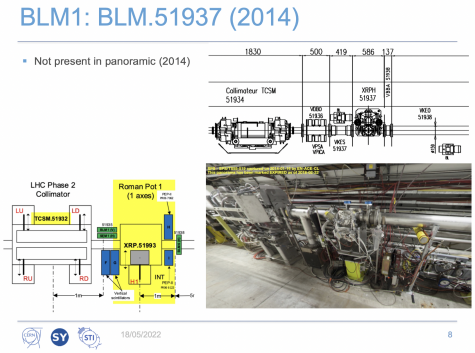

Figure 74: BLM1 2014 - not present in the year 2014 panoramic view.

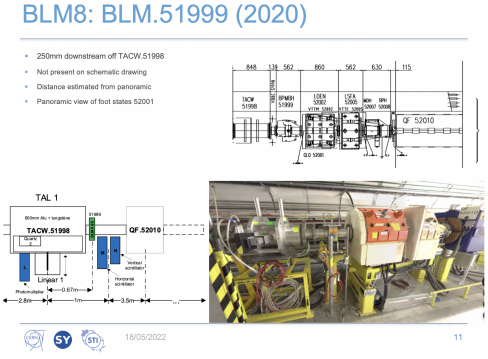

Figure 75: BLM8 2020 - present on both panoramic photos, but not present on the schematic drawing.

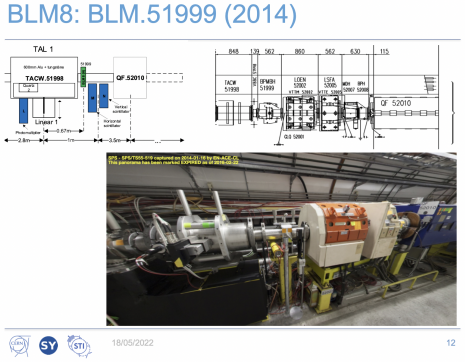

Figure 76: BLM8 2014 - present on both panoramic photos, but not present on the schematic drawing.

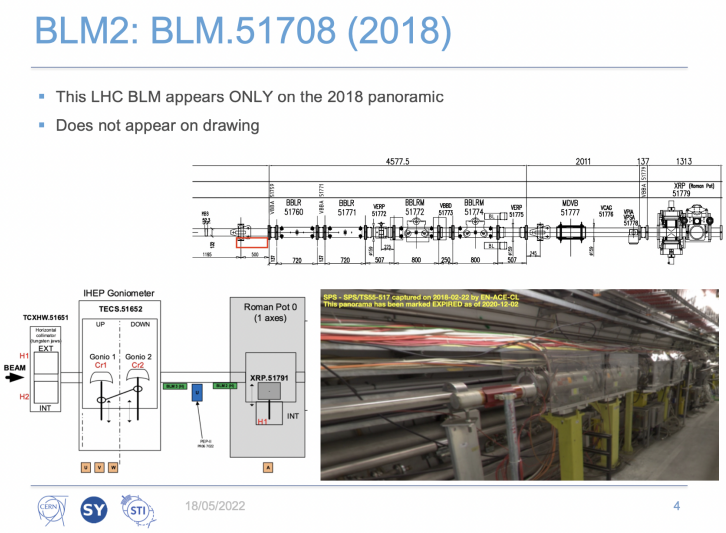

Figure 77: BLM2 2018 - is on panoramic photo and layout, but not on the schematic drawing